SINGLE-CELL IMPEDANCE SPECTROSCOPY

A Thesis
presented to
the Faculty of California Polytechnic State University,
San Luis Obispo

In Partial Fulfillment
of the Requirements for the Degree
Master of Science in Biomedical Engineering

by
David Paul Lange
December 2019

COMMITTEE MEMBERSHIP

TITLE:	Single Cell Impedance Spectroscopy
AUTHOR:	David Paul Lange
DATE SUBMITTED:	December 2019

COMMITTEE CHAIR:	David Clague Ph.D. Professor of Biomedical Engineering California Polytechnic State University
COMMITTEE MEMBER:	Benjamin Hawkins Ph.D Professor of Biomedical Engineering California Polytechnic State University
COMMITTEE MEMBER:	Robert Szlavik Ph.D Professor of Biomedical Engineering California Polytechnic State University
COMMITTEE MEMBER:	James Eason, Ph.D. Professor of Biomedical Engineering California Polytechnic State University

ABSTRACT

Impedance spectroscopy (IS) is an important tool for cell detection and characterization in medical and food safety applications. In this thesis, the Cal Poly Biofluidics Lab's impedance spectroscopy system was re-evaluated and optimized for single-cell impedance spectroscopy. To evaluate the IS system, an impedance spectroscopy bioMEMS chip was fabricated in the Cal Poly Microfabcrication lab, software was developed to run IS experiments, and studies were run to validate the system. To explore IS optimization, Maxwell's mixture theorem and the Schwartz-Christoffel transform were used to calculate an analytic impedance solution to the co-planar electrode system, a novel volume fraction to account for the non-uniformity of the electric field was developed to increase the accuracy of the analytic solution and to investigate the effect of cell position on the impedance spectrum, a software program was created to allow easy access to the analytic solution, and FEA models were developed to compare to the analytic solution and to investigate the effect of complex device geometry.

ACKNOWLEDGEMENTS

Foremost, I would like to express my sincere gratitude to Dr. David Clague. Dr. Clague's insights into impedance spectroscopy helped immeasurably. He is an incredible advisor and mentor who inspired me to question the status-quo and his continued support, motivation, and guidance with and beyond this thesis has been a source of tremendous personal growth.

I want to make a special thank you to Dr. Ben Hawkins. Without his time resources, and support, the device would not have been fabricated at Cal Poly. It has been a pleasure to spend those long hours in the clean room with you.

I'd like to thank Hans Mayer for his training and aide in the soft-lithography manufacturing process.

I'd also like to thank Jack Foley whose companionship and collaboration inside the clean room was critical for delivering a functional device.

To the committee members, thank you for your time in considering this thesis.

To my friends and family, thank you for your unending support and guidance, without it, this thesis would not have been possible.

Contents

List of Figures

List of Tables

Chapter 1: Introduction

Cell detection and characterization are important for applications in medical diagnosis and food safety [1]. With the advent of micro-electro-mechanical systems (MEMS), cell characterization techniques have developed with increasing precision and cost-effectiveness. One of these techniques is impedance spectroscopy. Cell impedance spectroscopy measures the electrical impedance of cell(s) over a range of frequencies and can identify cell types, differentiate cell states, and provide information about cell components. With significantly increased manufacturing precision provided by MEMS technologies, cell impedance spectroscopy has been miniaturized to measure the impedance spectrum of single cells instead of macro suspensions.

The applications of single cell impedance spectroscopy are extensive. In medical diagnostics, the ability to isolate the impedance spectrum of a single cell allows the diagnosis of diseases with very small limits of detection, such as early detection of cancer by identifying circulating tumor cells that can be as scarce as 1 cell per mL of blood [2]. In food safety single cell spectroscopy can detect pathogens in a rapid and inexpensive manner, such as E.Coli and Salmonella contamination in water sources [3]. In addition, impedance spectroscopy is an important tool in research, with the ability to quickly measure a cell's state and response to stimuli.

The focus of this thesis will be to reevaluate and optimize the Cal Poly Biofluidic lab's single cell impedance sensor.

1.1 The Cal Poly Biofluidic Lab's Cell Impedance System

In 2009, Fadriquela and Hernandez created a cell impedance spectroscope system for the Cal Poly biofluidic lab [4], [5]. The purpose of the project was to create a system to measure single cell impedance measurements. The project included the design of the electrodes and microfluidic channels of the impedance sensor,

manufacturing of the device, installment of requisite hardware, and development of software necessary for impedance measurements.

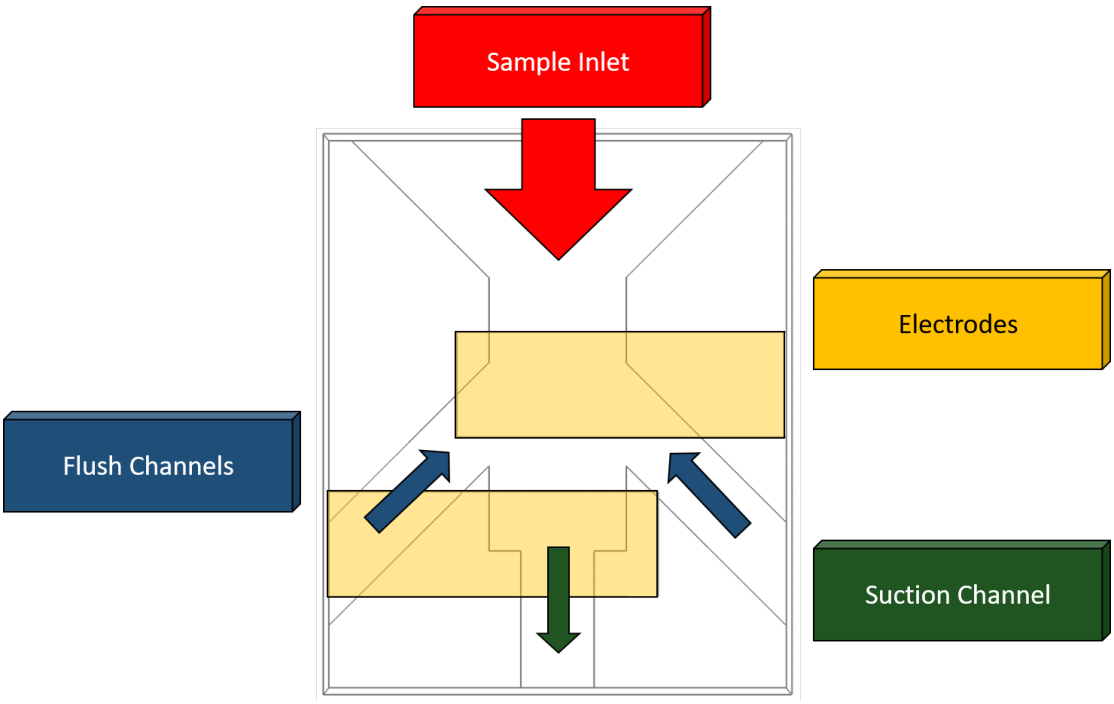

Figure 1.1: Functional diagram of cell impedance sensor chamber.

The impedance sensor was designed with two parallel 11.5 micron wide electrodes with a 5 micron offset that lays under a 15 by 15 micron target measurement area. The device isolates a cell by activating flush and suction channels once a cell from the sample inlet wanders into the test chamber. (figure 1.1). Once the device captures a cell, voltage signals over a range of frequencies are applied through the electrodes, and the impedance can be calculated from current response. Figure 1.2 depicts the simulated electric fields lines around a cell with desired device behaviour (the development of the COMSOL model is described in section 4.2). However, the device could not accomplish single-cell isolation and impedance measurements were taken on a suspension of cells (figure 1.3).

Manufacturing of the device took place in the Cal Poly microfabrication lab and the University of Santa Barbara Nanofabrication Lab. Fadriquela fabricated the microchannels using soft-lithography and Hernandez worked the Santa Barbara Lab to create the electrodes with electron beam deposition. Figure 1.4 and 1.5 depict

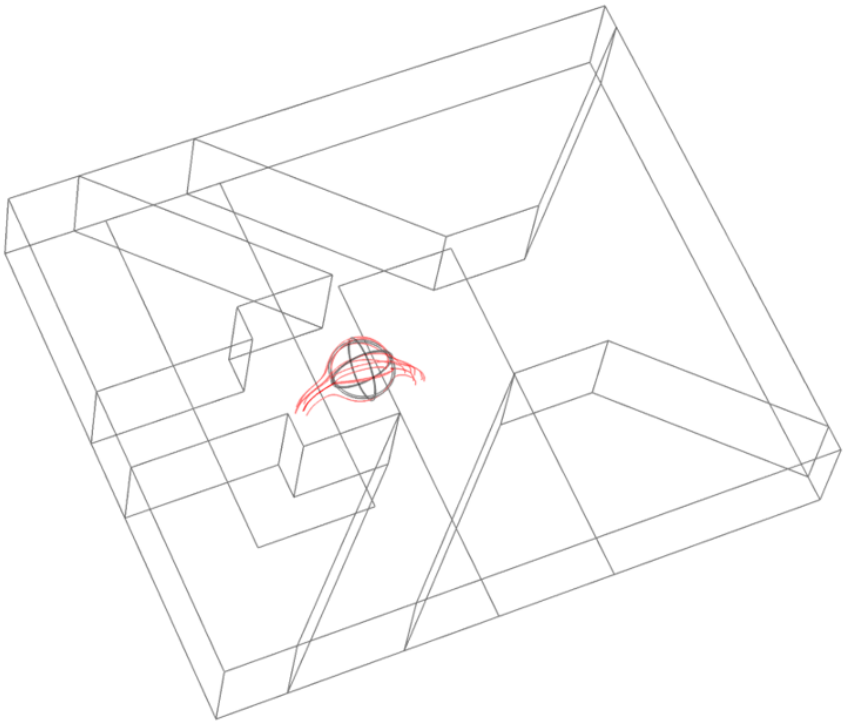

Figure 1.2: Example of desired device behaviour using a COMSOL simulation of electric field lines through a cell. A detailed description of the COMSOL model is presented in section 4.2.

the masks used in fabricating the microfluidic channels and electrodes.

1.2 Thesis Purpose and Objectives

The purpose of this thesis is to reevaluate and optimize the Cal Poly Biofluidic Lab's cell impedance spectroscopy system. To accomplish this, the following questions were answered:

1. Are there aspects of the impedance spectroscope that need redesign or optimization?

2. Is the hardware implementation correct?

3. Can the correct circuit model and desired data acquisition and analysis be packaged and incorporated in a device interface computer program?

4. Can model based design be applied to characterize and optimize electric fields and impedance to inform future designs?

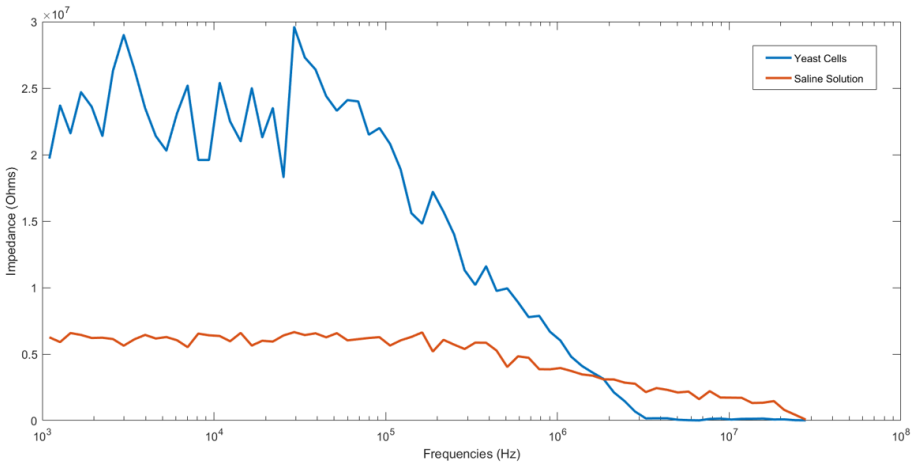

Figure 1.3: Impedance spectrum of yeast suspensions and saline solution from the Cal Poly Biofluidic Lab's impedance spectroscopy system [5].

5. Can a device be manufactured at Cal Poly to validate the device design and analysis?

By answering these guiding question, this thesis characterized and enhanced the Biofluidic's Lab's cell impedance spectroscope and developed a model based design framework for future IS systems.

Figure 1.4: Micro channel mask by Fadriquela [4].

Figure 1.5: Electrode mask by Hernandez [5].

Chapter 2: Background

2.1 Cells

The cell is the basic unit of life. At the fundamental level, a cell must have an outer membrane that acts as a gatekeeper between the surrounding environment and the interior constituents. The contents of the cell interior varies widely between organisms, cell specializations, and states of each cell. For example, mature red blood cells do not contain a nuclei or any genetic material, but skeletal muscle fiber consist of multiple nuclei [6]. However, all these variations can be generalized to useful cell models, such as the model for human cells in figure 2.1.

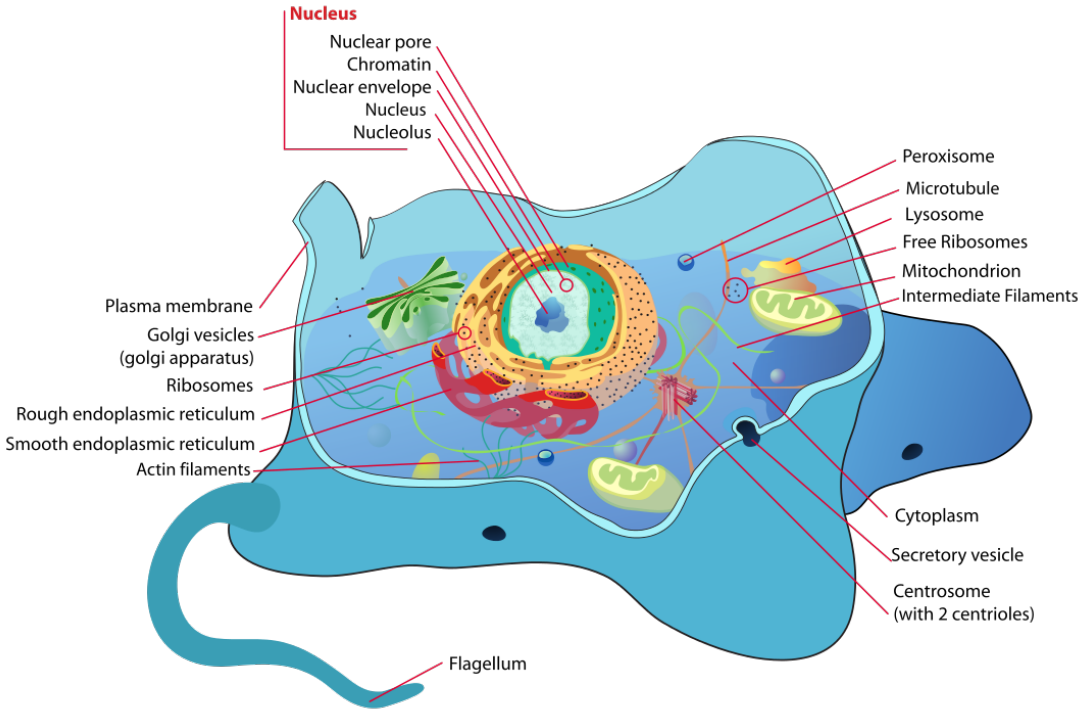

Figure 2.1: Diagram of human cell structure [7].

Generally, a cell carries genetic information in the nucleus which resides inside the cell membrane and cytoplasm. Cytoplasm is the cell material inside of the cell membrane and outside the nuclei. The cytoplasm consists of non-nuclei organelles and cytosol. Cytosol refers to the cellular solution between the cell organelles and the membrane, wich contains salts, nucleic acids and cytoskeleton filaments [6].

Organnelles are membrane bound structures inside the cell that perform special functions. Organelles include nuclei, mitochondria, the Golgi apparatus, lysosomes, and vacuoles.

2.1.1 The Cell Membrane

The cell membrane is an essential component of the cell that is necessary for signalling, extracellular interaction, and maintaining equilibrium. The membrane is primarily composed of the lipid bilayer, which is a semi-permeable barrier constructed from phospholipids. A phospholipid has a hydrophilic head group and a hydrophobic tail group. When exposed to an aqueous environment, phospholipids join together in a configuration that leaves the head groups exposed to the aqueous solution and the tail group surrounded by other non-polar tail groups. In the case of a cell, the phospholipids take the form of a spherical bilayer membrane (figure 2.2). The membrane forms a semi-permeable barrier that allows for restricted diffusion of certain molecules.

In addition to phospholipids, the cell membrane is packed with proteins that are critical for cell life and its interaction with the environment. Of special interest to this thesis, are channel and transport proteins that allow controlled passage of molecules through the membrane.

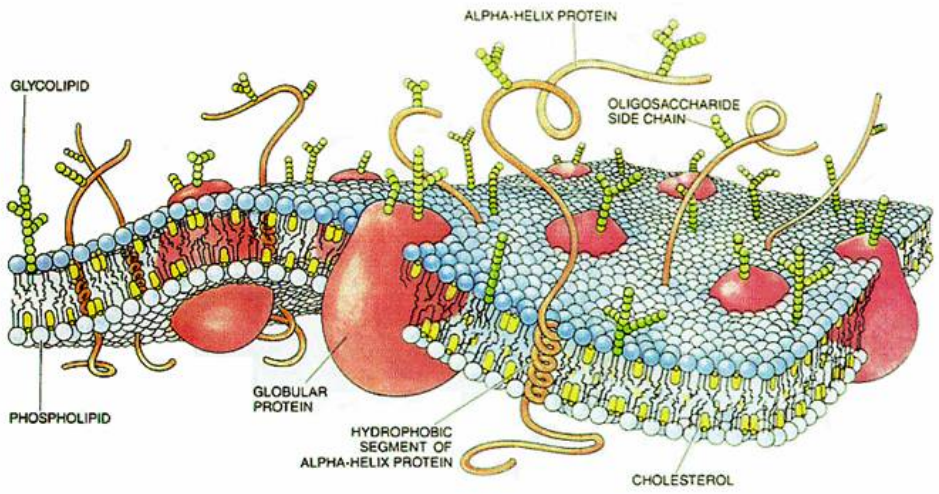

Figure 2.2: Diagram of the cell membrane [8]

2.1.2 The Electrical Model of the Cell

The state of a cell directly affects its electrical properties. Measuring these properties provides insight into the cell state, type, and afflictions. A common representation of the bulk electrical model of a cell is presented in figure 2.3. As a bulk electrical element, the cell membrane can be modeled as a leaky capacitor that can accumulate a charge differential, but also leaks charges across the membrane. This behaviour can be modeled as a resistor and capacitor in parallel. The membrane capacitance is supplemented by the formation of an electric double layer (EDL). A biological cell carries a net negative charge which results in the development of a surrounding 10-100 nm thick electric double layer in electrolyte solutions [9]. The electric double layer contributes to the capacitance of the cell membrane. The EDL will be described in further detail in section 2.5. The bulk electrical properties of the cytoplasm are often modeled as a RC series circuit with a relatively small capacitive impedance.

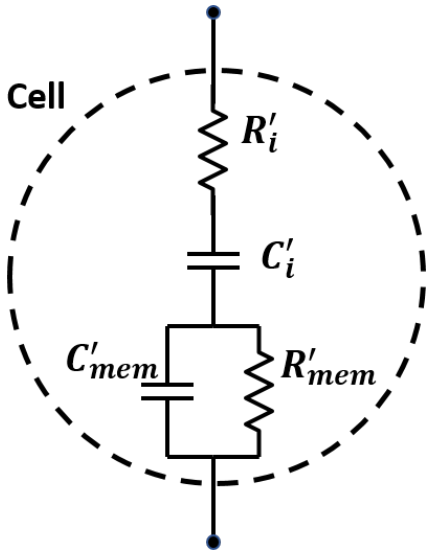

Figure 2.3: Electrical model of single shelled cell. R'_i and C'_i are the resistance and capacitance of the cytoplasm, and R'_{mem} and C'_{mem} are the resistance and capacitance of the membrane.

.

2.2 Dielectric Spectroscopy

The dielectric properties of cells have been investigated since 1910 when Höber showed the existence of the cell membrane by measuring the conductivity of erythrocytes at high and low frequencies [10]. The field of study further developed with Fricke's application of Maxwell's equations to measure the capacitance and thickness of the cell membrane from 1924 to 1925 [11]–[14].

In 1928, Cole used Maxwell's mixture equation to derive the complex impedance of a single shelled cell model and developed equations to describe the Cole-Cole plot [15]. And with Curtis, Cole made the first single cell measurements on a Nitella cell (a large bacteria cell that ranges from 20 to 60 mm in length) [16].

From 1957-1968 Schwan used broadband electric impedance spectroscopy to identify α, β, and γ dispersions of a cell [17]–[19]. A dielectric dispersion is a frequency range with a large change in permittivity with respect to frequency. The permittivity of a material is the resistance to forming an electric field over a medium. In general the effects of a source charge can be described as the polarization of surrounding medium and the residual electric field over the resisting polarized medium. For a dielectric material, the electric field may be thought of as having two components: the electric displacement vector $\boldsymbol{D}$ that accounts for the electric field generated from separated free electrical charges, and the polarization $\boldsymbol{P}$ which accounts for the bound polarization charges in a dielectric material. The effect of $\boldsymbol{P}$ is to attenuate of the electric field. This relationship can be observed by rearranging the definition of electric displacement.

$$\boldsymbol{D} = \epsilon_o \boldsymbol{E} + \boldsymbol{P}, \tag{2.1}$$

$$\boldsymbol{E} = \frac{1}{\epsilon_o}\Big(\boldsymbol{D} - \boldsymbol{P}\Big), \tag{2.2}$$

where ϵ_o is known as the dielectric constant or the permittivity of the vacuum, with a value of 8.85E-12 F/m.

For a linear dielectric medium, the polarization can be defined as

$$\boldsymbol{P} = \epsilon_o \chi \boldsymbol{E}, \tag{2.3}$$

where χ is the electric susceptibility. Substituting equation 2.3 into 2.1

$$\boldsymbol{D} = \epsilon_o(1+\chi)\boldsymbol{E} = \epsilon_o \epsilon_r \boldsymbol{E} = \epsilon \boldsymbol{E}, \tag{2.4}$$

where $\epsilon = \epsilon_o \epsilon_r$ is the permittivity and $\epsilon_r = 1 + \chi$ is the relative permittivity of a medium. For the case of isotropic materials, χ and ϵ reduce to scalar values, but for anisotropic materials, they are expressed as second order tensors. The susceptibility describes how a material polarizes under an electric field, and the permittivity describes the resistance to forming an electric field over that material. For dielectrics, the permittivity and susceptibility are closely related, but due to the resistance to forming an electric field over a vacuum, the two quantities are subtly different. The permittivity of a dielectric can be viewed as the sum of resistance to forming an electric field over a vacuum and the effect of polarizing a material. Figure 2.1 list the permittivity and susceptibility of some common materials.

Material	$\boldsymbol{x_e}$	$\boldsymbol{\epsilon_r}$
Vacuum	0	1
Dry air	5E-4	1.0005
Glass	5	6
Silicon	11	12
Ethanol	23	24
Water	79	80
Polystyrene	1.5	2.5

Table 2.1: Permittivities of and susceptibilities of common materials [20].

The frequency dependence of the permittivity arises from the time dependent material polarization or charge reorganization. Examples of charge reorganization include electron cloud distortion, charged particle displacement, and reorientation

of molecules with dipoles. α, β, and γ dispersions refers to the ranges of alternating current frequencies where the permittivity decreases significantly in cells (i.e. dielectric relaxation). Figure 2.4 depicts an approximate permittivity spectrum of a cell.

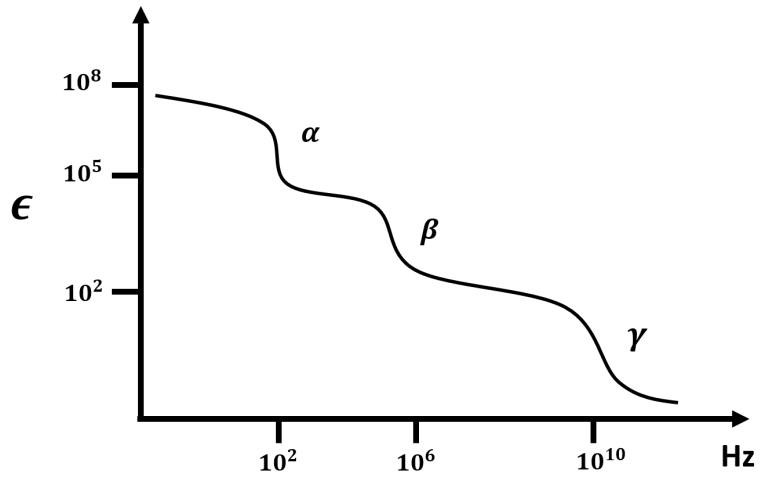

Figure 2.4: General cell permittivity spectrum with labeled α, β and γ dispersions.

β dispersions can occur up to a magnitude of 10 Mhz and is caused by the relaxation of the cell membrane. For lower frequencies, the membrane has enough time to charge and provide resistance to the electric field, but at frequencies greater than than the relaxation, the membrane does not have sufficient time to fully charge and provides little resistance to the electric field. γ dispersion is related to the relaxation of water molecules. Instead of a charging membrane, γ dispersion is due to the dipole rotation of the water molecules and the biomolecules that water is bound to. The source of α dispersion is undetermined, but current theories include the surface reactance of the electric double layer near the charged cell, the impedance of the sarcoplasmic recticulum (for muscle fibers), or the frequency dependent conductance of ionic membrane channels as predicted by the Hodgkin-Huxley equations [19].

These developments laid the foundations for the following techniques for measuring the dielectric properties of single cells.

2.2.1 Dielectrophoresis

The dielectrophoretic force (DEP) is the force generated on a particle suspended in a solution by the interaction of an applied nonuniform electric field and an induced dipole moment developed through Maxwell-Wagner polarization (a build up of charges at dielectric boundaries). Peter Debye and Herbert A. Pohl were among the first to develop dielectrophoresis and demonstrated how particles could be moved with nonuniform electric fields [21]. With an applied AC electric field, the average DEP force on a spherical particle is expressed as [22], [23]

$$\left\langle F_{DEP} \right\rangle = 2\pi\epsilon_m R^3 \mathrm{Re}[\tilde{f}_{CM}]\nabla|\mathbf{E_{rms}}|^2, \tag{2.5}$$

with

$$\tilde{f}_{CM} = \frac{\tilde{\epsilon}_p - \tilde{\epsilon}_m}{\tilde{\epsilon}_p + 2\tilde{\epsilon}_m}, \tag{2.6}$$

where ϵ_m is the permittivity of the medium, R is the radius of the particle, $\tilde{f}_{CM}$ is the Clausius-Mossotti factor for spherical particles, $\tilde{\epsilon}_p$ is the complex permittivity of the particle, $\tilde{\epsilon}_m$ is the complex permittivity of the medium, and $\mathbf{E_{rms}}$ is the root mean square of the electric field. For most cases, the complex permittivity can be expressed as

$$\tilde{\epsilon} = \epsilon - j\frac{\sigma}{\omega}, \tag{2.7}$$

where ϵ is the permittivity, $j = \sqrt{-1}$, σ is the conductivity, and ω is the angular frequency of the electric field.

From equation 2.5 and 2.6, it can be noted that, given a non-uniform electric field, the magnitude of the dielectrophoretic force depends on the size of the particle and the polarizability of the particle with respect to the medium (i.e Re$\left[\tilde{f}_{CM}\right]$), and the sign of the force only relates to the polarizability of the particle and medium (figure 2.5). It should be noted that, based on equation 2.6, the real part of the Clausius-Mossotti factor is restricted to less than 1 and greater than -0.5. However,

for non-spherical shapes, such as elongated ellipses, equation 2.6 does not satisfy the Clausius-Mossotti factor which can reach values far greater than 1.

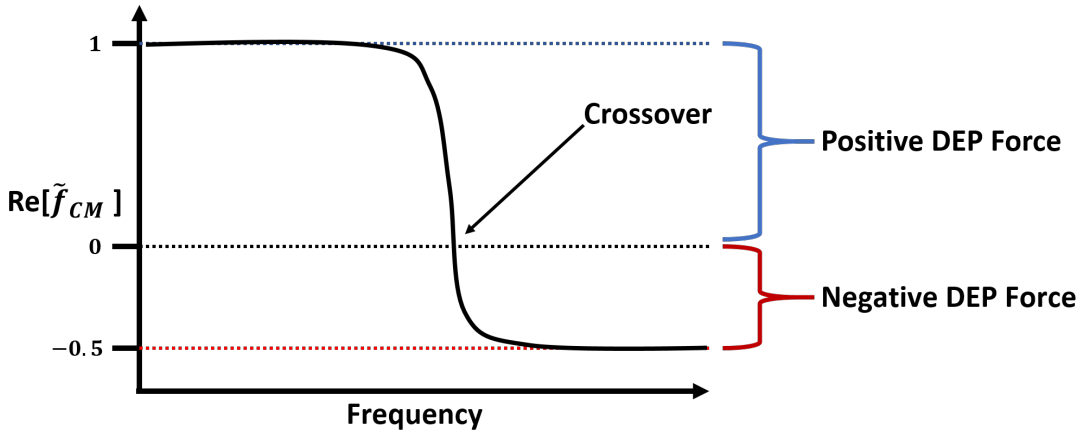

Figure 2.5: Frequency crossover of Clausius-Mossotti factor with labeled regions of positive and negative dielectriphoretic forces. From equation 2.5, if $\tilde{\epsilon}_p$ is greater than $\tilde{\epsilon}_m$, then the DEP force is positive, if $\tilde{\epsilon}_m$ is less than $\tilde{\epsilon}_p$, then the DEP force is negative.

To extract dielectric properties of cells using dielectric forces, the DEP crossover frequency can be experimentally determined and compared to theoretical values [22]. The crossover frequency occurs when the real part of the Clausius-Mossotti factor equals zero and is where the DEP force switches from a positive to a negative DEP force (or *vice versa*). Experimentally, this can be determined by the observation of a stationary cell in a non-uniform electric field. Theoretically, the crossover frequency can be described as

$$f_{cross} = \frac{1}{2\pi}\sqrt{\frac{(\sigma_m - \sigma_p)(\sigma_p + 2\sigma_m)}{(\epsilon_p - \epsilon_m)(\epsilon_p + 2\epsilon_m)}}, \tag{2.8}$$

where f_{cross} is the crossover frequency, subscript p denotes the particle, and subscript m denotes the medium. Equation 2.8 can be rewritten to include the Maxwell-Wagner relaxation frequency as [22]

$$f_{cross} = \frac{1}{2\pi}\sqrt{\frac{\sigma_m - \sigma_p}{\epsilon_p - \epsilon_m} f_{MW}}, \tag{2.9}$$

with

$$f_{MW} = \frac{1}{2\pi\tau_{MW}}, \tag{2.10}$$

$$\tau_{MW} = \frac{\epsilon_p + 2\epsilon_m}{\sigma_p + 2\sigma_m}, \tag{2.11}$$

where f_{MW} and τ_{MW} are the Maxwell-Wagner relaxation frequency and time constant respectively. The Maxwell-Wagner relaxation frequency characterizes the frequency of β dispersion described by Schwan [22].

For a single shelled model of a cell, the crossover frequency can be expressed as

$$f_{cross} = \frac{\sqrt{2}}{8\pi R C_{mem}} \sqrt{(4\sigma_m - R G_{mem})^2 - 9R^2 G_{mem}^2}, \tag{2.12}$$

where C_{mem} is the specific capacitance of the cell membrane and G_{mem} is the specific conductance of the membrane.

2.2.2 Electrorotation

Electrorotation is the applied torque to a polarized particle in a medium of different dielectric properties by a rotating electric field. Such a field can be created with a system of four electrodes with sinusoidal signals of 90° phase shifts between adjacent electrodes [24]. The phenomenon of electrorotation was first documented by Pohl in 1978 and then developed into dependable methods by Arnold and Zimmerman in 1982 [25], [26].

The average torque exerted on a spherical particle can be expressed as [22]

$$\mathcal{T}_{\mathsf{ROT}} = -4\pi\epsilon_m R^3 \mathsf{Im}\left[\tilde{f}_{CM}\right] |\mathbf{E}|^2, \tag{2.13}$$

where $\mathcal{T}_{\mathsf{ROT}}$ is the torque applied to the induced dipole of the particle, ϵ_m is the permittivity of the medium, R is the radius of the spherical particle, **E** is the electric field, and $\mathsf{Im}\left[\tilde{f}_{CM}\right]$ is the imaginary part of the Clausius-Mossotti factor expressed in equation 2.6. Similar to the average dielectrophoretic force (equation 2.5), the Clausius-Mossotti factor is the frequency dependent element and controls whether

the particle rotates with or against the applied rotating electric field.

The applied torque can be measured by the angular velocity of the particle, which can be expressed as [27]

$$R_{\mathsf{ROT}} = -\frac{\epsilon_m \mathsf{Im}\big[\tilde{f}_{CM}\big]|\mathbf{E}|^2}{2\eta}K, \tag{2.14}$$

where R_{ROT} is the angular velocity, η is the dynamic viscosity, and K is the scaling factor. When the angular velocity has reached equilibrium, the applied torque will be proportional R_{ROT} and related by the scaling factor K. The electrorotation torque spectrum of a cell can be used, in tandem with equation 2.13, to determine the dielectric properties of the cell.

By combining dielectrophoretic and electrorotation spectroscopy techniques, significant details of the dielectric properties can be obtained. Since dielectrophoretic spectroscopy determines the real Clausius-Mossotti factor spectrum, and electrorotation determines the imaginary Clausius-Mossotti factor, the full $\tilde{f}_{CM}$ spectrum can be deduced from which dielectric properties can be extracted. By separating the real and imaginary components of the Clausius-Mossotti factor, the following expressions are obtained [22], [28].

$$\mathsf{Re}\big[\tilde{f}_{\mathsf{CM}}\big] = \frac{(\sigma_p - \sigma_m)}{(1+\omega^2\tau_{\mathsf{MW}}^2)(\sigma_p + 2\sigma_m)} + \frac{\omega^2\tau_{\mathsf{MW}}^2(\epsilon_p - \epsilon_m)}{(1+\omega^2\tau_{\mathsf{MW}}^2)(\epsilon_p + 2\epsilon_m)}, \tag{2.15}$$

$$\mathsf{Im}\big[\tilde{f}_{\mathsf{CM}}\big] = \frac{3\omega\tau_{\mathsf{MW}}(\epsilon_p\sigma_m - \epsilon_m\sigma_p)}{(1+\omega^2\tau_{\mathsf{MW}}^2)(\epsilon_p + 2\epsilon_m)(\sigma_p + 2\sigma_m)}. \tag{2.16}$$

A major shortcoming of the previously discussed techniques is the long time needed for measurements. An electrorotaion assay could potentially take up to several seconds per test and limit the number of cells tested. An alternative approach, electric impedance spectroscopy, allows for rapid dielectric spectroscopy, and with flow-through designs, allows dielectric spectroscopy of every cell in a sample.

2.2.3 Impedance Spectroscopy

Impedance

Electrical Impedance is defined as the opposition of a system to the flow of electrical current for an applied voltage. If a sinusoidal voltage is applied to an arbitrary system, then the voltage and current can be expressed as

$$V(w) = |V|\cos(wt - \theta_V), \tag{2.17}$$

$$I(w) = |I|\cos(wt - \theta_I), \tag{2.18}$$

where w is the angular frequency, t is the time in seconds, and θ_V and θ_I are the phase of V and I respectively. Using Euler's formula, equations 2.17 and 2.18 can be recognized as the real part of the following:

$$\hat{V}(w) = |V|e^{j(wt-\theta_V)}, \tag{2.19}$$

$$\hat{I}(w) = |I|e^{j(wt-\theta_I)}. \tag{2.20}$$

Applying Ohm's law, the impedance of the system can be expressed as

$$Z = \frac{|V|}{|I|}e^{j(\theta_I-\theta_V)}, \tag{2.21}$$

or as

$$Z = |Z|e^{j\theta}, \tag{2.22}$$

where θ is the difference in phase of the voltage from the current after the current passes through the system. Equation 2.22 sets the interpretation of impedance to be a vector that lives on the complex plane where $|Z|$ is the length of the vector, and θ is the angle of the vector from the positive real axis (figure 2.6).

As a vector on the complex plane, impedance can be represented in rectangular

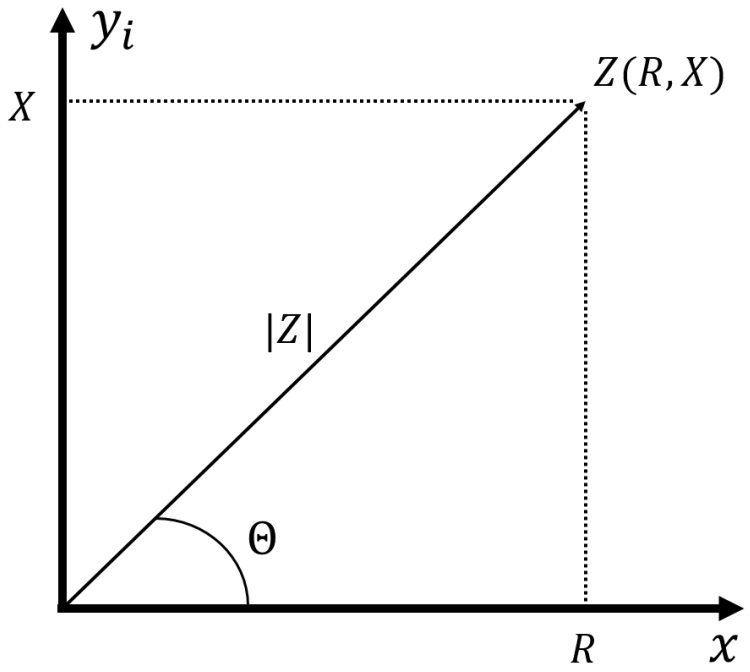

Figure 2.6: Representation of Impedance as a vector on the complex plane with a real component R and imaginary component X.

coordinates and polar form:

$$Z = R + jX, \tag{2.23}$$

where R and X are the real and imaginary components of the impedance vector,

$$Z = |Z| \angle \theta, \tag{2.24}$$

where $|Z|$ is the magnitude of the impedance vector and θ is the angle of the vector from the positive real axis. Given an AC applied signal, Ohm's law can then be expressed as

$$|V| = |Z||I|, \tag{2.25}$$

and the phase of the voltage signal will be shifted from the current signal by θ.

The rectangular form and polar form of the impedance are related as follows:

$$|Z| = \sqrt{R^2 + X^2}, \tag{2.26}$$

$$\theta = \arctan\left(\frac{X}{R}\right), \tag{2.27}$$

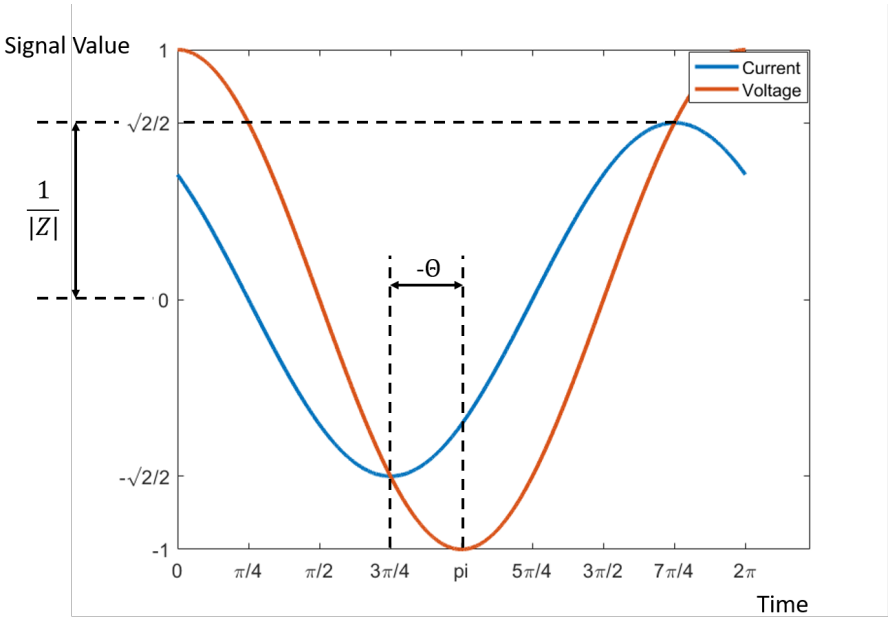

Figure 2.7: Current Response of a system to a 1 volt applied potential. Using equations 2.24 and 2.25, the impedance of the system can be expressed as $Z = \sqrt{2}\angle - \pi/4$.

$$R = |Z| \cos\theta, \tag{2.28}$$

$$X = |Z| \sin\theta. \tag{2.29}$$

The impedance of a system can be represented by a combination of elementary circuit components: resistors, capacitors, and inductors. The voltage response of these elements in the time domain can be expressed as

$$\text{Resistor:} \quad V = IR, \tag{2.30}$$

$$\text{Capacitor:} \quad V = C\frac{dV}{dt}, \tag{2.31}$$

$$\text{Inductor:} \quad V = L\frac{dI}{dt}, \tag{2.32}$$

where $V(t)$ and $I(t)$ are the voltage and current as a function of time, R is the resistance, C is the capacitance, and L is the inductance. After applying Laplace transforms, the frequency dependent impedance of each element can be obtained

as

$$\text{Resistor:} \quad Z(w) = R, \tag{2.33}$$

$$\text{Capacitor:} \quad Z(w) = \frac{1}{sC}, \tag{2.34}$$

$$\text{Inductor:} \quad Z(w) = sL, \tag{2.35}$$

where $s = jw$ for steady state solutions.

Impedance Spectroscopy: Coulter Counter

One of the first devices capable of measuring the electrical properties of particles is the Coulter counter, which measures the direct current resistance of two fluid filled chambers connected by an aperture (figure 2.8). The apparatus drives fluid through the aperture by a pressure differential caused by different levels of fluid in the two chambers. As particles flow through the aperture, conductive fluid is displaced and there is a change in resistance. Pulses of increased resistance mark particles flowing through the aperture, and the magnitude of the resistance pulse relates to the size of the particle.

In 1970, Deblois and Bean developed an analytical model of the Coulter counter resistance that can be related to dielectric properties of the particle [29]. The resistance of the large chambers were assumed to be negligible and the resistance of the aperture was derived (figure 2.9). For a tube of a mixture solution, the resistance can be expressed as

$$R_t = \frac{4\rho_{mix}L}{\pi d_t}G, \tag{2.36}$$

where G is a correction term for the non-uniform current density, R_t is the resistance of the tube, L is the length of the tube, d_t is the diameter of the tube, and ρ_{mix} is the resistivity of the mixture, which can be expressed using Maxwell's approximation,

$$\rho_{mix} = \rho_m\left[1 + \frac{3\phi}{2} + \left(\frac{-9\phi\rho_m}{4\rho_p + 2\rho_m}\right)\right], \tag{2.37}$$

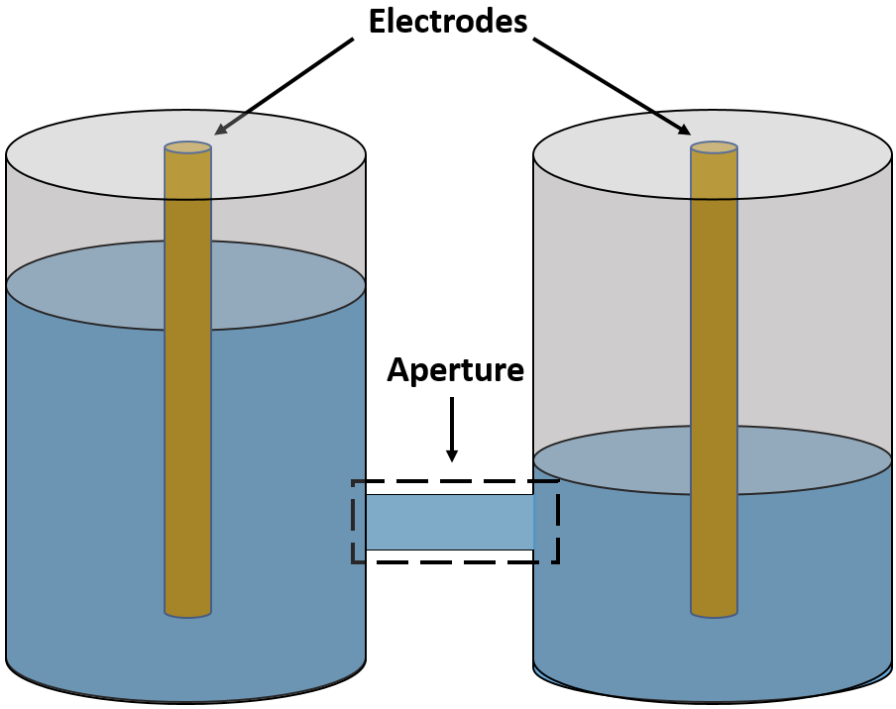

Figure 2.8: A Coulter counter that measures the DC resistance of the fluid in the chamber with two electrodes. When a particle enters the aperture, the change in resistance will provide information about the size and electrical properties of the particle

where ϕ is the volume fraction, ρ_m is the resistivity of the conductivity, and ρ_p is the resistivity of the particle. This approximation is only valid with the assumption that the particle diameter is small relative to the aperture. The volume fraction of a spherical particle in a tube is

$$\phi = \frac{2d_p^3}{3d_t^2 L}, \tag{2.38}$$

where d_p is the diameter of the particle.

Since 2000, Coulter counters have been fabricated on the micro scale and have allowed increased sensitivity and adaptability, leading to nanopore devices capable of analyzing single molecules [30].

Impedance Spectroscopy: Microfluidic Impedance Cytometry

Instead of electrodes on either side of an aperture, as in Coulter counter designs, microfluidic impedance cytometry designs electrodes directly onto the walls of the

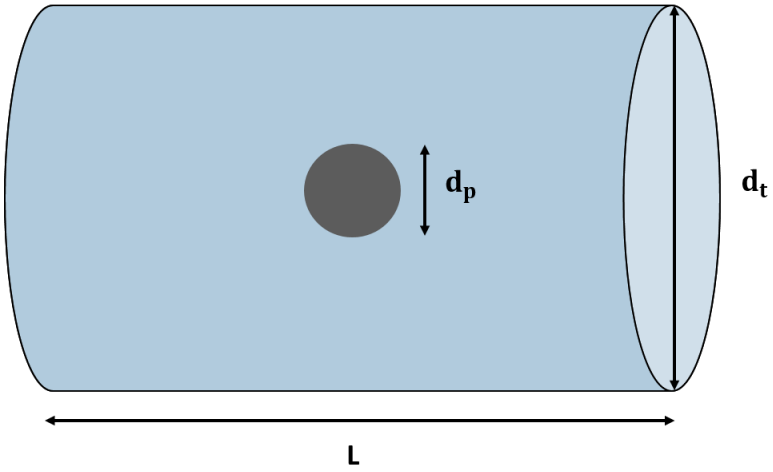

Figure 2.9: The aperture connecting the two chamber of the Coulter counter where L is the length of the aperture, d_p is the diameter of the particle flowing through the aperture, and d_t is the diameter of the aperture.

test volume. The test volume is the region that contains the particle and fluid with significant current density. The impedance of the test volume can be approximated as a leaky capacitor:

$$\tilde{Z}_{mix} = \frac{1}{jw\tilde{C}_{mix}}, \tag{2.39}$$

where $\tilde{C}_{mix}$ is the complex capacitance of the test volume, and can be expressed as

$$\tilde{C}_{mix} = \tilde{\epsilon}_{mix} G_f, \tag{2.40}$$

where $\tilde{\epsilon}_{mix}$ is the complex permittivity derived from Maxwell's mixture law and G_f is the geometric factor that accounts for fringing electric fields. Further details are provided in section 2.3.

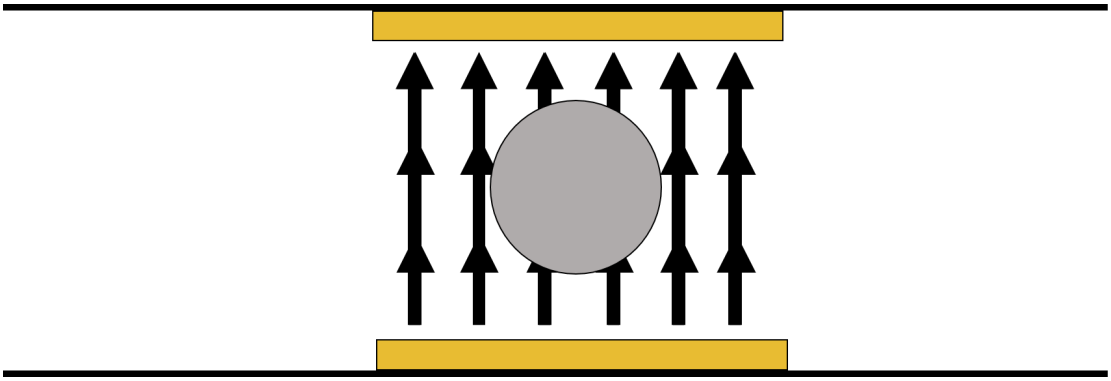

Figure 2.10: Parallel electrode configuration for impedance cytometry.

Common electrode configurations are parallel and coplanar facing (figure 2.10 and 2.11). Coplanar electrodes are easier to fabricate than parallel facing electrodes, but come at the cost of diminished sensitivity and accuracy [31]. Parallel electrode systems produce smaller variations in the electric field compared to coplanar electrodes. As a result, the signal variation is far greater for coplanar configurations. This results in a loss of accuracy, unless the vertical placement of the cell in the test volume can be controlled. In addition, parallel facing electrodes designs generally have larger volume fractions, and therefore, are more sensitive than coplanar electrodes. This can be observed by noting that given an electrode width, channel height, and channel depth, the coplanar test volume will be over twice that of parallel electrodes configurations.

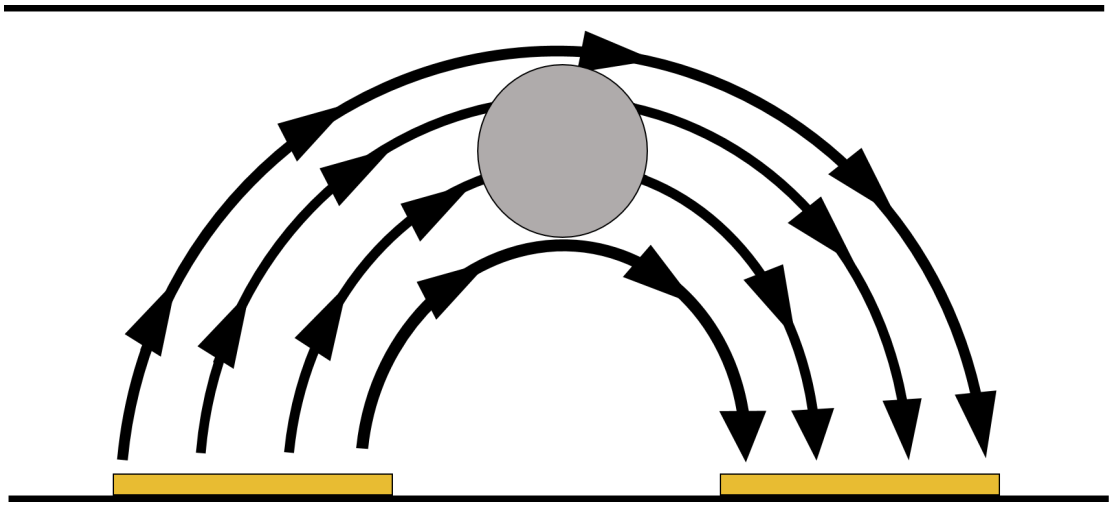

Figure 2.11: Coplanar electrode configuration for impedance cytometry.

In microfluidic impedance cytometry, alternating currents at a series of frequencies are applied to the system to measure the impedance response. From this impedance spectrum, the frequency dependent response can be depicted as magnitude-phase plots, real-imaginary plots, and nyquist plots in order to gain insight into the behaviour of the system (figure 2.12).

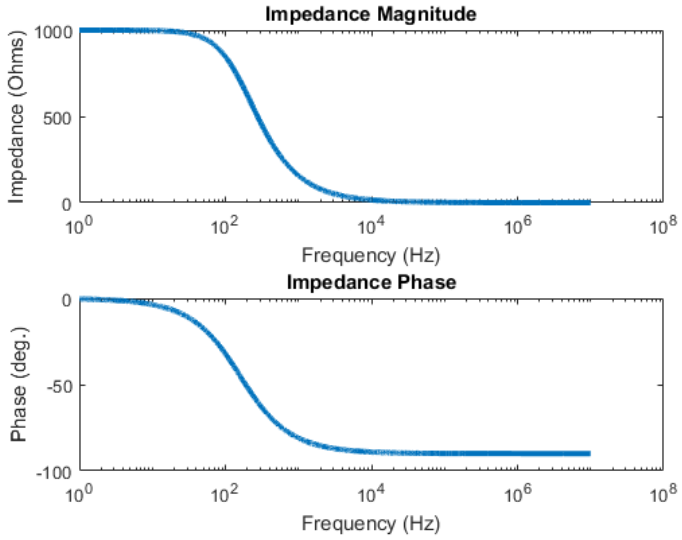

(a) Magnitude-phase versus frequency diagrams

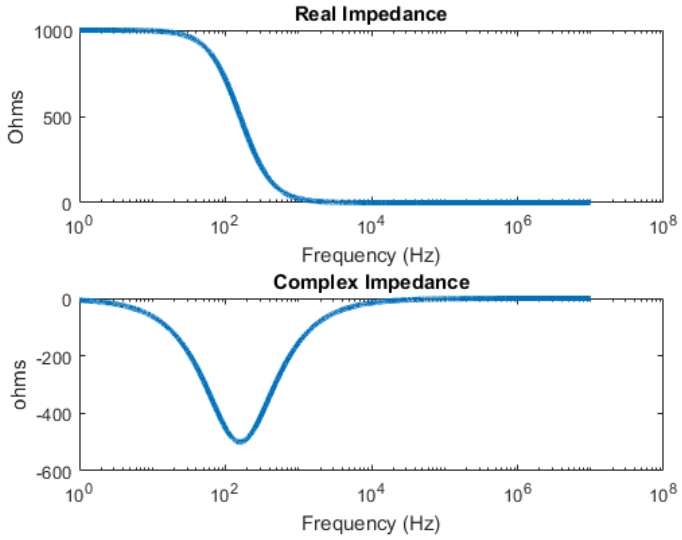

(b) Real-imaginary versus frequency diagrams

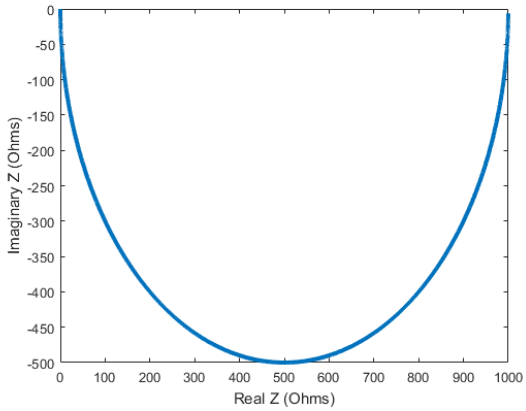

(c) Nyquist plot

Figure 2.12: Examples of magnitude-phase diagrams, real-complex diagrams, and a nyquist plot. The data is based off of the impedance of the circuit in figure 2.13.

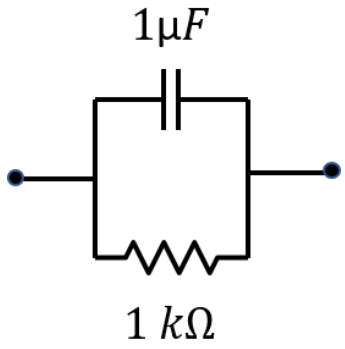

Figure 2.13: Example circuit used in impedance diagrams.

Circuit Implementation

The general process of impedance spectroscopy involves the application of a voltage or current signal, and the measurement of the signal response over a range of frequencies to obtain an impedance spectrum of the device under testing (DUT). The resulting spectrum provides insight into the dielectric properties of the DUT.

The simplest circuit for measuring impedance is based on the I-V method (figure 2.14). The I-V method determines the impedance of a DUT by measuring the voltage drop over the DUT and a high precision resistor in series. The current through the system can be calculated with Ohm's law at the high precision resistor. The impedance of the DUT for the I-V method can be expressed as

$$Z_{DUT} = \frac{\Delta V_{DUT}}{I} = \frac{V_1 - V_2}{V_2} R, \tag{2.41}$$

where V_1, V_2, and R correspond to values of elements in figure 2.14. An important disadvantage of this configuration, is that the accuracy of the impedance values relies on the precision of the resistor value, the extent of the parasitic capacitance in the system, and quality of the probes measuring $V1$ and $V2$ which can be challenged under a large DUT impedance and high frequencies. If the I-V method is used, coaxial cables will result in inaccuracies and should not be used.

Another circuit configuration to measure impedance is the auto-balancing bridge method (figure 2.15) [32]. The auto-balancing bridge method works as an extension

	Advantages	Disadvantages	Applicable frequency range
I-V method	– Grounded device measurement	–Operating frequency range is limited by probe	10 kHz to 100 MHz
Auto-balancing bridge method	– Wide coverage from low to high frequencies – High accuracy over a wide impedance measurement range – Grounded device measurement	– Not applicable to frequencies above 120 MHz	20 Hz to 120 MHz

Table 2.2: Common impedance measurement methods. [32]

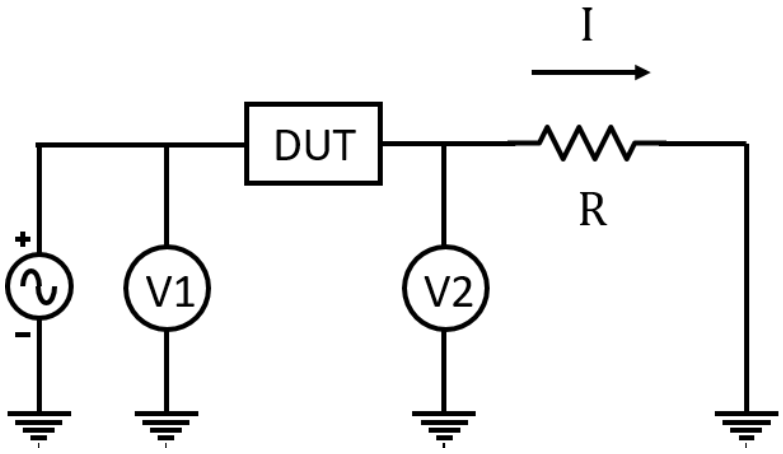

Figure 2.14: I-V impedance measurement.

of the I-V method. Instead of measuring the current directly, the potential on the low side of the DUT is driven to a virtual ground by an op-amp, and an equivalent current is measured. By applying Kirchoff's current law to the virtual ground node, the impedance of the DUT for using the auto-balancing bridge method can be expressed as

$$\frac{V_1}{Z_{DUT}} - \frac{V_2}{R} = 0, \tag{2.42}$$

$$Z_{DUT} = \frac{V_1}{V_2} R. \tag{2.43}$$

A significant advantage of the auto-balancing bridge method, is that when used with coaxial-grounded cables, the parasitic capacitance is removed from the measurement since all capacitances and measured elements are connected to ground.

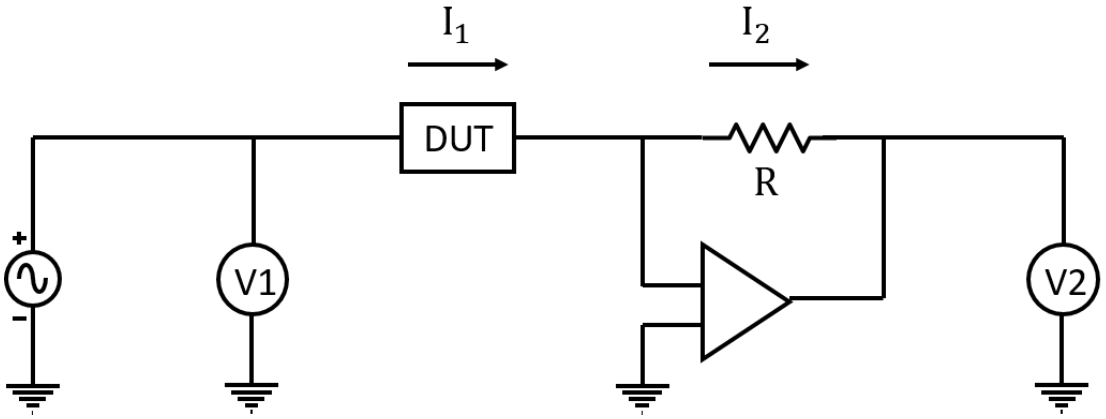

Figure 2.15: Auto-balancing bridge impedance method.

2.3 Theoretical Model of Impedance Cytometry

2.3.1 Maxwell's Mixture Theory

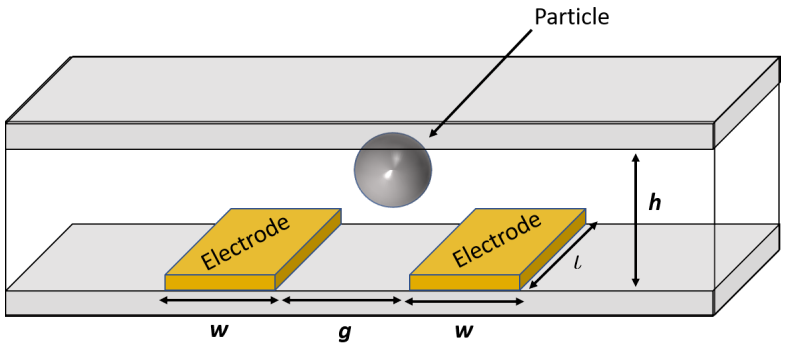

Figure 2.16: Diagram of the simplified impedance sensor chamber where w, g, and l are the width, gap, and length of the electrodes respectively, and h is the height of the chamber.

The impedance of a single cell suspension with low volume fractions (less than 10%), such as depicted in figure 2.16, can be solved for with Maxwell's mixture thoery [11], [30]. For high volume fraction suspensions, Hanai's theory should be considered [33]. In the case of single-cell impedance spectroscopy, the inherently low volume fraction of the suspension justifies the use of Maxwell's mixture theory. Maxwell's equation for the complex permittivity of a mixture is

$$\tilde{\epsilon}_{mix} = \tilde{\epsilon}_m \frac{1 + 2\Phi \tilde{f}_{CM}}{1 - \Phi \tilde{f}_{CM}}, \tag{2.44}$$

where $\tilde{\epsilon}_{mix}$ and $\tilde{\epsilon}_m$ are the complex permittivity of the mixture and medium respectively, $\tilde{f}_{CM}$ is the Clausius Mossotti factor, and Φ is the volume fraction. For most cases, the complex permittivity can be expressed as

$$\tilde{\epsilon} = \epsilon - j\frac{\sigma}{\omega}, \tag{2.45}$$

where ϵ is the permittivity, $j = \sqrt{-1}$, σ is the conductivity, and ω is the angular frequency. The Clausius Mossotti factor is defined as

$$\tilde{f}_{CM} = \frac{\tilde{\epsilon}_p - \tilde{\epsilon}_m}{\tilde{\epsilon}_p + 2\tilde{\epsilon}_m}, \tag{2.46}$$

where $\tilde{\epsilon}_p$ is the complex permittivity of the particle.

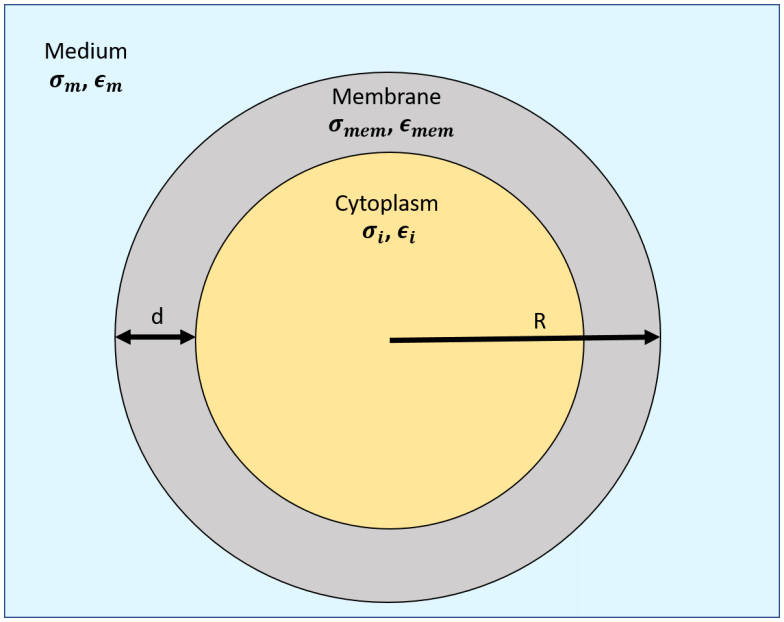

Figure 2.17: A diagram of a single shelled cell model where σ is the conductivity, ϵ is the permittivity, and the subscripts m and i denote the membrane and cytoplasm respectively. R and d are the radius of the cell and membrane thickness respectively.

The permittivity of the single-shelled cell in figure 2.17, can be modelled as

$$\tilde{\epsilon}_p = \tilde{\epsilon}_{mem}\frac{\gamma^3 + 2(\frac{\tilde{\epsilon}_i - \tilde{\epsilon}_{mem}}{\tilde{\epsilon}_i + 2\tilde{\epsilon}_{mem}})}{\gamma^3 - (\frac{\tilde{\epsilon}_i - \tilde{\epsilon}_{mem}}{\tilde{\epsilon}_i + 2\tilde{\epsilon}_{mem}})} \quad \text{with } \gamma = \frac{R+d}{R}, \tag{2.47}$$

where $\tilde{\epsilon}_i$ is the complex permittivity of the cytoplasm, $\tilde{\epsilon}_{mem}$ is the complex permittivity

of the cell membrane, R is the radius of the cell, and d is the thickness of the cell membrane.

The impedance of the mixture is

$$\tilde{Z}_{mix} = \frac{1}{jw\tilde{C}_{mix}}, \tag{2.48}$$

where w is the angular frequency and $\tilde{C}_{mix}$ is the complex capacitance of the mixture which can be expressed as

$$\tilde{C}_{mix} = \tilde{\epsilon}_{mix} G_f. \tag{2.49}$$

If equations 2.48 and 2.49 are combined, we obtain

$$\tilde{Z}_{mix} = \frac{1}{jw\tilde{\epsilon}_{mix} G_f}. \tag{2.50}$$

To find the value of the geometric factor G_f, the cell constant of electrodes must be determined.

2.3.2 Electrode Cell Constant

The cell constant κ is defined as the proportionality factor between the measured resistance R_b and the resistivity ρ of a material:

$$R_b = \kappa\rho. \tag{2.51}$$

Olthius related the measured resistance to capacitance in order to derive an analytic solution to the cell constant [34].

To find R_b for two electrodes with an interspatial material, the measured resistance can be related to capacitance via Ohm's law and Maxwell's equation:

$$RC = \frac{\oiint \epsilon \boldsymbol{E} \cdot d\boldsymbol{S}}{\oiint \sigma \boldsymbol{E} \cdot d\boldsymbol{S}}, \tag{2.52}$$

where R and C are the resistance and capacitance between the electrodes, ϵ is the product of the relative and vacuum permittivity, $\boldsymbol{E}$ is the electric field vector, and the integral is taken over a surface including one electrode.

If the interspatial material is homogeneous and isotropic, then equation 2.52 can be reduced to

$$RC = \frac{\epsilon}{\sigma}. \tag{2.53}$$

If we take $R_b = R$, we can combine equation 2.53 and 2.51 to express the cell constant in terms of capacitance:

$$\kappa = \frac{\epsilon}{C}. \tag{2.54}$$

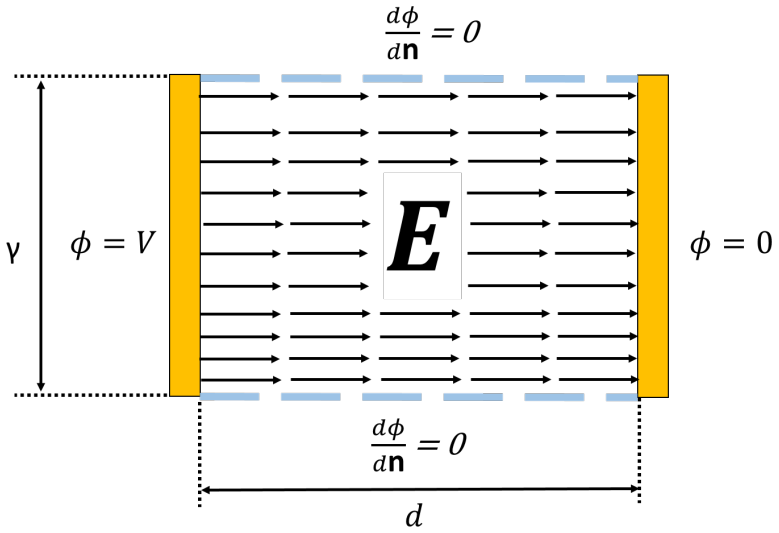

Figure 2.18: Uniform electric field between two parallel electrodes where $\boldsymbol{E}$ is the electric field, ϕ is the voltage, and $\frac{d\phi}{d\boldsymbol{n}} = 0$ is the boundary condition of a perfect insulator. The dimensions of the capacitor are the electrode height γ, and the distance between the electrodes d.

The capacitance of the two parallel plates with a uniform electrode field in figure 2.18 is

$$C = \frac{\epsilon A}{d}, \tag{2.55}$$

where A the area of the plate, and d is the distance between the plates. Since $A = l\gamma$, where l is the width, and γ is the height of the electrode, the capacitance

per unit width can be written as

$$C_l = \frac{\epsilon\gamma}{d} \quad \text{where} \quad C = l\,C_l. \tag{2.56}$$

Returning to equation 2.54, and substituting equation 2.56, the cell constant can be expressed as

$$\kappa = \frac{d}{\gamma\,l}. \tag{2.57}$$

The geometric factor is the inverse of the cell constant

$$G_f = (\kappa)^{-1}, \tag{2.58}$$

and can be expressed as

$$G_f = \frac{\gamma l}{d}. \tag{2.59}$$

Equation 2.59 is the solution of the geometric constant for the electrode configuration in figure 2.18, but to find the geometric constant for any other configuration, including the coplanar electrode in figure 2.16, d and γ will need to be mapped to the other configuration. This can be accomplished with conformal transformations.

2.3.3 Conformal Transformations

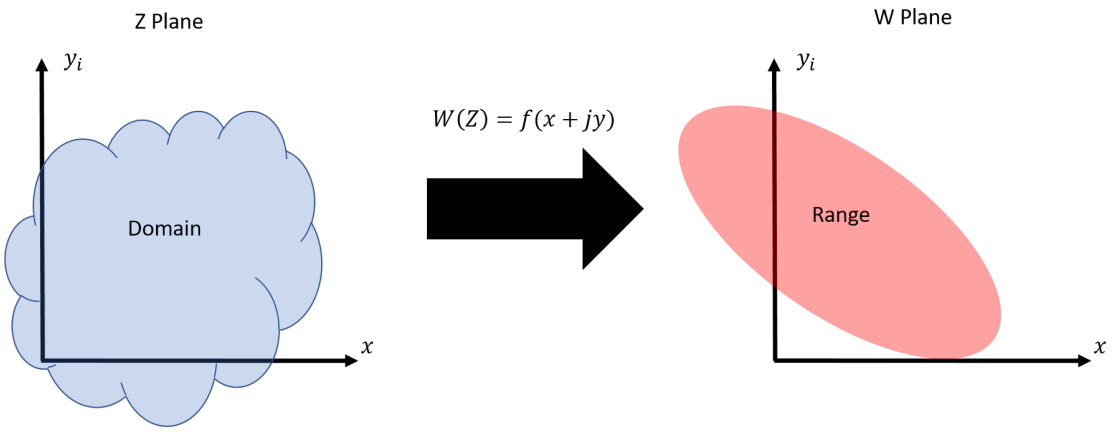

Figure 2.19: An Illustration of complex mapping.

Let $z = x + j\,y$, where j is the imaginary number $\sqrt{-1}$, then a function of z,

such as $W(z) = u(x, y) + j\, v(x, y)$, can be considered a mapping of an area of one complex plane to an area in another complex plane (figure 2.19). Conformal transformations are a special kind of mapping between two complex planes that preserves local angles. A mapping is conformal if it is composed of analytic functions, and as a consequence, fulfills the Cauchy-Rieman equations. Conformal mappings are extremely useful for solving complicated problems by mapping the problem to a simplified domain. An example of a conformal mapping is $w(z) = tan(z)$, which maps an infinite vertical strip to a circle (figure 2.20).

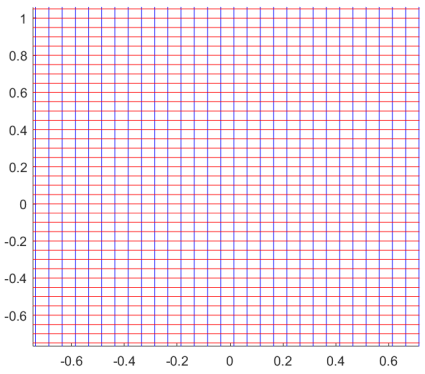

(a) Part of the partial infinite strip $-\pi/4 < x < \pi/4$.

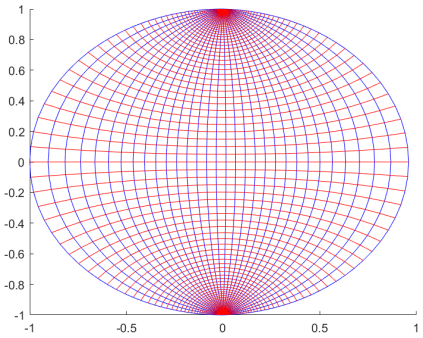

(b) Mapping of the partial infinite vertical strip to a circle

Figure 2.20: An example of conformal mapping by transforming a partial infinite vertical strip to a circle with the mapping $w(z) = tan(z)$.

Sun, Greene, et al. utilized the Schwartz-Christoffel transform to map the coplanar electrode configuration in figure 2.16 to the configuration of parallel electrodes with uniform electrode fields in figure 2.18 [31]. The Schwartz-Christoffel formula is a powerful transform that allows the mapping of the upper complex T-plane ($y > 0$) to the inside of a polygon. The formula is

$$Z = C_1 \int_{T_0}^{T} \prod_{r=1}^{m} (T - T_r)^{(\theta_r/\pi - 1)} dT + C_2, \tag{2.60}$$

where Z is the interior of a polygon in the Z-plane with vertices $Z_1,\ Z_2,\ Z_3,\ ..., Z_m$ and angles $\theta_1,\ \theta_2,\ \theta_3,\ ..., \theta_m$ which correspond to the points $T_1,\ T_2,\ T_3,\ ..., T_m$ on the real axis of the T-plane. C_1 and C_2 are integration constants. The Schwartz-

Christoffel transform has three degrees of freedom, and consequently, up to three points may be chosen arbitrarily. T_0 is the reference and is typically chosen at the origin.

The solution and application of the Schwartz-Christoffel transform to co-planar electrodes will be further explored in chapter 4.

2.3.4 Cell Suspension Equivalent Circuit

With a solution to the impedance of the system, an equivalent circuit of the cell and medium can be used to approximate discrete components. A simple equivalent circuit was described by Foster and Schwan that describes the cell as a capacitor and resistor in series (figure 2.21) [19]. The model assumes that the resistance of the cell membrane is far greater than its reactance and can be expressed as a capacitor. Similarly, it is assumed that the cytoplasm resistance is far greater than its capacitance and can be modeled as a resistor.

The values of the simplified circuit model are as follow [22]:

$$R_m = \frac{1}{\sigma_m(1 - 3\Phi/2)G_f}, \tag{2.61}$$

$$C_m = \epsilon_\infty G_f, \tag{2.62}$$

$$C_{mem} = \frac{9\Phi R C_{mem,0}}{4} G_f, \tag{2.63}$$

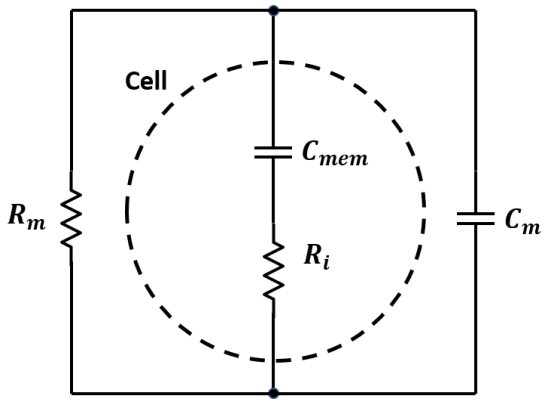

Figure 2.21: Simple equivalent circuit of cell and medium.

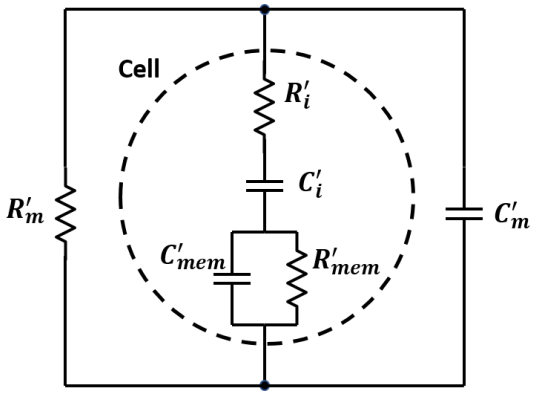

Figure 2.22: Complete equivalent circuit of cell and medium.

$$R_i = \frac{4\left(\frac{1}{2\sigma_m} + \frac{1}{\sigma_i}\right)}{9\Phi G_f}, \tag{2.64}$$

where σ_m and σ_i are the conductivities of the medium and cytoplasm respectively, R is the cell radius, Φ is the volume fraction, and $C_{mem,0}$ is the specific membrane capacitance and can be expressed as [30]

$$C_{mem,0} = \epsilon_{mem}/d, \tag{2.65}$$

where ϵ_{mem} is the permittivity of the cell membrane and d is the thickness of the membrane. ϵ_∞ is the high frequency permittivity of the suspension and can be approximated as

$$\epsilon_\infty \approx \epsilon_m \left[1 - 3\Phi \frac{\epsilon_m - \epsilon_i}{2\epsilon_m + \epsilon_i}\right]. \tag{2.66}$$

For cases where the cytoplasm reactance and membrane resistance are significant, such as during cell lysis, the complete equivalent circuit can be used (2.22) [30]. A quantitative description of the model is described by Sun et al. [35].

2.4 MEMS and Microfluidics

Microelectromechanical systems (MEMS) are devices on the order of microns, and are often smaller than the diameter of a human hair (about 100 microns). MEMS evolved from the manufacturing processes used to fabricate integrated circuits and ink jet cartridges [36]. Using silicon based microfabrication techniques such as

photolithography, etching, and metal deposition; mechanical and electrically driven micro-sized pumps, cantilevers, and sensors can be fabricated [37].

Using these microfabrication techniques, systems can be miniturized in precise and reproduceable packages with applications in a variety of biology related problems. MEMS applied in these fields are referred to as BioMEMS. The majority of BioMEMS are focused on creating diagnostic systems that can identify diseases and properties of biogical substances. These devices usually need to treat, filter, and utilize detection methods that include electrophoresis, dielectrophoresis, surface plasmon resonance, and enzyme-linked immunosorbent assays (ELISA) [38]. In order to run diagnostics on a solution of biological material, a sample needs to undergo pretreatment, sample preparation, preconcentration, and detection. With the miniaturization afforded by microfabrication technology, the concept of combining these steps into a single chip is now feasible. These devices are referred to as labs on a chip or micro total analysis systems. This thesis focuses on the detection method of such a device.

2.4.1 MEMS Fabrication

Photolithography

Photolithography is a MEMS fabrication method that patterns a thin layer of photoresist onto a substrate. Photoresist is a polymer that reacts to certain wavelengths of light. How the photoresist reacts determines whether the photoresist is classified as a positive or negative photoresist. Positive photoresist becomes soluble to a developer after exposure to light, and negative photoresist becomes cross-linked and insoluble to the developer after exposure.

Photoresist can be applied to a substrate with a precise thickness through application of a spinner machine. The machine spins the substrate at given rotation velocities to evenly distribute the photoresist and precisely control the thickness.

The photoresist can then be exposed to ultra violet light. In order to apply a design to the surface, a contact aligner can be used to expose the substrate under

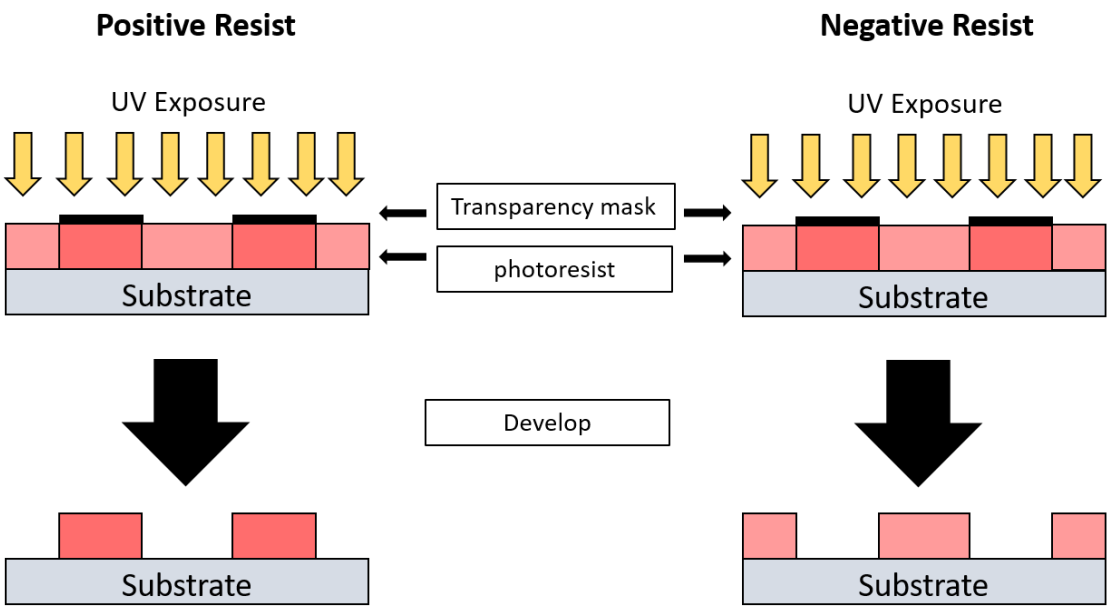

Figure 2.23: A comparison of positive and negative photoresist. For positive photoresist, exposed regions are removed, and for negative photoresist, unexposed regions are removed.

a mask. The mask is a transparency sheet with the design printed on it. The mask controls where light is allowed and the contact aligner controls the distance between the mask and the photoresist. The resist is then developed to reveal the patterned design.

Soft-lithography

Soft-lithography uses photolithography to create a mold of the desired structures. A material such as polydimethyl siloxane (PDMS) can be cast on the mold and then removed to create the desired structure. The PDMS can be plasma bonded to a substrate to create fluid channels. Soft-lithography is frequently used for the fabrication of microfluidic channels since the process is far easier and cheaper than the alternative of glass etching [39].

Metal Deposition

One of several methods for MEMS metal deposition is sputtering. Sputtering ejects metal ions onto the target surface. The target substrate is placed on the anode

with the desired metal used as the cathode. An argon plasma bombards the metal plate and ejects metal ions that are attracted to the anode and deposit on the target substrate.

Lift-off Process

The lift-off process is a method for precise metal deposition of a pattern onto a substrate and is useful for creating micro-scale electrodes. Photolithography is first used to pattern photoresist where metal is not desired. After metal deposition of the substrate with patterned photoresist, the sputtered substrate is then placed in photoresist remover to lift off the photoresist with the undesired metal.

Plasma Bonding

To irreversibly bond PDMS, the surface can be exposed to an air plasma. The plasma activates the PDMS surface by creating Si-OH groups that can bond to itself, glass, silicon, polystyrene, polyethylene, and silicon nitride [40].

2.4.2 Microfluidics

In most BioMEMS there is fluid flow on the micrometer scale. At this scale fluid flow physics differ from fluid flow at the macro scale. Understanding and leveraging microfluidic mechanics allows for small reagent and sample volumes, multiplexing, and physic phenomenon that allow experiments and functions not possible at the macro scale. Laminar flow, diffusion, fluidic resistance, surface area to volume, and surface tension, may not be dominant in phenomenon on the macro scale, but on the micro scale become significant [41]. Microfluidics are discussed in further detail in appendix A.

2.5 The Electric Double Layer

When electric fields are applied to ionic solutions, the electrodes will attract ions of opposite charge. With equilibrium to thermal forces, the applied field will result in the

electric double layer (figure 2.24) [42]. The electric double layer creates an effective capacitance at the electrode-fluid interface. For electrodes with large surface areas, the capacitance may be large enough to be negligible, but for MEMS with micro-scale electrodes, the capacitance will be small and can mask the impedance of the device under testing for frequencies up to 100 kHz to 1 MHz [43].

2.5.1 Theoretical Capacitance

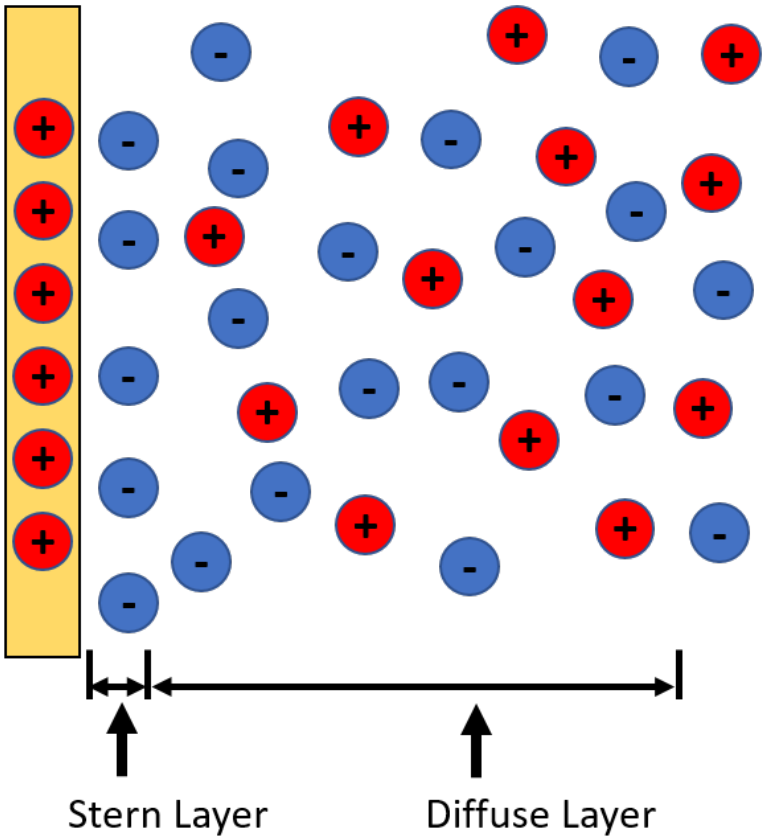

Figure 2.24: The Stern model of the electric double layer that includes the Helmholtz and diffuse layers.

Helmholtz was the first to describe the electric double layer and modeled it as a single layer of ions adsorbed to the surface of the electrode [42]. If the ions are treated as point charges, the Helmholtz model can be interpreted as a parallel capacitor with a distance d_H between the plates that represents the distance between the center of the ion and the surface of the electrode. The capacitance per unit area can be approximated as

$$C = \frac{\epsilon_o \epsilon_r}{d_H}, \tag{2.67}$$

where ϵ_o is the permittivity of the vacuum, ϵ_r is the relative permittivity of the medium, and d_H is the thickness of the Helmholtz layer [44]. The Helmholtz model neglects the thermal, concentration, and voltage dependencies that experiments have confirmed [45].

Guoy and Chapman expanded on the electric double layer by including the effects of thermal motion, concentration, and applied voltage [44], [46]. This results in a diffuse layer that consists of counter-ions and co-ions. The distribution of ions in the diffuse layer can be described by the Boltzmann distribution:

$$n_{i\pm} = n_i^o \exp\Big(\frac{\mp z_i e\phi}{k_b T}\Big), \tag{2.68}$$

where n_i is the concentration of the ion i, ϕ is the electric potential, T is the temperature, k_b is the Boltzmann constant, z_i is the charge number of the ion, and e is the charge of an electron. The charge density can be written as the sum of all ions:

$$\rho(x) = e\sum_i n_i^o z_i \exp\Big(\frac{-z_i e\phi}{k_b T}\Big). \tag{2.69}$$

Combining Poisson's equation with the charge distribution above, results in the Poisson-Boltzmann equation:

$$\nabla^2\phi = \frac{e}{\epsilon_o \epsilon_r}\sum_i n_i^o z_i \exp\Big(\frac{-z_i e\phi}{k_b T}\Big), \tag{2.70}$$

and then recognizing that

$$\frac{d^2\phi}{dx^2} = \frac{1}{2}\frac{d}{dx}\Big(\frac{d\phi}{dx}\Big)^2, \tag{2.71}$$

then with the boundary condition for electrodes far apart, $\phi \to 0$ and $\frac{d\phi}{dx} \to 0$ as

$x \to \infty$, equation 2.70 can be integrated to

$$\Big(\frac{d\phi}{dx}\Big)^2 = \frac{2k_bT}{\epsilon_o\epsilon_r}\sum n_i^o\Big[exp\Big(\frac{-z_ie\phi}{k_bT}\Big) - 1\Big]. \tag{2.72}$$

For a symmetrical electrolyte, the Poisson-Boltzmann equation can be expressed as

$$\frac{d\phi}{dx} = \frac{8k_bTn^o}{\epsilon_o\epsilon_r}\sinh\Big(\frac{ze\phi}{2k_bT}\Big). \tag{2.73}$$

Capacitance can generally be defined as the differential capacitance:

$$C_{diff} = \frac{d\sigma}{d\phi_o} \tag{2.74}$$

where σ is the surface charge of the electrode and ϕ_o is the electric surface potential. From Gauss's law and equation 2.73, the charge for the electric double layer is

$$\sigma = \epsilon_o\epsilon_r\Big[\frac{d\phi}{dx}\Big]_{x=0} = \sqrt{8k_bTn_i^o\epsilon_o\epsilon_r}\sinh\Big(\frac{ze\phi_o}{2k_bT}\Big). \tag{2.75}$$

Differentiating 2.75 with respect to surface potential gives the differential capacitance of the electric double layer:

$$C_{GC} = \Big(\frac{2z^2e^2n_i^o\epsilon_r\epsilon_o}{k_bT}\Big)\cosh\Big(\frac{ze\phi_o}{2k_bT}\Big). \tag{2.76}$$

Stern combined the Helmholtz and the Guoy-Chapman thoeries to create a model with two layers: the inner layer known as the Stern layer, which consists of the adsorbed ions on the electrode surface from the Helmholtz model, and the outer diffuse layer (figure 2.24 [45]. The capacitance of the Stern model can be approximated by the capacitance of the Helmholtz and Guoy-Chapman models in series [44]:

$$C_s = \left[\frac{1}{C_H} + \frac{1}{C_{GC}}\right]^{-1}. \tag{2.77}$$

Unfortunately, these models do not fully describe the electric double layer and

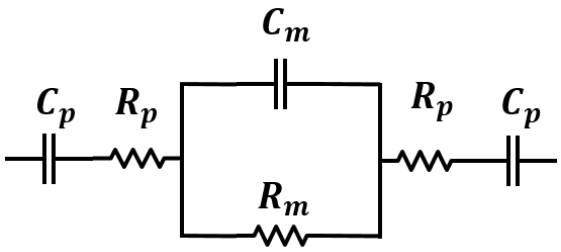

Figure 2.25: A series resistor and capacitor equivalent circuit of the electric double layer.

significantly overestimates the electric double layer capacitance. Gongadze et al. measured the capacitance of the electric double layer in a phosphate-buffered electrolyte solution with titanium electrodes. Using theory, the electric double layer capacitance was calculated as 231.7 μF/cm^2, 77.16 μF/cm^2, and 57.92 μF/cm^2 for the Helmholtz, Guoy-Chapman, and Stern model respectively, but the experimental capacitance was 6 μF/cm^2 [44]. Predicting the electric double layer is convoluted by the surface properties of the electrodes, electrochemical reactions, and other non-quantified phenomena in the solution.

2.5.2 Correction for the Electric Double Layer

To overcome the theoretical shortcomings, devices can be designed to minimize the effect of the electric double layer and/or an empirical corrective function can be applied to data. Physical compensations include four electrode sample cells, increasing the surface area by coating the electrode in black platinum or polypyrrole polystyrenesulphonate, and high current density methods [42]. However, due to a combination of device constraints, difficulty in implementation, reduced electrode strength, and failure to completely bypass the electric double layer, physical compensations are usually avoided [47].

Empirical recalculations involve fitting a reference measurement to a function or equivalent circuit. One of the more common equivalent circuit models of the electric double layer is a resistor and capacitor in series (figure 2.25) [48]. The impedance

of the system can be expressed as

$$Z = 2Z_p + Z_m, \tag{2.78}$$

$$Z_p = \frac{1 + sC_pR_p}{sC_p}, \tag{2.79}$$

$$Z_m = \frac{R_m}{sC_mR_m + 1}, \tag{2.80}$$

where Z_p, C_p, and R_p are the impedance, capacitance, and resistance of the electric double layer respectively; and Z_m, C_m, and R_m are the impedance, capacitance, and resistance of the medium respectively. s is the Laplace variable, and since our interest is in the steady state behaviour, $s = jw$.

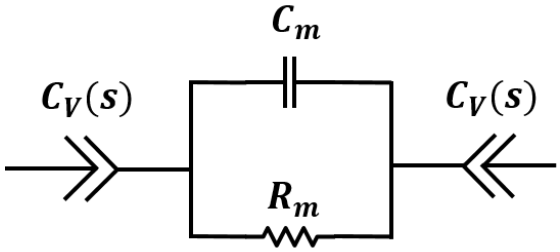

Figure 2.26: A recap equivalent circuit of the electric double layer.

A second equivalent circuit involves a similar system, but with the inclusion of recap elements (figure 2.26) [49]. A recap element can be modeled as

$$C_v = R(RC)^{-v}s^{-v}, \tag{2.81}$$

where C is capacitance, R is resistance, and v is $0 < v < 1$. v determines the degree of capacitance or resistance behavior, with $v = 1$ a complete capacitor, and $v = 0$ a pure resistor. The recap element is known as a type of constant phase element (CPE), which is named after its property of contributing a constant angle and describes an imperfect dielectric. Constant phase elements are found in a wide range of electrodes and are used extensively in empirical descriptions of electrode polarization [42]. To fit data to the CPE, it is useful to express the system impedance

as

$$Z_{sys} = Z_{bulk} + Z_0 \left(j \frac{f}{f_0} \right)^{-v}, \tag{2.82}$$

where Z_{bulk} is the impedance of the medium, j is the imaginary number, f is frequency, f_0 is the onset frequency of the electrode polarization, and Z_0 is a impedance fitting term. It is convenient to find the onset frequency by looking for the characteristic tail of the CPE on a nyquist plot [47].

Chapter 3: Methods

3.1 Device Manufacturing

3.1.1 PDMS Channel Fabrication

The device microchannels were fabricated by pouring polydimethysiloxane (PDMS) over a silicon wafer master mold. Through photolithography, a master mold was created by patterning a silicon wafer with SU-8 photoresist in a process known as soft lithography. A 6"x6" 20,000 DPI negative transparency mask was ordered from CAD/Art Services Inc. with the emulsion face down. A general process flow is depicted in figure 3.1.

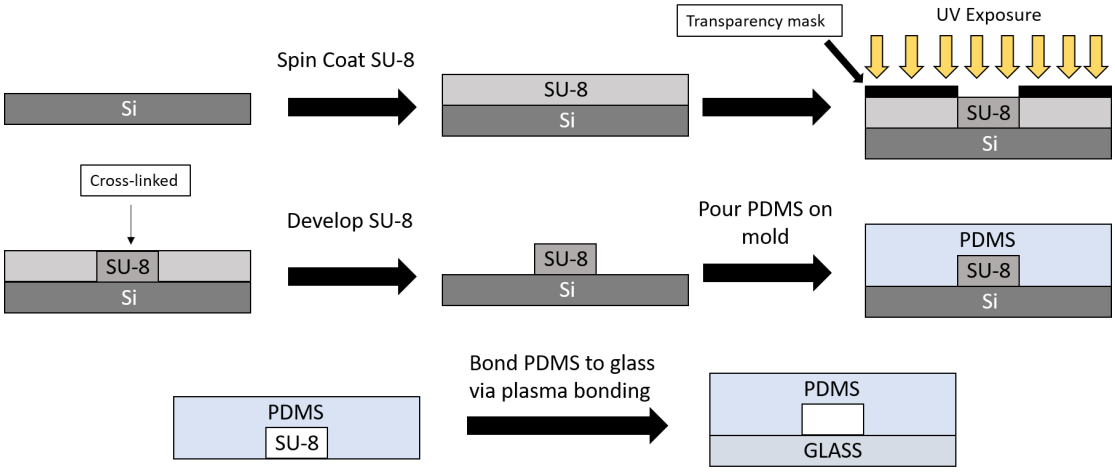

Figure 3.1: Micro-channel manufacturing flowchart with SU-8 photoresist and soft-lithography.

SU-8 Master Mold

Before photolithography, silicon wafers were cleaned in a piranha bath (mixture of sulfuric acid and hydrogen peroxide) for 15 minutes with a deionized (DI) water rinse, and dipped in a BOE solution (buffered oxide etchant; mixture of buffer and concentrated hydrofluoric acid) for 5 minutes with another DI rinse. The wafers were washed and dried in the SRD (spin rinse dry) machine. The wafers were baked at

205°C for 10 minutes and allowed to cool for 10 minutes. This dehydration bake ensured that moisture was evaporated from the silicon surface.

Figure 3.2: Laurel Technologiers ws-400 spin coater.

The wafers were coated with SU-8 (negative tone photoresist) on a spin coater (Laurel Technologies, ws-400; figure 3.2). The spin coater rotates at a series of angular velocities in order to coat the wafer with the desired thickness of photoresist. About 4 mL of SU-8 2007 (#07110769, MicroChem) was placed on the center of the wafer, spun at 400 RPM for 20 seconds to disperse the SU-8, and then at 1500 RPM for 35 seconds to spread the photoresist to a 10 μm thickness. After spin-coating, the wafer was soft-baked at 85°C for 3 minutes and allowed to cool for 4 minutes.

The photolithography process was completed using the Cannon PLA-501FA mask aligner (figure 3.3). With the transparency mask centered over the wafer and the 365 nm glass-transparency filter in place, UV light was applied to the photoresist for 14 seconds with a total exposure of 140 mJ/cm^2. The wafer was baked at 85 °C for 4 minutes with a 10 minute cool down.

Figure 3.3: Cannon PLA501FA mask aligner.

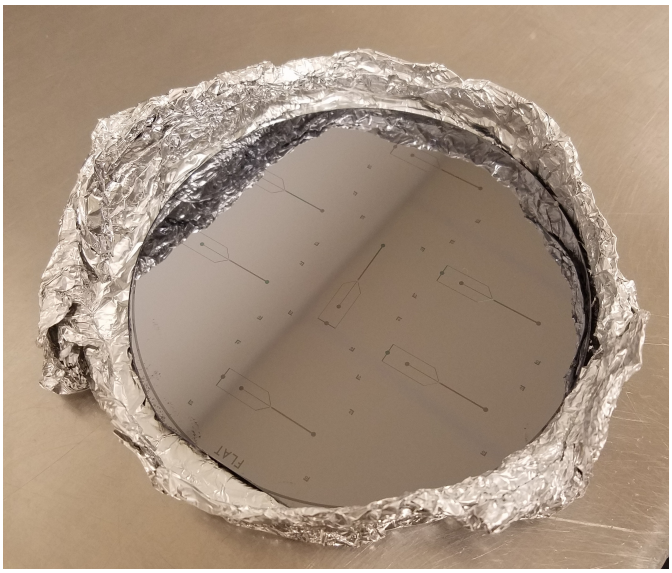

Figure 3.4: SU-8 master mold.

The wafer was developed in propylene glycol monomethyl ether acetate (SU-8 developer, MicroChem) in order to remove the non-exposed SU-8 from the wafer. The wafer was placed in the SU-8 developer for 3 minutes and hard baked for 15 minutes at 210°C. The result was a SU-8 patterned silicon wafer mold (figure 3.4).

Soft Lithography

The Dow Corning 184 Sylgard kit was purchased through Ellsworth adhesives for the PDMS supply. The kit comes with a base and a curing agent that cross-links the PDMS and increases the polymer's stiffness. The PDMS was prepared by mixing the base and the curing agent at a 10:1 ratio. The mixture was degassed under vacuum until the PDMS was free of bubbles (figure 3.5). The PDMS was then poured directly onto the SU-8 master mold until the PDMS covered the wafer with approximately 1/4" of depth. The PDMS-covered master mold was baked at 65°C for at least an hour in order to cure the PDMS. The PDMS chips were cut from the master mold with a scalpel and peeled off the wafer.

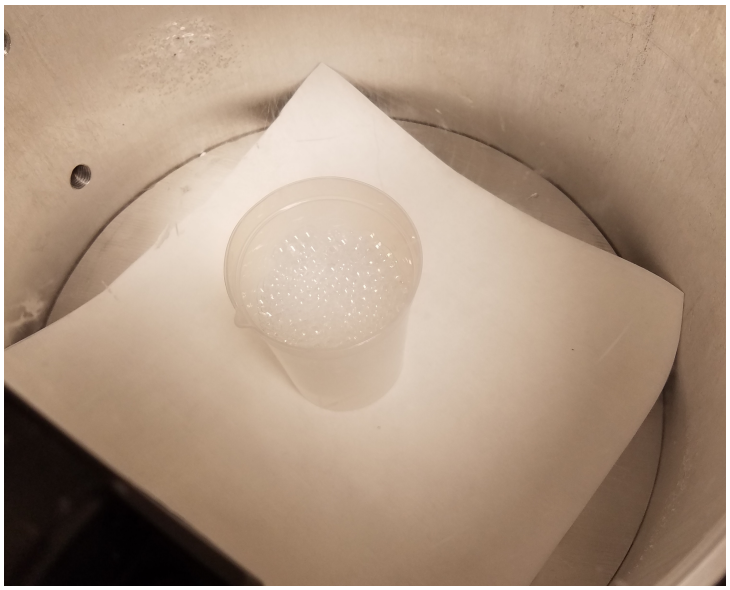

Figure 3.5: Degassing PDMS mixture under vacuum.

The finished product was a PDMS chip with the desired microchannel dimensions molded into the polymer surface.

3.1.2 Electrode Fabrication

The device electrodes were fabricated onto a glass substrate using the lift-off process (section 2.4.1). The process utilized a 6"x6", 20,000 DPI transparency mask ordered from CAD/art services Inc. A flow chart of the overall process is depicted in figure 3.6.

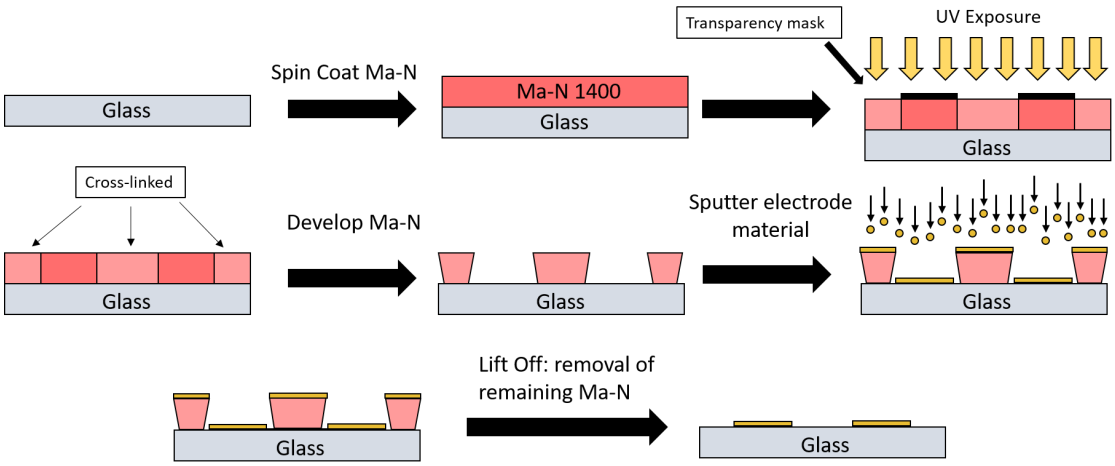

Figure 3.6: Electrode fabrication flowchart through the lift off-process.

Photolithography

Glass wafers were prepared for the lift-off process by cleaning the wafers in a pirahna bath for 15 minutes with a DI rinse, and a 1 minute dip in BOE with another DI rinse before running the wafers through the SRD. The wafers were dehydrated by baking on a hot plate for 10 minutes at 200 °C and allowed to cool for five minutes.

The wafers were coated with ma-N1420 negative-tone photoresist on a spin coater (Laurel technologies, ws-400; figure 3.2). The ma-N1420 photoresist is advantageous for the lift-off process since the developed photoresist has an undercut profile, and the cross-linked property of the negative photoresist is more durable than the "soft" positive photoresist. Before application of the ma-N1420, a primer was dispersed and then spun onto the wafer at 3000 RPM for 30 seconds to increase photoresist adhesion. Ma-N1420 was then dispersed onto the glass wafer, but before spinning, it was ensured that the photoresist spread to all edges of the wafer. The photoresist was spun at 2000 RPM for 35 seconds with a target of 2.5 micron thickness. The wafers were then soft-baked on a hotplate at 120°C for 3 minutes to increase stability.

The photolithography process was completed using the Cannon PLA-501FA mask aligner (figure 3.3). The glass wafer was placed in the aligner with a black tape backing in order to prevent light scattering and absorb radiation. UV light was

applied to the wafer for 30 seconds for a total of 450 mJ/cm^2.

The wafer was then developed for 60-90 seconds in ma-D 533/3 developer and rinsed in DI water. At this step, the wafer was examined under a microscope to ensure the photoresist was fully developed with sharp patterns (figure 3.7). If not, the wafer was developed for another 10 seconds and reexamined.

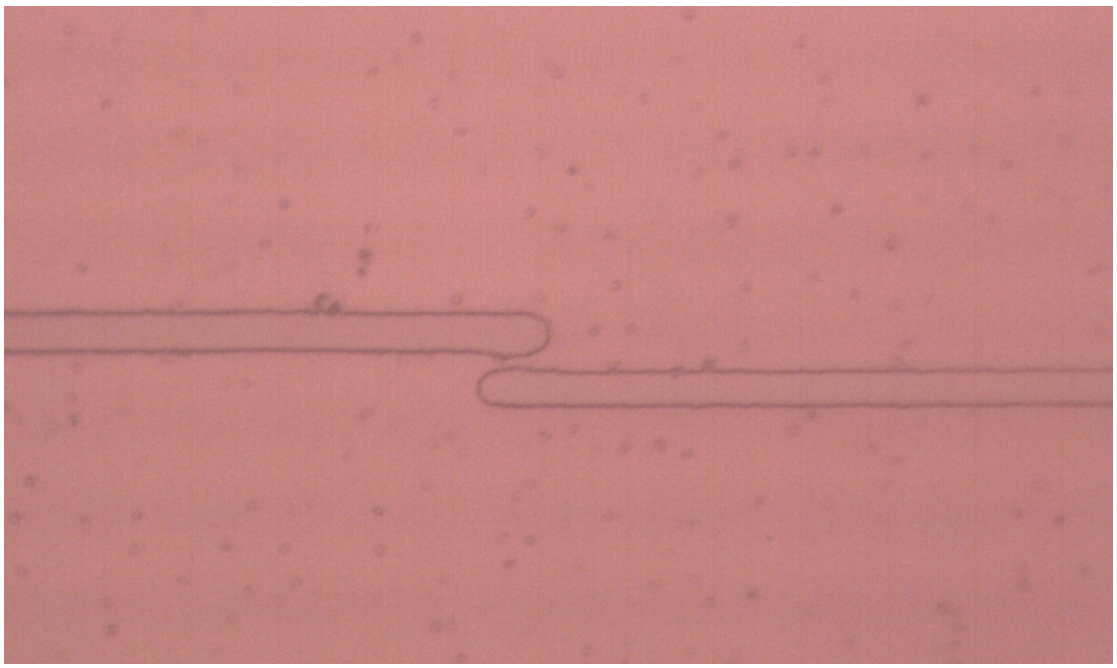

Figure 3.7: Post-developed Ma-N1420 photoresist. The two outlined areas depict areas of removed photoresist.

After the photoresist was fully developed, the wafer was flood-exposed (i.e. no transparency) in order to improve stability. The photoresist was exposed 3 times for 40 seconds with a five minute rest between each exposure for a total of 1800 mJ/cm^2. Finally, the wafers were baked on the hotplate with a ramping temperature from 60 °C to 100 °C for 10 minutes and allowed to cool for 10 minutes.

Metal Deposition

To deposit the electrode metals onto the developed-photoresist wafer, the AGS reactive ion etcher, CrC-150 chrome sputtering system, and the Denton Desk V sputtering system were used to clean and sputter chromium and gold. The target metal deposition consists of three layers: a 125 Å thick base chromium layer to facilitate

adhesion of the electrode to glass, a 180 nm thick gold layer as the main conductor in the electrode, and a 42 Å thick layer of chromium that will oxidize to an inert finish (figure 3.8).

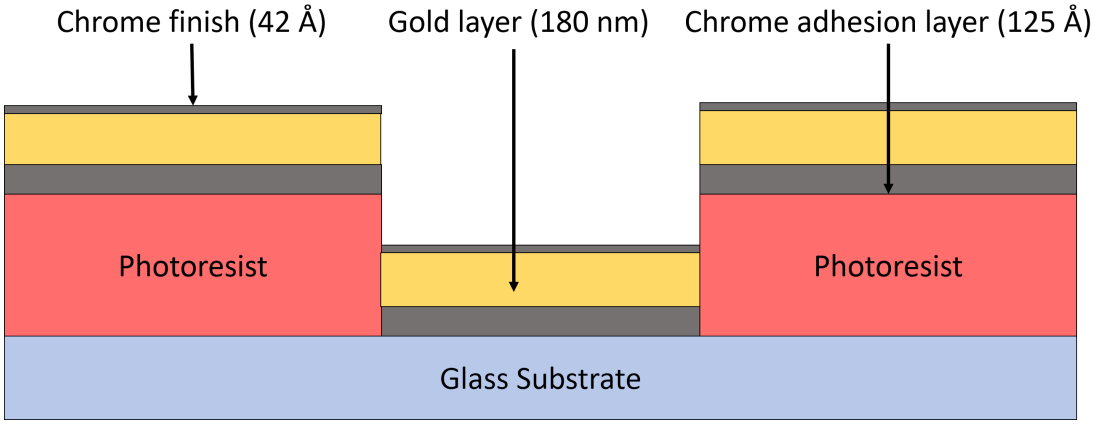

Figure 3.8: Diagram of the three layered metal deposition onto photoresist-developed substrate.

To prepare the photoresist-developed wafer for metal deposition, the wafers were exposed to an oxygen plasma to volatilize and remove organic residues. The wafer was placed under vacuum in the AGS RIE system and exposed to an oxygen plasma for 30 seconds (figure 3.10). The CrC-150 sputtering system was then used to deposit 125 Å of chromium at a rate of 250 Å per minute for 30 seconds. Using the Denton Desk 5, 180 nm of gold was deposited at a rate of 180 Å per minute for 10 minutes. A final 42 Å layer of chromium was deposited with the CrC-150 at a rate of 250 Å per minute for 10 seconds (figure 3.9).

(a) CCr-150 Sputter system

(b) Denton Desk V Sputter/Etch unit

Figure 3.9: The sputter machines used for metal deposition. The CCr-150 and the Denton Desk V were used for chromium and gold deposition respectively.

Figure 3.10: The AGS reactive ion etcher used to remove organic residue with an oxygen plasma.

During the transition between sputtering systems, the wafers were kept under vacuum in order to keep them clean, and in the case for chromium depositions, to reduce the formation of chromium oxide which can significantly impair chromium-gold adhesion.

Lift Off

The final step of the electrode fabrication process was to remove the photoresist with the undesired metal depositions. The wafers were submerged in Microposit remover 1165 for five days under constant agitation (figure 3.11a). To increase the speed of lift off, the solution can be heated to 65°C.

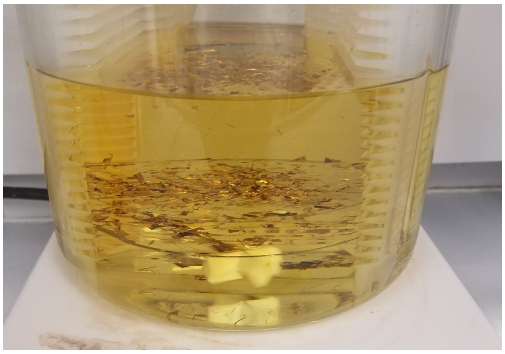

(a) Sputtered wafer in Microposit remover

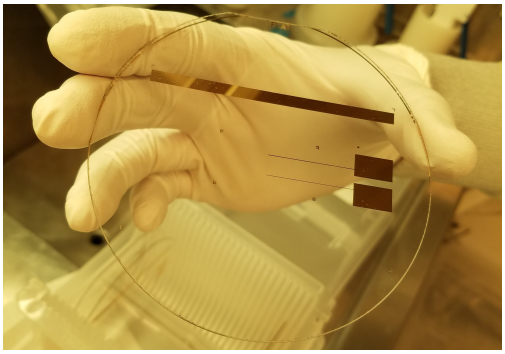

(b) Wafer with electrode post lift off

Figure 3.11: (a) Metal depositions removed from the glass substrate with Microposit remover 1165. (b)The remaining depositions after the lift off process.

3.1.3 Device Assembly: Alignment and Plasma Bonding

To assemble the PDMS chip the electrodes, the components were plasma bonded to create a water-tight seal that permits optical viewing. The PDMS and the glass electrode substrate were placed device-side up in the Cal Poly Microfabrication Lab's PDC-32G plasma cleaner. After pumping the plasma cleaner down to a vacuum, the device was exposed to an atmospheric plasma for 10 seconds.

Figure 3.12: PDC-32G plasma cleaner used for plasma bonding.

After plasma activation, a drop of ethanol was placed on the PDMS surface before placing the PDMS onto the electrode substrate. This created a liquid float barrier that prevented permanent binding for $\sim$5 minutes. The electrodes and PDMS microchannels were aligned by hand with a microscope set at 20X magnification for

visual feedback. After proper alignment, the device was baked in an oven at 65°C for an hour.

3.2 Software Interface

LabVIEW was used to interface with the NI-5421 function generator and the NI-5124 oscilloscope to package the circuit model, data acquisition, and data analysis into an impedance spectroscope program. The LabVIEW language was chosen due to the ease of connecting to the National Instrument hardware and the rapid development cycle. The program specifications include interfacing with the NI-hardware to run an impedance spectroscopy experiment, the ability to control the sweeping frequencies, the ability to switch circuit topologies, the ability to automatically run tests at specified intervals, the implementation of a data saving system that records the users settings for the experiment as well as the impedance spectroscopy results, and the ability to view and compare data.

3.2.1 Architecture

The LabVIEW program was designed with an event-driven state machine architecture and is diagrammed in figure 3.13. A state machine is a common LabVIEW coding pattern where the program exists as a set of states. Depending on user input or calculations, each state leads to a subsequent state that can potentially lead to a large network of modular decision making code. For this program, the state machine is simple with most states leading to an idle state that continues to wait for user input. The state machine lives inside an event structure that listens for specific user interface (UI) interactions. These interactions trigger an event that runs code and can specify the next state in the machine. After a specified amount of time passes without an event triggering, the time out event will trigger and run the state machine.

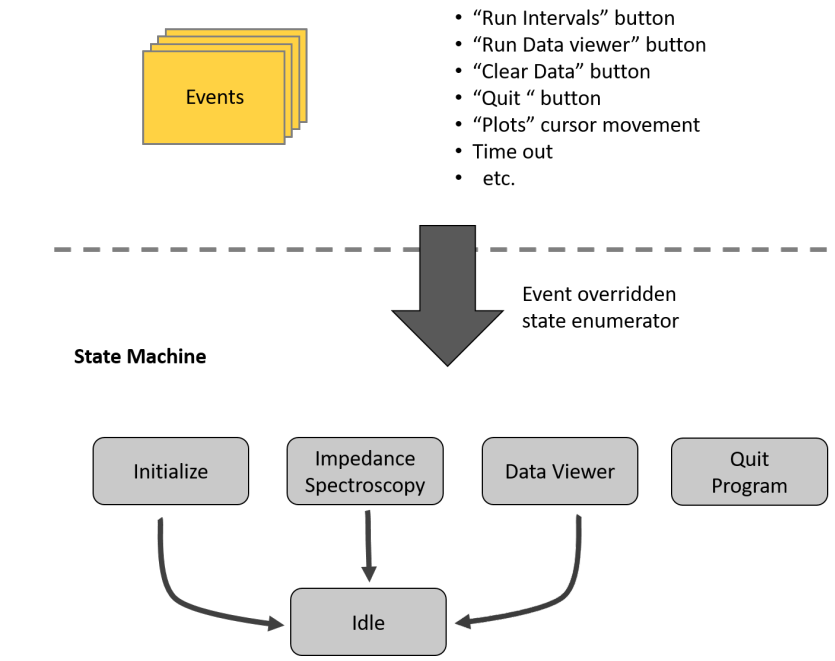

(a) Event-driven state machine architecture

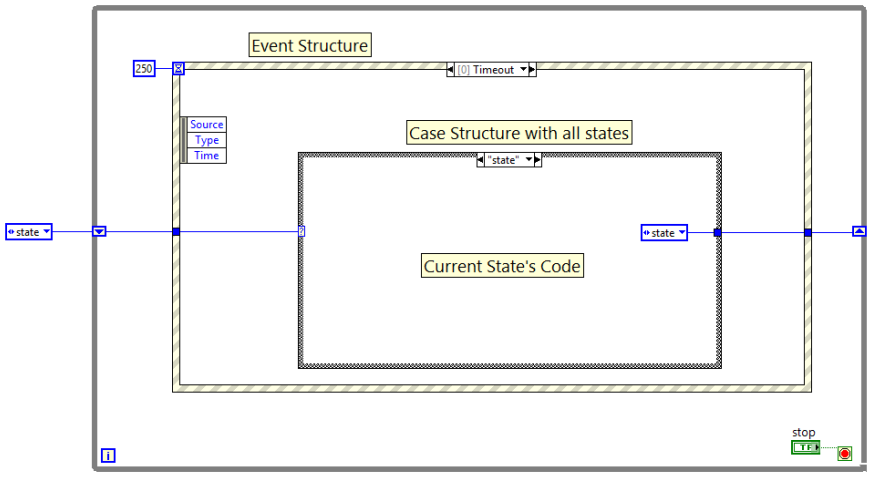

(b) Event-driven state machine code

Figure 3.13: The event-driven state machine architecture used for the impedance spectroscope LabVIEW program.

The event driven state machine architecture allowed for a responsive UI that maintained the modularity of a state machine with safe program initialization and exit. The architecture was implemented to create two main modules: the impedance spectroscope, and the data viewer.

3.2.2 Impedance Spectroscopy

The impedance spectroscopy UI gives users the ability to control settings for experiments and view results (figure 3.14). All impedance spectroscopy settings are located in a set of three tabs: circuit topology, frequency parameters, and interval parameters.

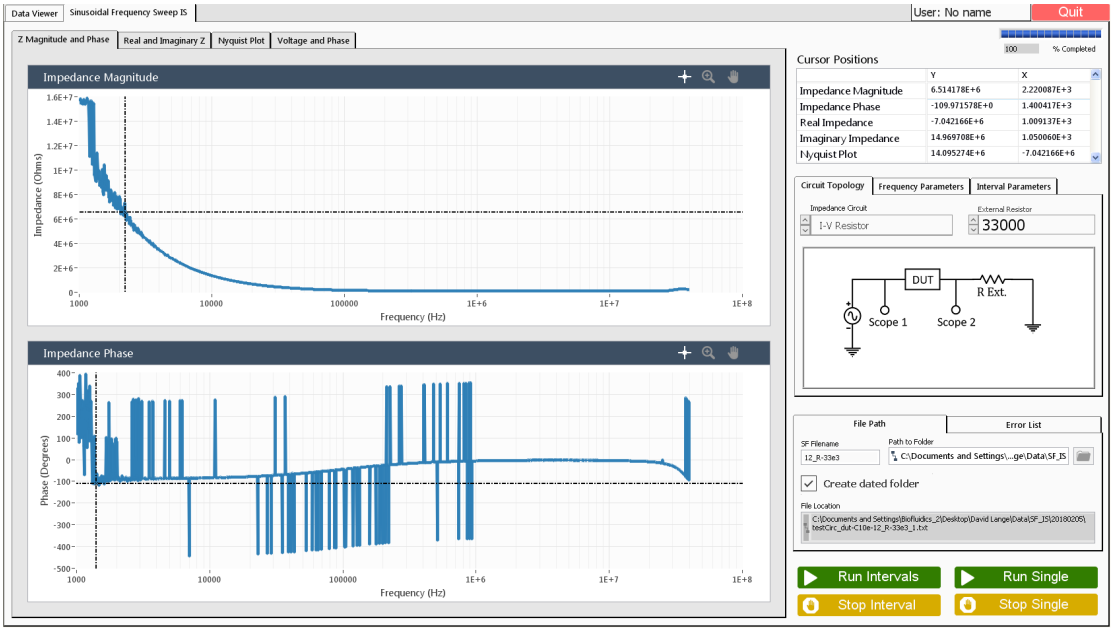

Figure 3.14: Impedance spectroscopy user interface

The circuit topology tab informs the software of the circuit being used and the value of the external resistor (figure 3.15). With each circuit selection, an image updates to display the measurement method and the required oscilloscope connections. In the current implementation, the software includes options for the I-V and auto-balancing bridge circuits.

The frequency parameter tab controls the frequencies studied in the impedance spectroscopy experiment (figure 3.16). The frequency expression shows how frequency values are calculated with x and y representing incremented values with the caveat that a value for every increment of x is generated for every one increment of y. For example, with the settings given in figure 3.16, ten frequencies per decade with decades 1E3 to 1E7 are generated. The max input frequency truncates the frequencies generated to the specified value. In addition to frequency parameters,

the tab also includes controls for the waveform amplitude, the number of cycles measured by the oscilloscope, and the sample rate.

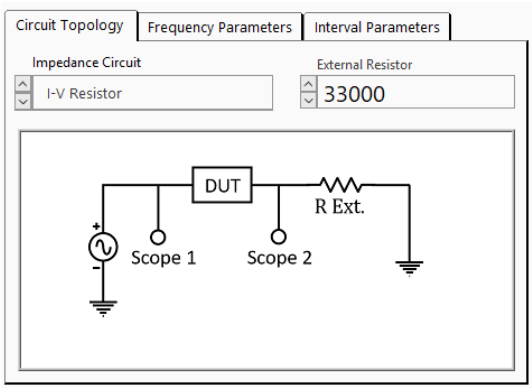

(a) I-V topology

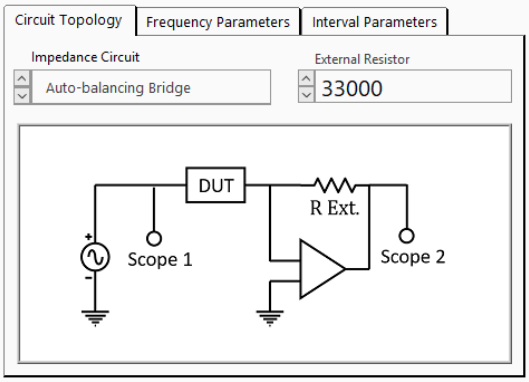

(b) Auto-balancing bridge topology

Figure 3.15: Circuit settings

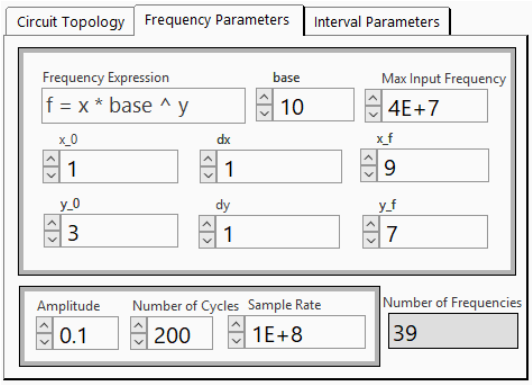

Figure 3.16: Frequency sweep options

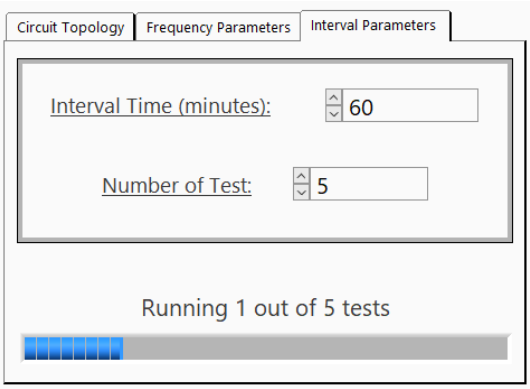

Figure 3.17: Interval measurement settings

The interval parameters tab contains options for running automatic experiments at timed intervals (figure 3.17).

After running an experiment, the results are visualized and saved in a text file. The results are used to generate seven plots in four different tabs: impedance magnitude and phase, real and imaginary impedance, the Nyquist plot, and voltage bode and phase plots (figure 3.18). With the exception of the voltage bode and phase plots, the graphs are different ways of visualizing the impedance data. The voltage bode and phase plots were primarily used in troubleshooting.

Every experiment is automatically saved in a tab delimited text file with the designated experiment name (a number is appended to a filename duplicate; i.e. no

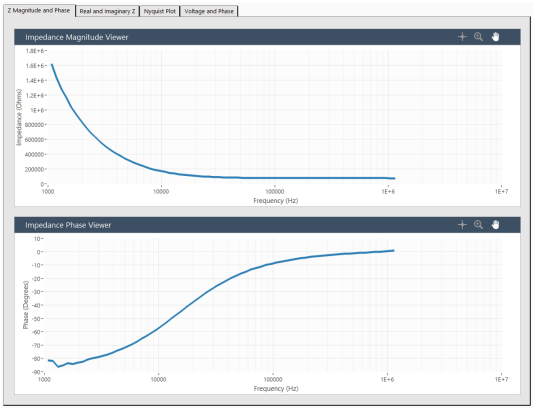

(a) Impedance magnitude and phase

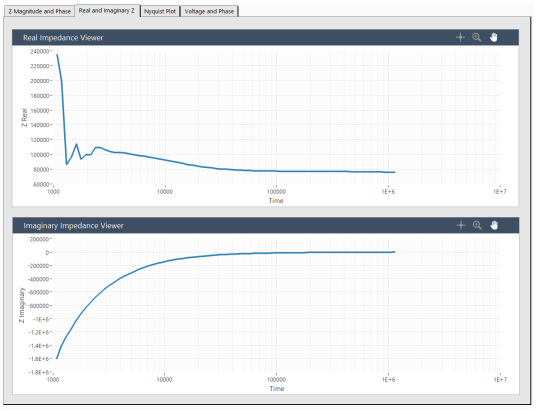

(b) Real and imaginary impedance graphs

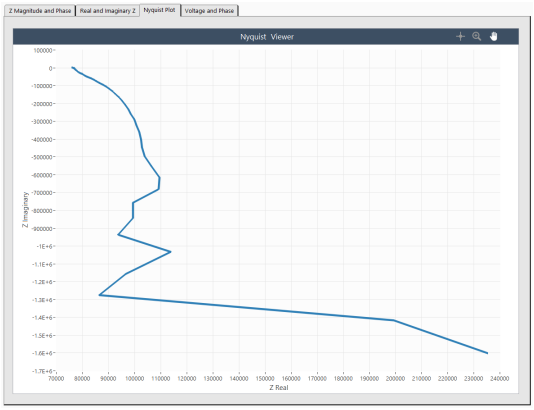

(c) Nyquist plot

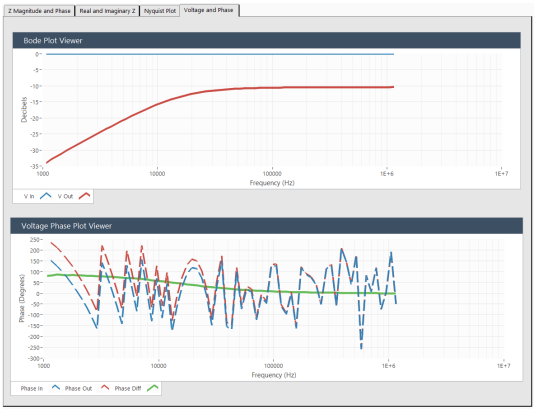

(d) Bode pot and phase shift plot

Figure 3.18: Software generated graphs to display the results of the impedance spectroscopy experiment. Sub-figures (a), (b), and (c) present different views of the calculated impedance data while sub-figure (d) is reserved for troubleshooting.

files are overwritten) with the option to generate dated folders. Each file contains a header that saves the date and time the experiment was run, the user, and user defined settings. The impedance spectroscope data is saved in labeled columns. An example of a saved experiment file is given in figure 3.19.

Experiment: test.txt
Date: 02/01/2018
Time: 12:32:45 PM
User: dplange
Circuit Topology: I-V Resistor
Amplitude: 0.1
Number of waveform cycles: 200
External resistor: 33000
Sample rate: 100000000
Frequency expression: f = (1:1:1)*2.71^(7:0.1:14)
Max frequency: 40000000
END OF HEADER

frequency	zMag	zPhase	zReal	zImag	vMagIn	vMagOut	vPhaseIn	vPhaseOut
1073.62	1585109	-84.101	162919	-2E+06	0.09992	0.00204	166.549	250.649
1185.97	1428565	-83.706	156625	-1E+06	0.09994	0.00226	146.345	230.051

Figure 3.19: An example of the impedance spectroscopy data file. All user and experiment data is recorded in a TSV file.

3.2.3 Data Viewer

The data viewer UI allows users to visualize and compare previous experiments (figure 3.20). The UI allows up to ten experiments to be simultaneously plotted with a legend in the top right corner and a table to display each experiment's header information.

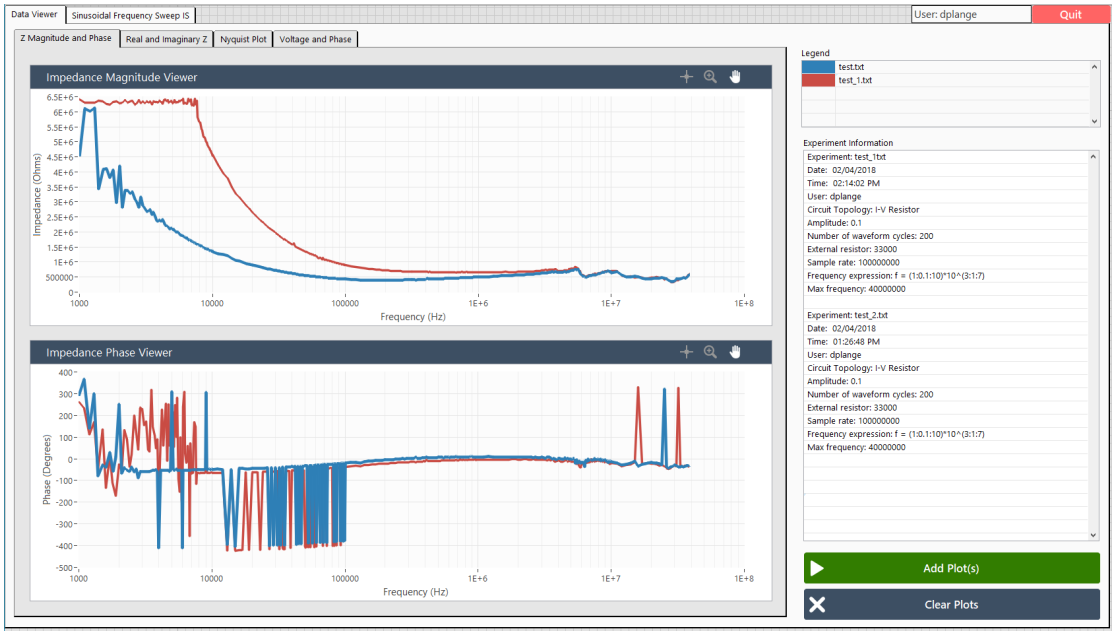

Figure 3.20: The data viewer UI allows users to compare up to 10 experiments simultaneously.

3.3 System Implementation

To run impedance spectroscopy tests, a system was assembled to control and record experiments. The complete implementation included a function generator (NI PXI-5421), an oscilloscope (NI PXI-5124), a hardware interfacing labview program, an I-V circuit, three Harvard apparatus syringe pumps, an inverted video microscope (LabSmith SVM340) for imaging, and the impedance spectroscopy microfluidic chip. Figure 3.21 displays the impedance spectroscopy system.

Figure 3.21: The impedance spectroscopy system.

3.3.1 Electrical Interface

NI Hardware

The NI PXI-5421 function generator and the NI PXI-5124 oscilloscope were used to load and measure the impedance spectroscopy chip. The NI PXI-5421 is a 43 MHz waveform generator capable of generating user defined standard and arbitrary waveforms with a $\pm$6 V range and a 50 Ω output impedance. The signal generator

was controlled with the LabVIEW program and operated to run at specified frequencies of a standard sine wave. The NI PXI-5124 is a 150 MHz 200 MS/s oscilloscope. The PXI-5124 has a 4.0 GS/s equivalent time sampling rate for repetitive signals, and a selectable 50 Ω or 1 MΩ||29 pF input impedance. The oscilliscope was controlled with LabVIEW and configured to have a 1 MΩ||29 pF input impedance.

Electrode Interface

To establish an electrical connection to the impedance spectroscopy chip, solid core wires were soldered to to the device. Since the metal depositions were too thin for direct soldering, copper tape was placed adjacent to the electrode pads, soldered to the solid-core wire, and then a silver-based epoxy was applied to the copper tape and electrode pads using the M6 Chemicals silver conductive pen (figure 3.22). The epoxy has a resistivity of 1E-4 Ω·cm.

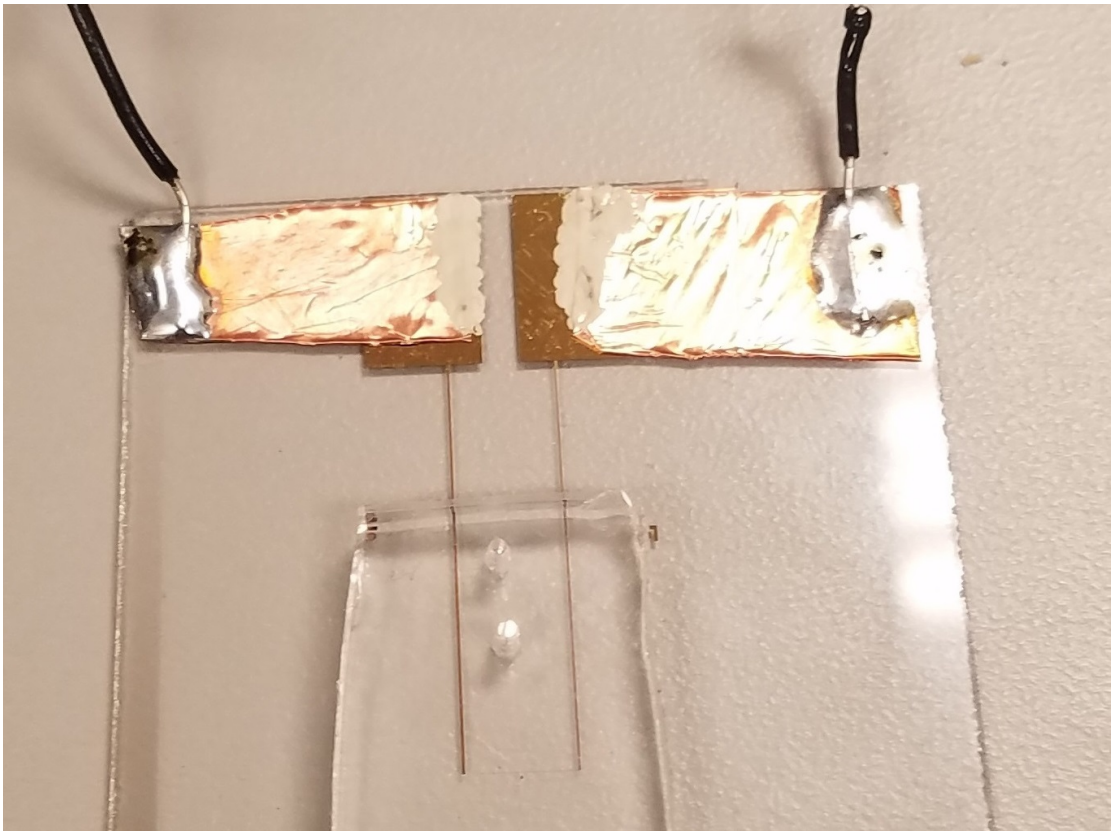

Figure 3.22: The electrode interface consisting of solid-core wire soldered to copper tape epoxied to the electrode pads.

Connections to the NI instruments were made with solid-core wires soldered to BNC female jacks. Since the function generator output signal was not 50 Ω terminated, the signal amplitude will be twice the selected amplitude. Wiring length to the I-V circuit was minimized.

I-V Circuit

An I-V circuit, with an external resistor of 3300 Ω, measured the impedance of the device under testing. The circuit was discussed in detail in section 2.2.3, and the implementation is depicted in figure 3.23.

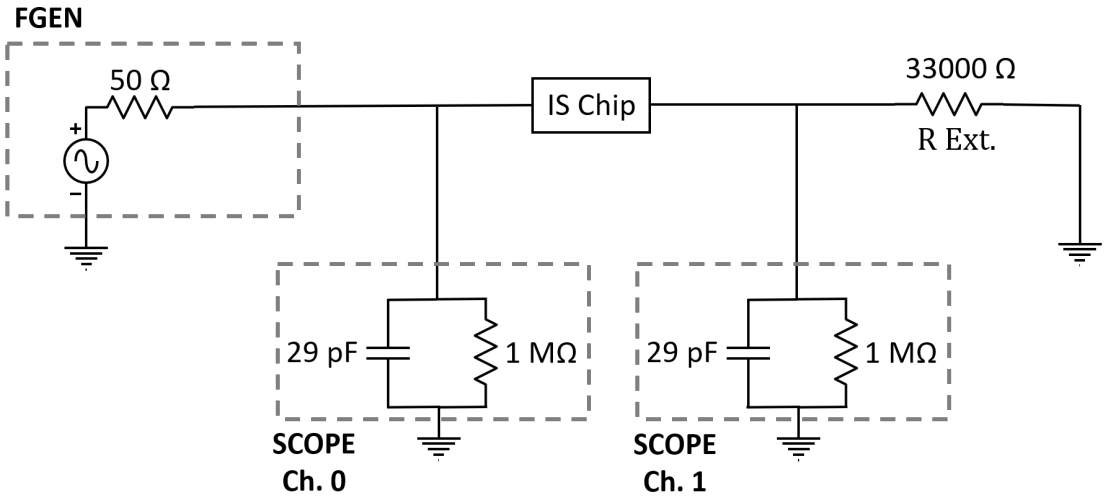

Figure 3.23: Implementation of the I-V circuit including impedance loads of the function generator and oscilloscopes.

The circuit was implemented using two different methods: a system of soldered solid core wires, and using a breadboard. There was no difference noted between the two implementations sweeping up to 40 MHz. However, the breadboard should generally be avoided for high frequencies due to intercontact capacitance ($\sim$25 pF for power strips, and $\sim$2.5 pF for the remaining breadboard).

3.3.2 Microfluidics

Three Harvard Apparatus syringe pumps driving 1 mL BD syringes were used to control fluid flow through the impedance spectroscope chip. The microfluidic net-

work is diagrammed in figure 3.24.

The original design of the device was meant to capture a single cell in the measurement chamber, but since this design cannot achieve single-cell isolation (section 1), pump #3 was used to initially flood the flush channels and then hold its syringe at a constant volume to prevent flow through the flush channels. For fluid flow, pump #1 drove fluid at 1 μL/min and pump #2 pulled fluid at 1 μL/min.

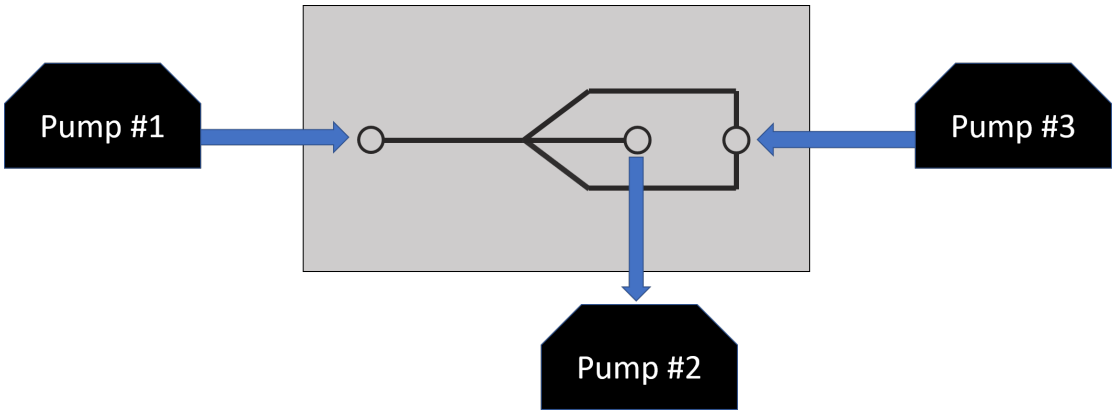

Figure 3.24: The implemented microfluidic network utilzed 3 Harvard Apparatus syringe pumps. Pump #1 drove fluid into the device and pump #2 suctioned particles into the sensor region.

Spherotech polystyrene beads (FP-2052-2) were injected into the impedance spectroscope system for system evaluation. The Spherotech beads ranged from 7 μm to 7.9 μm in diameter and had a relative permittivity of 2.5 (table 2.1). The beads were mixed with a separate DI water and phosphate bufferred saline solution (PBS) at 0.1% by mass. A single drop of Titron x-100 surfactant was added to both solutions and then sonicated.

The device was evaluated by making impedance measurements of DI water, PBS, polystyrene micro-beads.

Chapter 4: Modeling

In order to understand, validate, and optimize the single cell impedance spectroscopy system, three models were implemented: an analytic impedance solution, finite element analysis simulations, and a circuit model. The analytic impedance solution was implemented to build a foundational understanding of basic IS systems, to optimize simple IS systems, and to validate FEA simulations. The finite element analysis expands upon the analytic solution to understand how the complex device geometry differentiates from the simple analytic impedance model geometry, and to inform optimized device designs. The circuit model was developed to validate the IS DAQ system and understand its shortcomings.

4.1 Analytic Single Cell Impedance Model

For cell suspensions with low volume fractions, Maxwell's Mixture theory can model the electrical impedance of the system. The model is summarized in equations 4.1 to 4.5 below.

$$\tilde{Z}_{mix} = \frac{1}{jw\tilde{C}}, \tag{4.1}$$

$$\tilde{C} = \tilde{\epsilon}_{mix} G_f, \tag{4.2}$$

$$\tilde{\epsilon}_{mix} = \tilde{\epsilon}_m \frac{1 + 2\phi\tilde{f}_{cm}}{1 - \phi\tilde{f}_{cm}}, \tag{4.3}$$

$$\tilde{f}_{cm} = \frac{\tilde{\epsilon}_p - \tilde{\epsilon}_m}{\tilde{\epsilon}_p + 2\tilde{\epsilon}_m}, \tag{4.4}$$

$$\tilde{\epsilon}_p = \tilde{\epsilon}_{mem} \frac{\gamma^3 + 2(\frac{\tilde{\epsilon}_i - \tilde{\epsilon}_{mem}}{\tilde{\epsilon}_i + 2\tilde{\epsilon}_{mem}})}{\gamma^3 - (\frac{\tilde{\epsilon}_i - \tilde{\epsilon}_{mem}}{\tilde{\epsilon}_i + 2\tilde{\epsilon}_{mem}})} \text{ with } \gamma = \frac{R + d}{R}. \tag{4.5}$$

An explanation of these equations is given in section 2.3.1. The values for G_f (geometric constant) and ϕ (volume fraction) are dependent on the geometry of the system. In the following sections, solutions to both variables will be presented for the co-planar electrode configuration in figure 4.1.

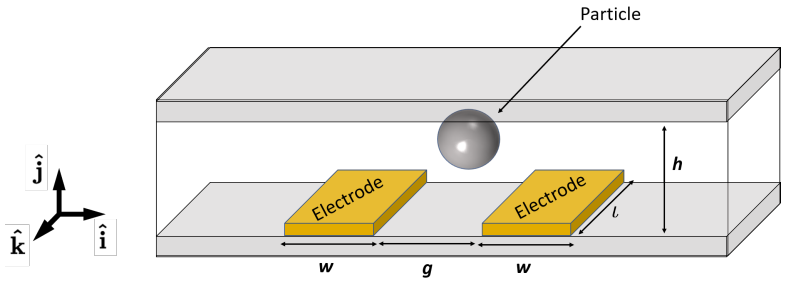

Figure 4.1: Diagram of a simplified impedance sensor chamber where w, g, and l are the width, gap, and length of the electrodes respectively. h is the height of the chamber.

4.1.1 Coplanar Electrode Cell Constant

The geometric constant is the inverse of the cell constant (κ). If the cell constant is thought of in terms of the resistive cell constant ($R = \kappa\rho$), then the geometric cell constant can be thought of as the capacitive cell constant ($C = G_f\epsilon$). If equations 4.1 to 4.5 were expressed in terms of complex conductivities rather than complex permittivities, the impedance of the mixture could be expressed as $\tilde{Z}_{mix} = \frac{\kappa}{\tilde{\sigma}}$. For the ideal parallel plate capacitor in figure 4.2, where the electric field is uniform, the geometric constant can be expressed as

$$G_f = (\kappa)^{-1} = \frac{\gamma l}{d}, \tag{4.6}$$

where d is the distance between the electrodes, γ is the height of the electrodes, and l is the length of the electrodes. This relation is discussed in further detail in section 2.3.2. If the co-planar electrode geometry is mapped to the ideal parallel plate capacitor configuration, the ratio of d and γ can be derived.

Sun, Greene, et al. utilized the Schwartz-Christoffel transform to map the coplanar electrode configuration in figure 4.1 to the configuration of parallel electrodes with uniform electrode fields in figure 4.2 [31]. The Schwartz-Christoffel formula is a powerful transform that allows the mapping of the upper complex T-plane ($y > 0$) to the inside of a polygon and can be expressed as

$$Z = C_1 \int_{T_0}^{T} \prod_{r=1}^{m} (T - T_r)^{(\theta_r/\pi - 1)} dT + C_2, \tag{4.7}$$

where Z is the interior of a polygon in the Z-plane with vertices $Z_1,\ Z_2,\ Z_3,\ ..., Z_m$ and angles $\theta_1,\ \theta_2,\ \theta_3,\ ..., \theta_m$ which correspond to the points $T_1,\ T_2,\ T_3,\ ..., T_m$ on the real axis of the T-plane. C_1 and C_2 are integration constants. The Schwartz-Christoffel transform has three degrees of freedom, and consequently, up to three points may be chosen arbitrarily. T_0 is the reference and is typically chosen at the origin.

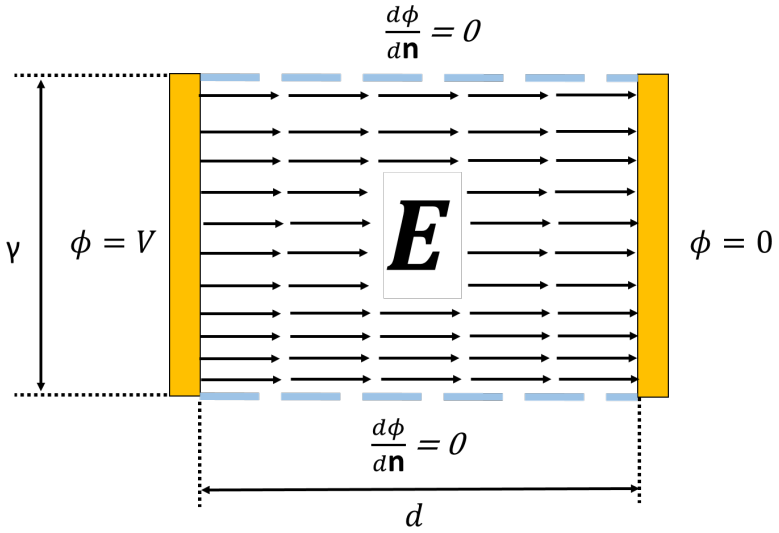

Figure 4.2: Uniform electric field between two parallel electrodes where $\boldsymbol{E}$ is the electric field, ϕ is the voltage, and $\frac{d\phi}{d\boldsymbol{n}} = 0$ is the boundary condition of a perfect insulator. The dimensions of the capacitor are the electrode height γ, and the distance between the electrodes d.

A brief solution for the co-planar electrode system is covered in the following section with the complete step-by-step solution included in appendix B.3.

To find the geometric constant for coplanar electrodes, Schwartz-Christoffel transforms will be used to map half of the co-planar electrode geometry (Z-plane) to the upper complex plane (T-plane) and then to map the T-plane to half of the ideal parallel plate geometry (W-plane). The W-plane vastly simplifies the solution to the cell constant and will allow the direct calculation of the ratio γ to d. Figure 4.3 diagrams the three mapped planes.

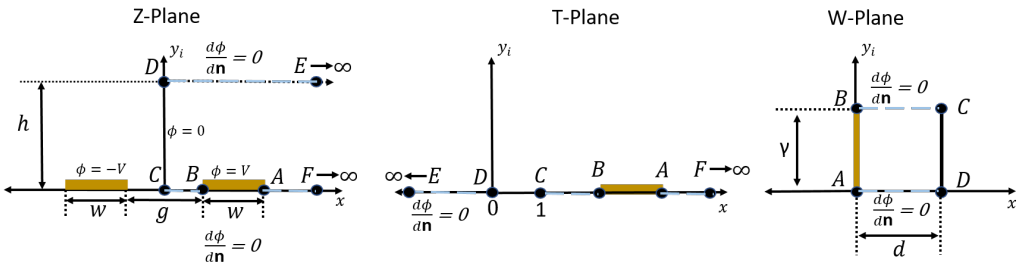

Figure 4.3: Diagrams of coplanar electrodes through Schwartz-Christoffel mapping where the Z-plane contains the physical dimensions of the electrode configuration, the T-Plane links the Schwartz-Christoffel mappings of Z and W plane, and the W-plane represents the parallel electrodes producing a uniform electrode field.

In this model, it will be assumed that the floor and the ceiling of the model are perfect insulators, the medium is homogeneous, and the channel is infinitely long.

Schwartz-Christoffel Transform Mapping

Mapping the T-plane to the Z-plane, point C and D from figure 4.3 will be chosen as the polygon corners with angles of $\pi/2$.

$$Z = C_1 \int (T - T_c)^{-1/2}(T - T_D)^{-1/2} dT + C_2, \tag{4.8}$$

By integrating equation 4.8 with the coordinate relationships $Z_C = 0$, $T_C = 1$ and $Z_D = jh$, $T_D = 0$, the mapping between the Z-plane and the T-plane can be expressed as

$$Z = \frac{2h}{\pi} \ln\left(\sqrt{T-1} + \sqrt{T}\right), \tag{4.9}$$

The mapping of the T-plane to the Z-plane is depicted in figure 4.4.

The mapping of the Z-plane to the T-plane can be found by solving for the inverse of equation 4.9:

$$T = \cosh^2\left(\frac{Z\pi}{2h}\right). \tag{4.10}$$

Figure 4.5 depicts the mapping of the Z-plane to the T-plane.

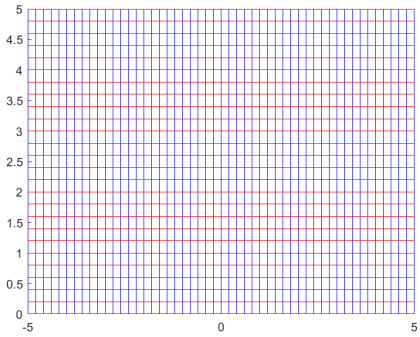

(a) Part of upper complex T-Plane

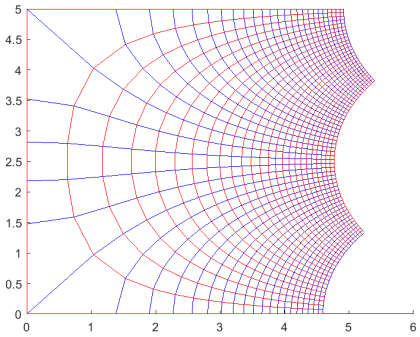

(b) Mapping of the part of the T-plane to the polygon in the Z-plane

Figure 4.4: Mapping of the T-plane to the inside of the open polygon in the Z-Plane outlined by the points F, C, D, and E in the Z-plane. Equation 4.9 is the mapping function.

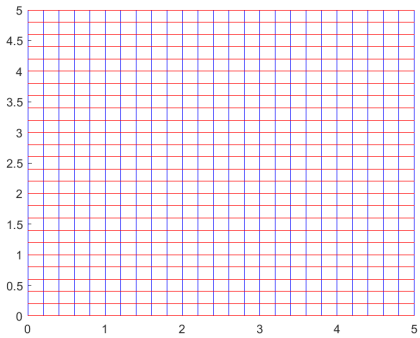

(a) Part of the open polygon in the Z-plane.

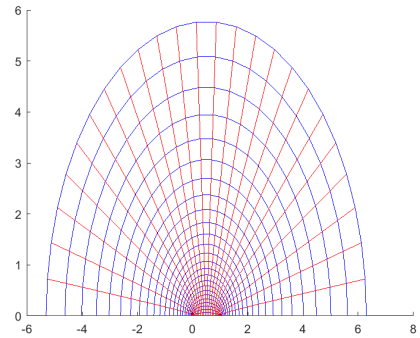

(b) Mapping of part of the polygon in the Z-plane to the T-plane.

Figure 4.5: Mapping of the open polygon in the Z-Plane outlined by the points F, C, D, and E. Equation 4.10 is the mapping function.

To map the T-plane to the W-Plane, points A, B, C, and D, will be chosen as the polygon corners with angles of $\pi/2$:

$$W = D_1 \int (T - T_A)^{-1/2}(T - T_B)^{-1/2}(T - T_C)^{-1/2}(T - T_D)^{-1/2}\, dT + D_2. \quad (4.11)$$

Since equation 4.11 is an integral of a rational function with a root of a quartic polynomial, the function can be rewritten as an elliptic integral [50]. For $T > T_A > T_B > T_C > T_D$,

$$W = D_3 F(v, k) + D_2, \quad (4.12)$$

$$D_3 = \frac{2D_1}{\sqrt{(T_A - T_C)(T_B - T_D)}}, \tag{4.13}$$

$$v = \arcsin\sqrt{\frac{(T_B - T_D)(T - T_A)}{(T_A - T_D)(T - T_B)}}, \tag{4.14}$$

$$k = \sqrt{\frac{(T_B - T_C)(T_A - T_D)}{(T_A - T_C)(T_B - T_D)}}, \tag{4.15}$$

where $F(v,k)$ is the incomplete elliptic integral of the first kind, and can be expressed as

$$F(v,k) = \int_0^v \frac{d\alpha}{\sqrt{1 - k^2\sin^2\alpha}}, \tag{4.16}$$

where v and k are referred to as the amplitude and modulus respectively. For all values that T are greater than T_A or do not lay on the real number line (i.e. has an imaginary component), the elliptic integral provided is valid.

Using the coordinate relations for point A: $W_A = 0$, $F\big(v(T_A), k\big) = 0$; point B: $W_B = j\gamma$, $F\big(v(T_B + \lim_{x\to 0} jx), k\big) = jK(k')$; and point D: $W_D = \delta$, $F\big(v(T_D), k\big) = K(k)$; we find that

$$D_2 = 0, \tag{4.17}$$

$$D_3 = \frac{\delta}{K(k)}, \tag{4.18}$$

and

$$D_3 = \frac{j\gamma}{K(k')}, \tag{4.19}$$

where $K(k)$ is the complete elliptic integral and is expressed as

$$K(k) = \int_0^{\pi/2} \frac{d\alpha}{1 - k^2\sin^2(\alpha)}, \tag{4.20}$$

and where k' is the complement modulus and is expressed as

$$k' = \sqrt{1 - k^2}, \tag{4.21}$$

By combining equations 4.18 and 4.19 we get

$$\frac{\gamma}{\delta} = \frac{K(k')}{K(k)}, \tag{4.22}$$

and then substituting equation 4.22 into equation 4.6, and recognizing that δ in the W-plane only represents half of the actual parallel plate distance (d), we find that the cell constant and geometric factor for co-planar electrodes are

$$\kappa = \frac{2K(k)}{lK(k')}, \tag{4.23}$$

$$G_f = \frac{lK(k')}{2K(k)}. \tag{4.24}$$

It should be noted that the current mapping of the T-plane to W-plane is unconstrained with no solution to the constant D_3. By selecting a value for either D_3, γ, or δ, we constrain the mapping, but the actual value we choose is of no consequence to the power, current, or impedance of the system. Physically, this is explained since the cell constant is defined by the ratio of d and γ and, given the same material properties, as long the ratio in equation 4.22 is maintained, the effective impedance will be the same. There are an infinite number of W-planes that satisfy the ratio in equation 4.22. For mapping the T-plane to the W-plane, D_3 can be arbitrarily chosen. If D_3 is chosen to be 1, the W transform can be expressed as

$$W = F(v, k). \tag{4.25}$$

Figure 4.6 depicts the mapping the Z-plane to the W-plane.

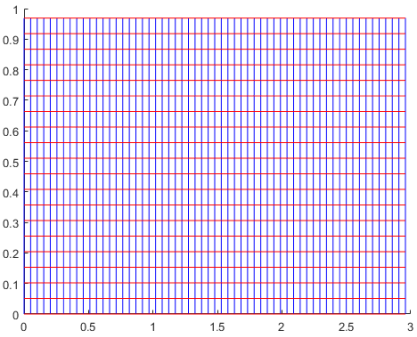

(a) Part of the open polygon in the Z-plane.

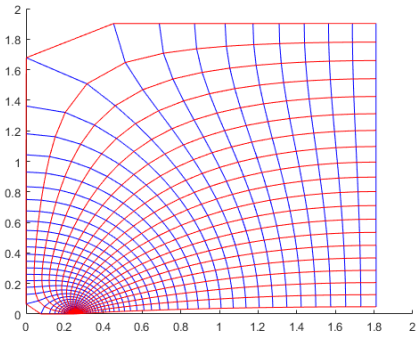

(b) Mapping of part of the polygon in the Z-plane to the W-plane.

Figure 4.6: Mapping of the open polygon in the Z-Plane outlined by the points F, C, D, and E to the W-plane. Equation 4.25 is the mapping function.

4.1.2 Coplanar Electric Field

With Z-T and T-W mappings, the solution of the electric field in the W-plane can be mapped to the Z-plane. The mapping of the electric field can be expressed as

$$\boldsymbol{E_z} = -\nabla\phi_z \quad \text{with} \quad \nabla\phi_z = \nabla\phi_w \overline{\frac{dW}{dZ}}. \tag{4.26}$$

Where $\nabla\phi$ is the gradient of potential and $\overline{\frac{dW}{dZ}}$ is the conjugate of the derivative of W with respect to Z [51].

Applying the chain rule to equation 4.26, the electric field mapping is expressed as

$$\boldsymbol{E_z} = -\nabla\phi_w \overline{\frac{dW}{dT}\frac{dT}{dZ}}, \tag{4.27}$$

with

$$-\nabla\phi_w = \frac{V}{d}, \tag{4.28}$$

$$\frac{dW}{dT} = \frac{d}{2K(k)} \frac{(T_A - T_C)^{1/2}(T_B - T_D)^{1/2}}{(T - T_A)^{1/2}(T - T_B)^{1/2}(T - T_C)^{1/2}(T - T_D)^{1/2}}, \tag{4.29}$$

and

$$\frac{dT}{dZ} = \frac{\pi}{h}(\sqrt{T - T_D})(\sqrt{T - T_C}). \tag{4.30}$$

Combining equations, 4.27, 4.28, 4.29, and 4.30, the electric field for co-planar

electrodes can be expressed as equation 4.31. The electric field solution is depicted with streamlines in figure 4.7a and with electric field magnitude in figure 4.7b. A complete step-by-step solution is provided in appendix B.4.

$$E_z = \frac{\pi V}{2hK(k)} \frac{\sqrt{(T_A - T_C)(T_B - T_D)}}{\sqrt{(T - T_A)(T - T_B)}} \tag{4.31}$$

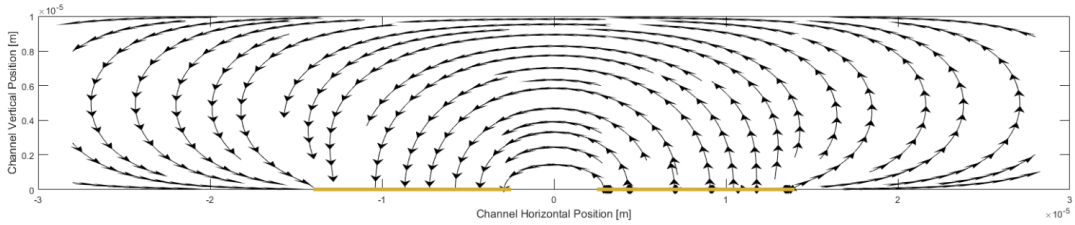

(a) Electric field stream lines for co-planar electrodes.

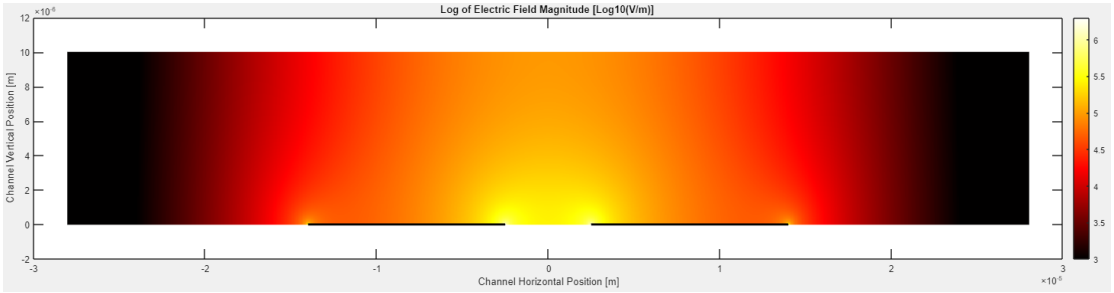

(b) Electric field magnitude generated by co-planar electrodes. The magnitude is reported in units Log_{10}(V/m).

Figure 4.7: The electric field for co-planar electrodes as defined by equation 4.31. The electrodes are 11.5 μm wide with a 5 μm gap and the chamber is 10 μm tall.

4.1.3 Novel Volume Fraction

The traditional method to approximate the volume fraction of a single spherical particle suspended over co-planar electrodes is to calculate the ratio of the cell volume to the volume over the electrodes in the channel:

$$\phi = \frac{\frac{4}{3}\pi R^3}{(2w+g)hl}, \tag{4.32}$$

where R is the particle radius, w is the electrode width, g is the gap between the coplanar electrodes, h is the height of the channel, and l is the length of the electrodes in the channel. This approximation assumes that the fringe fields outside the boundaries of the electrodes is negligible, and that the electric field magnitude is uniform inside the boundaries of the electrodes. However, for most co-planar electrode geometries used in impedance spectroscopy, the electric field is highly non-uniform. Figure 4.7 depicts the non-uniformity of an electric field produced by co-planar electrodes. In this section, two alternative approaches to calculating the correct volume fraction are proposed.

Mapping Particle Volume to the W-Plane

To calculate the effective volume fraction, it is necessary to calculate the ratio of effective volumes:

$$\phi' = \frac{V_p'}{V_{sys}'}, \tag{4.33}$$

where ϕ' and V_p' and V_{sys}' denotes the effective volume fraction, effective volume of the particle, and effective volume of the system respectively. When considering a particle suspended in the Z-plane, it is difficult to determine the effective volume for the system or the particle due to the non-uniform electric field. However, the electric field is uniform when the system is mapped to the W-plane. The effective volume fraction can be expressed as

$$\phi' = \frac{V_p^w}{V_{sys}^w}, \tag{4.34}$$

where w denotes volumes in the W-plane.

By referring to the ideal capacitor geometry in figure 4.2, the system volume in the W-plane can be expressed as

$$V_{sys}^{w} = \gamma dl, \tag{4.35}$$

and by substituting in equations 4.18 and 4.19, and remembering D_3 was arbitrarily chosen as 1 for the W-mapping, we find

$$V_{sys}^{w} = 2K(k)K(k')l. \tag{4.36}$$

When a spherical particle is mapped to the W-plane, the particle cross-sections are deformed based on the non-uniformity of the electric field. If we assume that these cross-sections are deformed to either "circle-like" or "ellipsoid-like" sections, the mapped volume of the sphere can be approximated as

$$V_{p}^{w} = \frac{4}{3}\pi r_z r_{w1} r_{w2}, \tag{4.37}$$

where r_z is the radius of the spherical particle in the Z-plane, and r_{w1} and r_{w2} are the principle radii of the "ellipsoid-like" mapping of the particle orthodrome to the W-plane. Equation 4.37 can be rewritten as

$$V_{p}^{w} = \frac{4}{3} r_z \iint_{A_w} dA, \tag{4.38}$$

where the integral represents the area of the particle orthodrome mapped to the W-plane.

Combining equations equations 4.36 and 4.38, we can approximate the effective volume fraction as

$$\phi_w = \frac{2}{3}\frac{r_z \iint_{A_w} dA}{K(k)K(k')l}. \tag{4.39}$$

The major shortcoming of this method is operating under the assumption that

the mapped particle cross-sections are circle or ellipsoid-like. From simulated data, many particle-electrode configurations result in mapped particle cross-sections that do appear circular or ellipse-like, but there will be an associated error that will often grow with the degree of the non-uniformity. Compared to the traditional volume fraction, the error is minimal. The W-plane volume fraction accounts for fringe field effects and the local non-uniformity of the electric field, allowing for the calculation of the volume fraction for a particle located anywhere in the system.

Power Volume Fraction

In the W-plane, which represents the ideal parallel plate electrode model depicted in figure 4.2, the electric field is uniform inside the valid domain, and as a direct result, the power density is uniform throughout the domain of the W-plane. By interpreting the effective volume fraction as the ratio of volumes in the W-plane, we arrive at the following relationship:

$$\phi' = \frac{V'_p}{V'_{sys}} = \frac{V^w_p}{V^w_{sys}} = \frac{P_p}{P_{sys}}. \tag{4.40}$$

By finding the ratio of power in the domain of the particle to the power of the system, we are able to calculate the effective volume fraction as the power fraction:

$$\phi_p = \frac{P_p}{P_{sys}}, \tag{4.41}$$

The power of the system can be expressed as

$$P_{sys} = \frac{(\Delta V)^2}{R_{sys}}, \tag{4.42}$$

where ΔV is $2V$ for our mapped system. By recalling that $R = \rho\kappa$,

$$P_{sys} = \frac{4V^2}{\rho\kappa}. \tag{4.43}$$

By substituting equation 4.23 for the cell constant, the power of the system is ex-

pressed as

$$P_{sys} = \frac{2V^2K(k')l}{\rho K(k)}. \tag{4.44}$$

The power in the domain of a spherical particle can be solved for by integrating the power density over the volume of the particle.

$$P_p = \iiint_V \rho \big|J\big| dV = \iiint_V \frac{1}{\rho}\big|E\big|^2 dV \tag{4.45}$$

By substituting the solution of the electric field from equation 4.31, we can express the power in the domain of the particle as

$$P_p = \frac{1}{\rho}\left(\frac{\pi^2V^2}{4h^2K(k)^2}\right) \iiint_V \left|\left(\frac{T_A - T_C}{T - T_A}\right)\left(\frac{T_B - T_D}{T - T_B}\right)\right| dV. \tag{4.46}$$

Combining equations 4.41, 4.44, and 4.46, the power fraction can be expressed as

$$\phi_p = \frac{\pi^2}{8h^2K(k)K(k')l} \iiint_V \left|\left(\frac{T_A - T_C}{T - T_A}\right)\left(\frac{T_B - T_D}{T - T_B}\right)\right| dV. \tag{4.47}$$

If the particle is a sphere, the integral can be conveniently expressed in spherical coordinates:

$$\phi_p(Z_c, R) = 2C \int_0^{\frac{pi}{2}} \int_0^{2\pi} \int_0^R r^2 \sin(\phi) F(r, \theta, \phi, Z_c) dr\, d\theta\, d\phi, \tag{4.48}$$

where Z_c is the center of the particle on the complex Z-plane, R is the particle radius,

$$F(r, \theta, \phi) = \left|\left(\frac{T_A - T_C}{T(r, \theta, \phi, Z_c) - T_A}\right)\left(\frac{T_B - T_D}{T(r, \theta, \phi, Z_c) - T_B}\right)\right|, \tag{4.49}$$

$$T(r, \theta, \phi, Z_c) = \cosh^2\left(\frac{\pi}{2h}\left(Z_c + r\cos(\frac{\pi}{2} - \phi)e^{i\theta}\right)\right), \tag{4.50}$$

and

$$C = \frac{\pi^2}{8h^2K(k)K(k')l}. \tag{4.51}$$

The power fraction provides an accurate solution to the volume fraction for the

co-planar electrode system outlined in section 4.1.1. These corrected volume fractions allow for a complete analytic impedance solution that accounts for the effect of the fringe field and non-uniform electric field based on the position of the particle. If incorporated in a drag-flow model, flow-through IS systems can be simulated with respect to time.

To illustrate the relationship between these volume fractions, figure 4.8 illustrates the power fraction and W-plane mapping as a cell traverses through the co-planar electrode chamber.

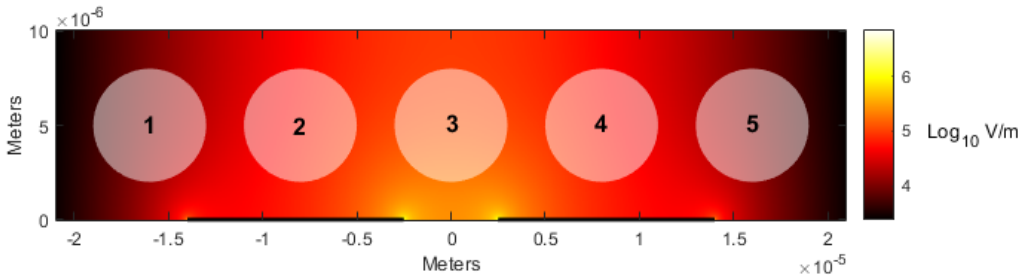

(a) Particle position overlay on the electric field magnitude plot of a co-planar electrode system.

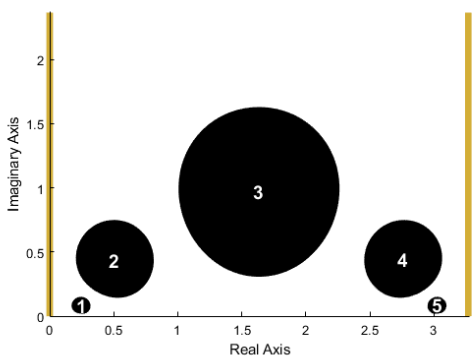

(b) Particle mapped to the W-plane.

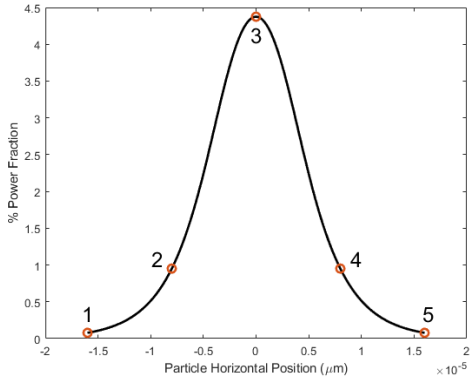

(c) Calculated power fraction of the particle.

Figure 4.8: Illustration of the W-plane particle mapping and the power fraction. (b) depicts the mapped region of an ideal parallel electrode system occupied from a particle in a co-planar electrode system.The gold colored y axis represent the systems electrodes.

As expected, both illustrations of the power fraction indicates the maximum volume fraction as the particle passes through the center of the electrode chamber. It should also be noted how the orthodrome of the particle mapped to the W-plane becomes deformed, which will contribute error to the W-plane volume fraction esti-

mate described by equation 4.39. Although the power fraction is the more accurate tool in calculating the volume fraction, the W-plane mapping is a powerful tool in visually investigating the effects of cell position, chamber geometry, and electrode geometry.

4.1.4 Device Sensitivity

Linderholm defined the sensitivity of a device as the local dissipation of power normalized by the total power of the system. In otherwords, Linderholm sensitivity is the ratio of power density at a point in the system to the power of the system, and can be expressed as

$$S_{Linderholm} = \frac{\rho|j|^2}{R_{sys}V_{sys}^2} \quad [52]. \tag{4.52}$$

The Linderholm definition of sensitivity takes into account the non-uniformity of the electric field, but does not include the particle size and dielectric properties of the particle and the medium.

If instead of taking the ratio of power density at a specific point to the power of the system, the ratio of power in the region of the particle to the power of the system is calculated, we arrive at the power fraction described in equation 4.41. The power fraction, as a measure of sensitivity, extends Linderholm's sensitivity to account for the size and shape of the particle.

Sun proposed an alternative sensitivity definition as the ratio of relative impedance to the impedance of the medium:

$$S_{Sun} = \frac{||\tilde{Z}_{mix}| - |\tilde{Z}_m||}{|\tilde{Z}_m|} \quad [31]. \tag{4.53}$$

Sun's definition has the advantage of taking into account the dielectric properties of the suspension. However, his calculations used the standard method of determining the volume fraction, which do not account for the non-uniformity of the electric field local and the position of the particle.

By using the power volume fraction with Sun's definition of sensitivity, we get the advantages of both sensitivity definitions: the ability to account for dielectric properties, and local non-uniformity in the power density over the region of the particle.

When choosing a sensitivity metric to optimize the device, the power fraction or Linderholm's sensitivity should be employed when only concerned with optimizing the geometry of the device. Sun's definition of sensitivity is useful in considering the medium used in the device.

4.1.5 Analytic Impedance Modeling Tool

The analytic impedance solution for co-planar electrode systems was implemented in the MATLAB programming language. To facilitate simulation and exploration of the analytic impedance solution, the IS App was created. The IS App collated the analytic impedance solution into a single program with a graphical user interface. The main page of the application is displayed in figure 4.9. The IS App is split into three sections: impedance spectroscopy, equivalent circuit values, and the electric field and volume fraction analysis.

Impedance Spectroscopy

The main section of the IS App is the impedance spectroscopy simulation. The parameter entry section is located on the right side of the user interface depicted in figure 4.9 and allows the user to dictate the parameters in the analytic impedance solution. It is important to keep in mind that the analytic impedance solution assumes that the channel length continues infinitely, but the electrode geometry, channel height, and particle geometry can all be specified.

The parameters *RelTol* and *AbsTol* under the *Volume Fraction* subsection affect the acceptable error tolerance when calculating the power volume fraction. Smaller values will provide more accurate answers at the expense of computing time. In most cases, the default values are more than sufficient. The current application requires so little computing time that there is little reason to increase the tolerance

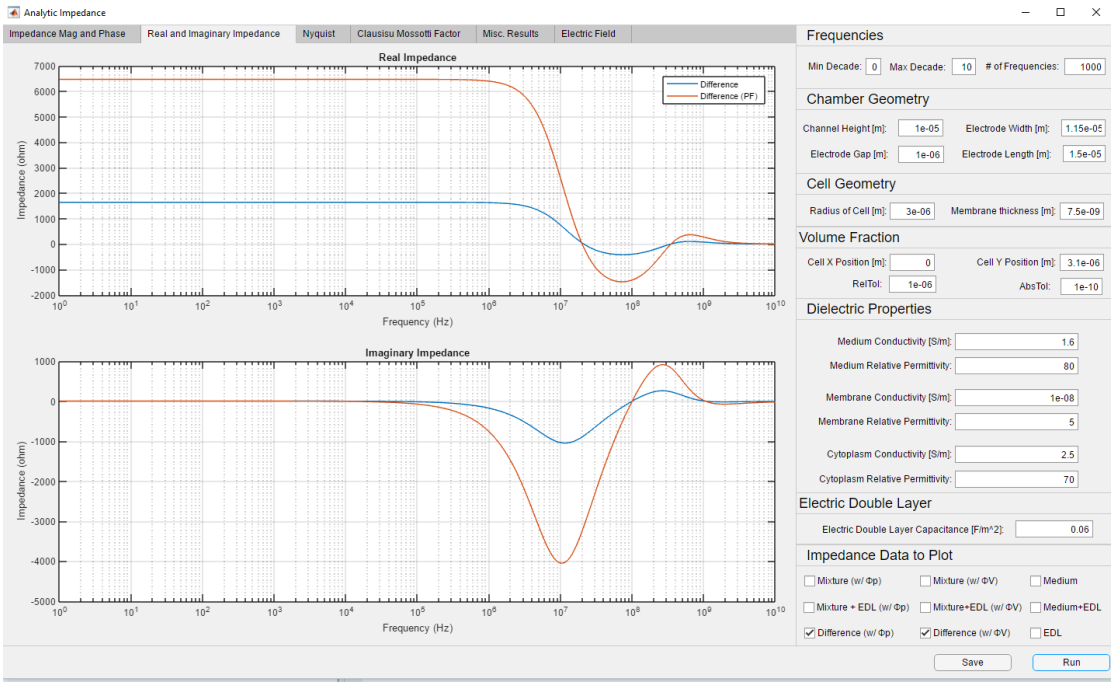

Figure 4.9: The IS app GUI created in MATLAB to calculate and display the analytic impedance solution to a single cell suspension over co-planar electrodes. The impedance is displayed as magnitude-phase, real-imaginary, and Nyquist plots. The IS app also includes the capability to calculate the Clausius Mossotti spectrum, an equivalent circuit model, the electric field of the co-planar electrode system, and a mapping of the cell orthodrome to the W-plane.

parameters from their default value, and few applications would require higher precision than currently provided.

The electric double layer capacitance parameter determines the effect of the EDL on the model. The model takes the simplest approach to the EDL and represents its as two capacitors in series to the analytic impedance solution. The capacitance is calculated by finding the product of the capacitance per unit area and with the area of the electrodes. Implementation of sophisticated EDL models should be considered for further development of the IS App.

The checkmarks under the *Impedance Data to Plot* subsection dictates what data sets will be plotted and saved after running the simulation. The *mixture*, *medium*, and *difference* option denote the impedance solution of the single cell suspension, no-cell solution, and the difference between the single cell suspension and the no-cell solution impedance respectively. The *EDL*, ϕV, and ϕp options calculates the analytic impedance solution with the electric double layer, the traditional

volume fraction, and the power fraction respectively.

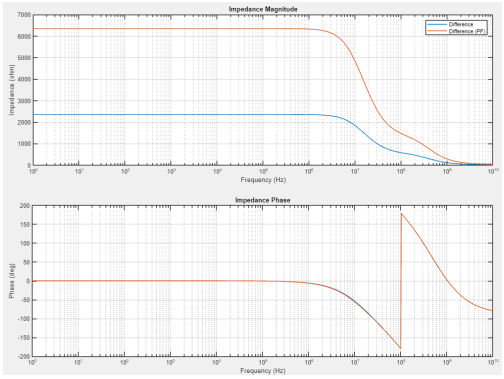

(a) Impedance magnitude and phase

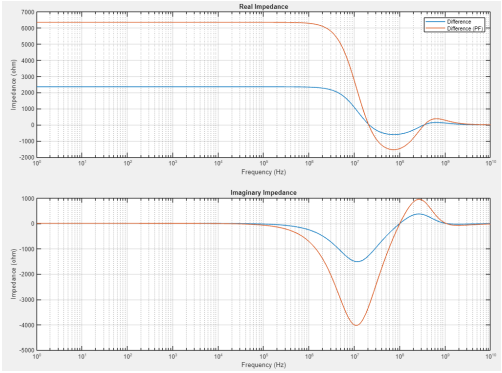

(b) Real and imaginary impedance

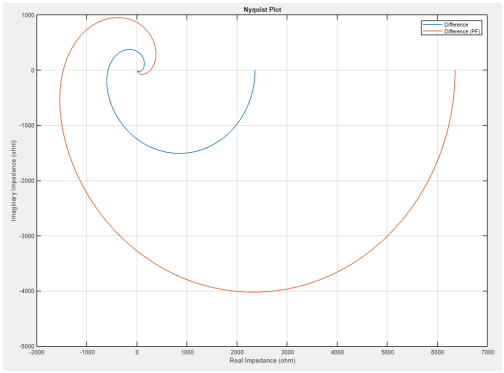

(c) Nyquist plot

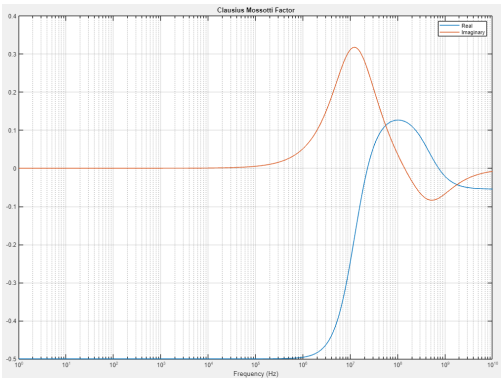

(d) Clausius Mossotti Factor

Figure 4.10: Example plots depicting results of the analytic impedance solution generated by the IS App.

The IS App visualizes the results as impedance magnitude-phase plots, real-imaginary parts, a Nyquist plot, and the real and imaginary parts of the Clausius Mossotti factor. An example of the plots is given in figure 4.10.

Equivalent Circuit

The equivalent circuit section of the the IS App uses the Foster-Schwan model to calculate the equivalent circuit values for the single cell suspension described by the parameter entries displayed in figure 4.9. A full explanation of the Foster-Schwan model is provided in section 2.3.4. The equivalent circuit section of the IS App is displayed in figure 4.11. For comparison purposes, the equivalent circuit values using both the traditional volume fraction and the power fraction are provided.

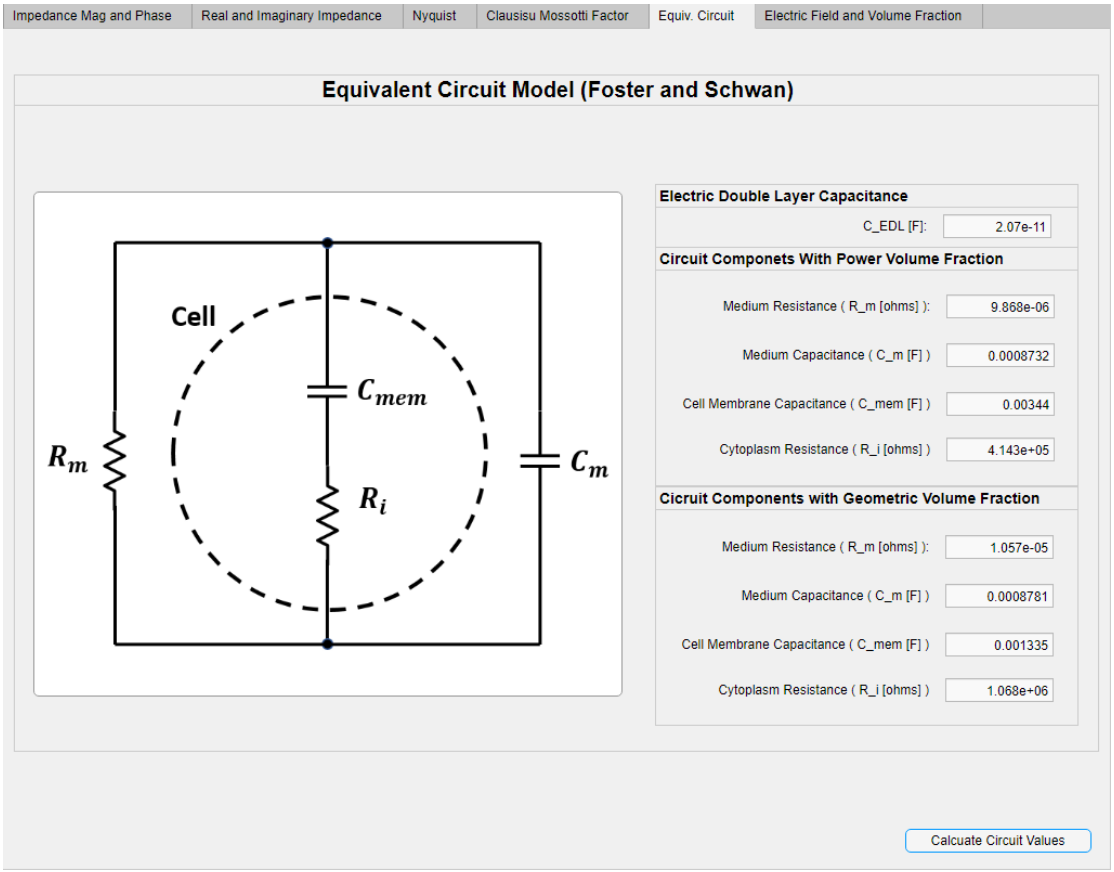

Figure 4.11: The IS app display for the equivalent circuit model of a single cell suspension. The application uses the Foster-Schwan model to calculate circuit values with the geometric and power volume fractions.

Electric Field and Volume Fraction

The electric field and volume fraction section of the IS App was created to depict how the geometry of the system affects the electric field and volume fraction. The electric field and volume fraction section of the program is displayed in figure 4.12.

The top chart in figure 4.12 depicts the logarithm electric field magnitude of the co-planar electrode system. Since this analytic impedance solution describes an infinitely long channel, the width of the calculated electric field must be truncated. The user is given the ability to control the width of the data calculated with the *Plot width multiplier* parameter. The parameter determines the width of the calculated electric field with the following relation:

$$\text{Data Width} = (\text{Plot width multiplier}) * (2w_{electro} + g_{electro}),$$

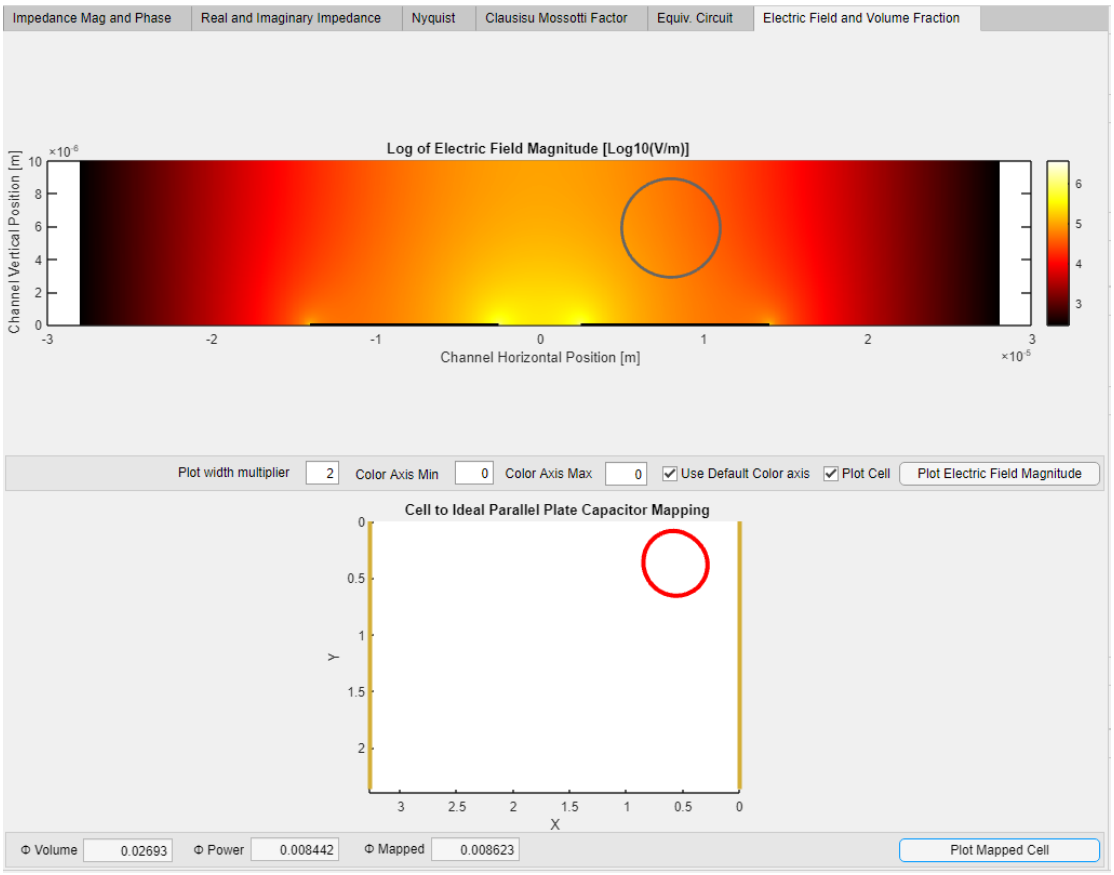

Figure 4.12: The IS app display for the electric field magnitude, the cell orthodrome mapping to the W-plane, and volume fractions.

where $w_{electro}$ is the electrode width, and $g_{electro}$ is the gap between the electrodes. In addition, the user can specify the color bar range plotted with the *Color Axis Max* and *Color Axis Min* parameters. Altering these parameters is useful when the area of interest is over-saturated by the color axis extrema, or the user desires to identify where a bounded range of the electric field magnitude occurs. If the plot cell checkbox is selected, the orthodrome perimeter of the cell is plotted.

The bottom chart in figure 4.12 plots the transformed orthodrome perimeter of the cell to the ideal parallel plate capacitor plane (W-plane) using the SCM-derived mapping described by equation 4.25. The depiction of the cell orthodrome in the W-plane provides a direct illustration of how the position of the cell in the chamber affects its effective volume fraction. In addition, the calculated values of the traditional, power, and mapped volume fraction are provided in the bottom left corner.

4.2 Finite Element Analysis

Finite element analysis (FEA) models were developed to characterize the single cell impedance spectrum and to investigate optimal co-planar electrode configurations with the purpose to inform future designs. To accomplish this goal, four FEA models were designed:

- Simple medium: a basic model that only includes electrodes and medium inside a rectangular domain.
- Simple cell: a basic model inclusive of the simple medium model with the addition of a cell centered over the electrodes.
- Device medium: a model that replicates the designed geometry of the Cal Poly Biofluidic Lab's impedance spectroscopy device. The model only includes electrodes and the device medium.
- Device cell: inclusive of the the device medium model with the addition of a cell centered over the electrodes.

Figure 4.13 depicts the four models. The simple models will investigate the characteristics of an ideal co-planar electrode cell and provide model validation by comparison to the analytic impedance solution. The device models will provide insight into the impedance characteristics of the Cal Poly Biofluidics Lab's impedance spectroscopy device.

4.2.1 Model Development

The simple medium, simple cell, device medium, and device cell models were created using COMSOL Multiphyisics FEA software with the electric current physics module. Model development included the specification and implementation in COMSOL of geometry, material properties, and governing physics.

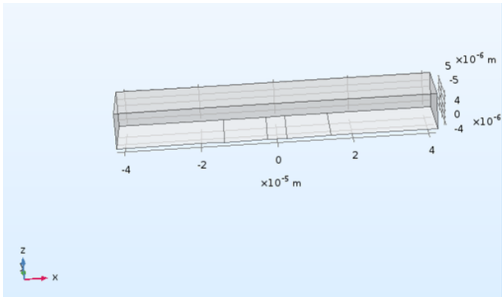

(a) Simple medium model

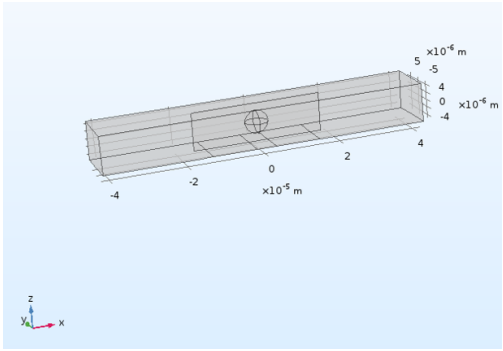

(b) Simple cell model

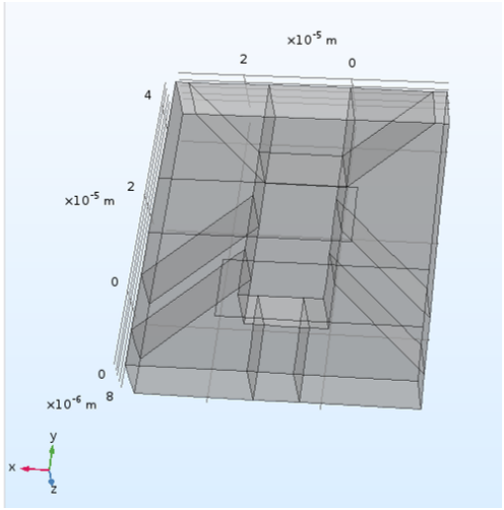

(c) Device medium model

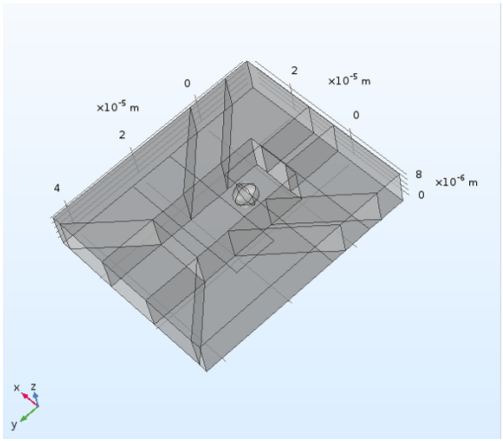

(d) Device cell model

Figure 4.13: The four finite element analysis models depicted in COMSOL. The simple medium and simple cell models are based off the geometry used for the analytic impedance solution. The device models are based on the geometry of the Cal Poly Biofludic Lab's impedance spectroscopy device.

Model Geometry

Two geometries were developed for the impedance spectroscopy models: a basic rectangular electrode cell for the simple models, and an implementation of the impedance spectroscopy device for the device models. The simple geometry is depicted in figure 4.13a and 4.13b, and the device geometry in figure 4.13c and 4.13d. Dimensioned drawings are presented in figure 4.14 and figure 4.15 for the simple and device models respectively.

In general, the simple geometry attempts to follow two of the assumptions made in the analytic impedance solution with reference to the electrode orientation given

in figure 4.1:

1. The electrode fringe fields are allowed to expand infinitely in the $\hat{\imath}$ direction (i.e. there are no horizontal bounds).

2. The electric field has no component in the $\hat{\jmath}$ direction (i.e. geometry must be uniform in the direction parallel to the electrodes).

The simple geometry approximated assumption 1 by making the sensor chamber sufficiently long. An iterative approach determined the sufficient length of the chamber by repeatedly increasing the length of the chamber until the model impedance stabilized to a constant value.

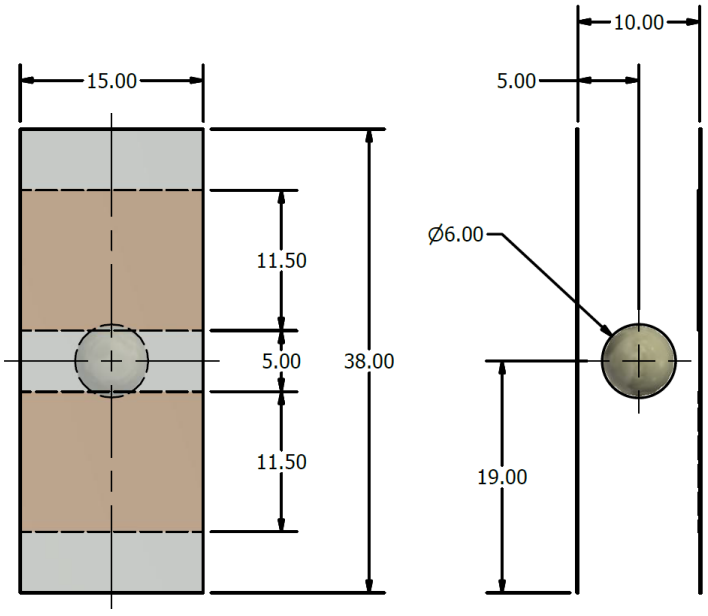

Figure 4.14: Drawing of the Simple FEA models' geometry. The simple medium model excludes the 6 μm diameter cell. All units of length are in microns.

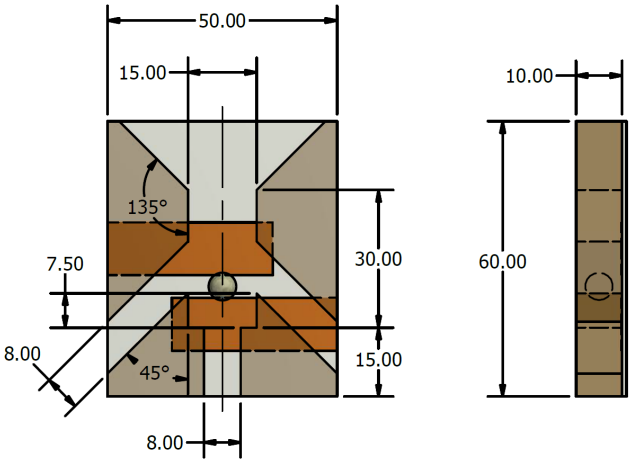

(a) Drawing of the geometry used in the device FEA model with dimensioned system and PDMS geometry. All dimensions of length are in units of microns.

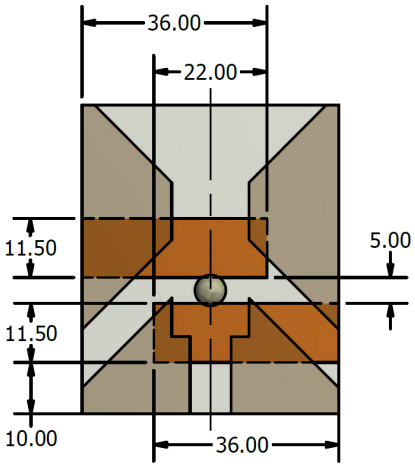

(b) Drawing of the geometry used in the Device Medium and Device Cell FEA models with dimensioned electrode geometry. All dimensions of length are in units of microns.

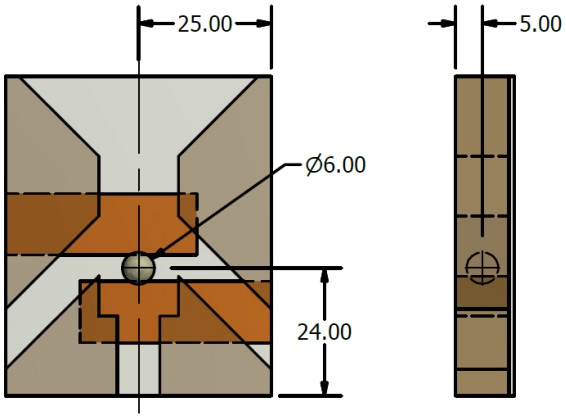

(c) Drawing of the geometry used in the Device Cell FEA model with dimensioned cell geometry. All dimensions of length are in units of microns.

Figure 4.15: Drawing of the Device FEA geometry models. All dimensions of length are in microns.

At this point, any additional fringe fields permitted by an infinitely long channel was assumed to be negligible. This approach led to an optimal model length of 38 microns. The second assumption was met by creating uniform features in the $\hat{\jmath}$ direction.

The device geometry focused on the sensor chamber of the impedance spectroscope device and assumed that the effects of the electrodes far from the chamber are negligible.

The cell version of both geometries includes a cell centered over the electrodes with the cell center 5 microns above the electrodes. The cell was modeled as a 6 μm diameter sphere of cytoplasm. The 7.5 nm cell membrane is implemented in the physics.

Material Properties

The materials used in the FEA models included the medium solution, the cell membrane, cytoplasm, and polydimethylsiloxane (PDMS). For each of these materials materials, the conductivity and relative permittivity were specified and are summarized in table 4.1.

Material	Conductivity	Relative Permittivity
Solution	1.6 [S/m]	80
Cell Membrane	1e-8 [S/m]	5
Cytoplasm	2.5 [S/m]	70
PDMS	2.5E-14 [S/m]	2.6

Table 4.1: The electrical conductivity and permittivity material properties used in the FEA models [30],[22],[53].

Physics

The electric current COMSOL interface set the physical equations for the models. The governing formula is the equation of continuity:

$$\boldsymbol{\nabla \cdot J} = -\frac{d\rho}{dt}, \tag{4.54}$$

where $-\frac{d\rho}{dt}$ is the rate of change of charge density and $\boldsymbol{J}$ is the current density expressed as

$$\boldsymbol{J} = \sigma \boldsymbol{E} + jw\boldsymbol{D} + \boldsymbol{J}_e, \tag{4.55}$$

where $\boldsymbol{E}$ is the electric field, j is $\sqrt{-1}$, w is the angular frequency, $\boldsymbol{J}_e$ is the externally generated current density, and $\boldsymbol{D}$ is the electric displacement field.

All exterior bounds, except for the electrodes, were modeled as perfect insulators with the boundary condition

$$\hat{\boldsymbol{n}} \cdot \boldsymbol{J} = 0. \tag{4.56}$$

The cell membrane was modeled with the contact impedance condition. This is an effective alternative to meshing very thin boundaries. The condition is defined by

$$\hat{\boldsymbol{n}} \cdot \boldsymbol{J} = \frac{\tilde{\sigma}}{d_m} \Delta V, \tag{4.57}$$

where d_m is the thickness of the cell membrane and $\tilde{\sigma}$ is the complex conductivity expressed as

$$\tilde{\sigma} = \sigma + jw\epsilon, \tag{4.58}$$

The contact impedance condition allows current normal to the selected boundary, but does not allow tangential current flow through the boundary. The condition can be used as an effective approximation to thin and relatively non-conductive domains. In the case of the cell membrane, it is an appropriate approximation.

The low and high potential electrodes were set as the ground ($v = 0$) and the applied voltage ($v = v_0$).

The impedance of the system was calculated by dividing the input voltage of $v_0 = 1$V by the system current. The system current was calculated by placing a boundary probe over the ground electrode that integrated the current density over the surface of the electrode. The calculation resulted in the phasor impedance of the electrode cell.

4.2.2 Mesh Development

The FEA models were meshed with quadratic tetrahedral meshes. Mesh convergence studies were run on all four models to determine appropriate meshes and to validate that the model is convergent. To improve the simulation efficiency, the mesh was only refined in the regions over the electrodes.

Each convergence study was based on the calculated resistance of the system (i.e. impedance at 0 hz), which requires integrating the current density over an electrode to find current. In COMSOL, the default settings using the Electric Current module only provides a discretized spatial gradient to the post-processor. When post-processing calculations use the discretized spatial gradient, the result is highly mesh dependent and can result in greater errors. In the simple medium model, this effect manifested as non-zero current values through perfectly insulated boundaries, and the apparent break down of the continuity equation. As a result, an additional error is added to the calculated impedance and the model will require a finer mesh to converge. The effect can be mitigated by applying weak constraints on the boundaries used for post-processing flux calculations. The weak constraint setting provides the post-processor with additional variables that allow for accurate flux calculations. The effect of weak constraints is illustrated in the convergence study of the simple medium model depicted in figure 4.16. Weak constraints were used in the simple models, but due to complicated geometry over the electrodes in the device models, COMSOL was unable to compile the device model simulations with weak constraints and the non-weak constraints were used keeping this shortcoming in mind.

The results of the convergence studies are presented in figures 4.16, 4.17, 4.18, and 4.19. The meshes corresponding to 2.18E5, 2.785E5, 8.45E5, and 8.33E5 degrees of freedom were chosen for the simple medium, simple cell, device medium, and device cell respectively. The chosen meshes are depicted in figure 4.20 with mesh descriptions in table 4.2. The converged meshes were chosen for the simple models and the finest meshes that didn't crash COMSOL during parametric analysis

were used for the device models.

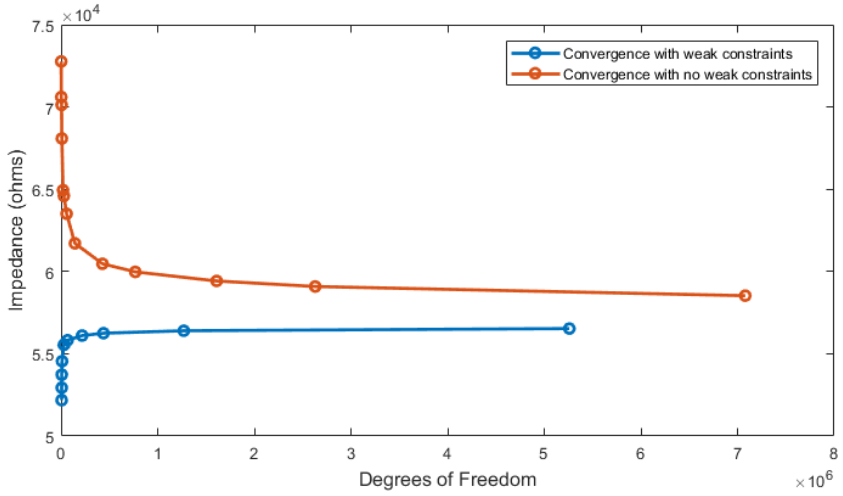

Figure 4.16: Simple medium convergence study using weak and non-weak constraints. The non-weak constraints resulted in added mesh dependence in the impedance calculation. The mesh corresponding to 2.18E5 DOFs was used as the chosen mesh.

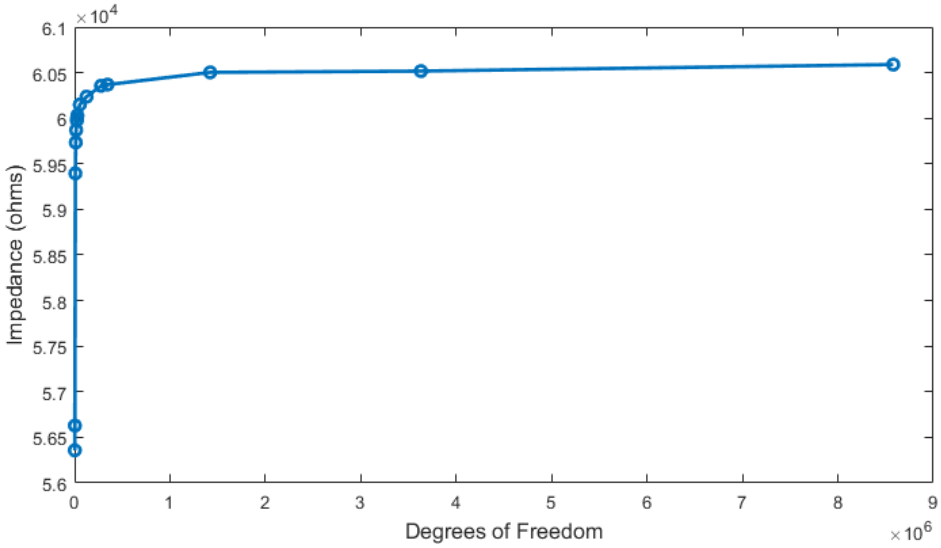

Figure 4.17: Simple cell convergence study. The mesh corresponding to 2.79E5 DOFs was used as the chosen mesh.

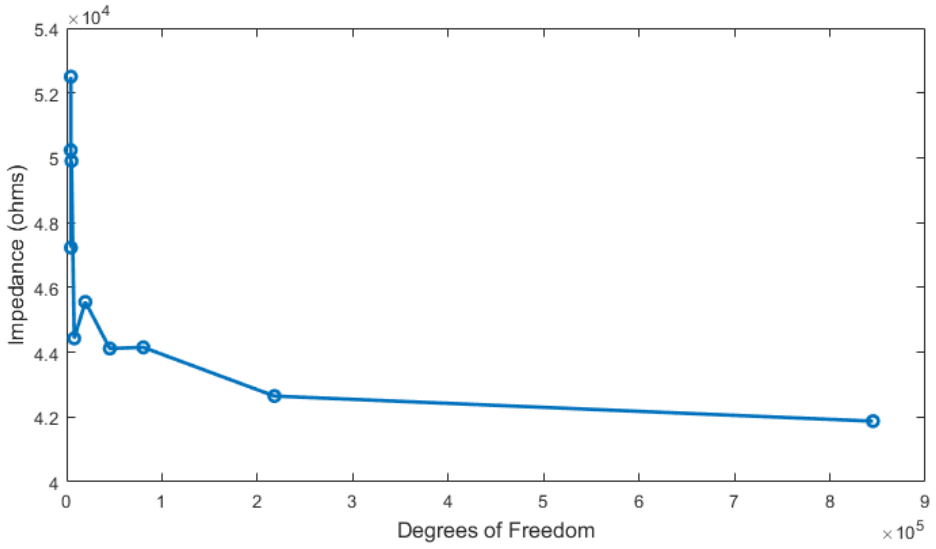

Figure 4.18: Device Medium convergence study. The mesh corresponding to 8.45E5 DOFs was used as the chosen mesh.

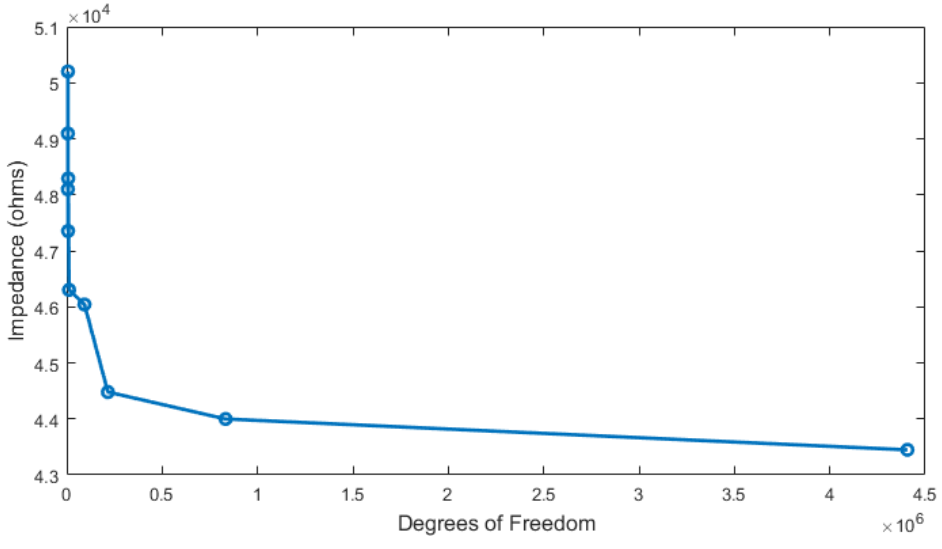

Figure 4.19: Device Cell convergence study. The mesh corresponding to 8.33E5 DOFs was used as the chosen mesh.

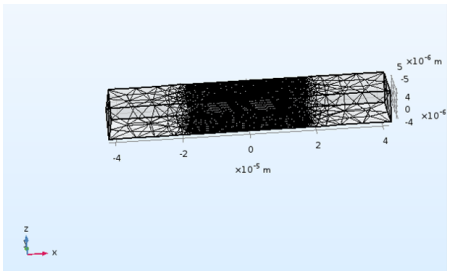

(a) Simple medium mesh with with 2.18E5 DOFs.

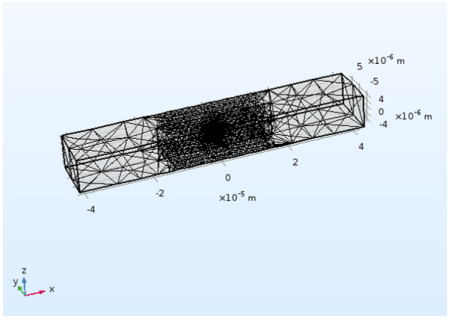

(b) Simple cell mesh with 2.78E5 DOFs.

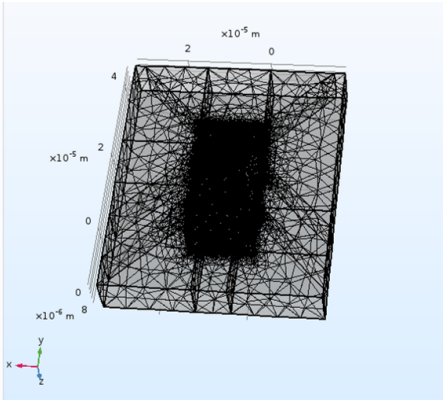

(c) Device medium mesh with 8.45E5 DOFs.

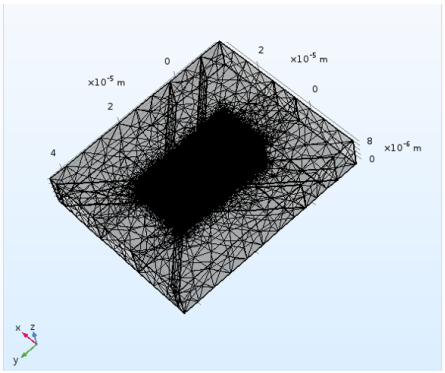

(d) Device cell mesh with 8.33E5 DOFs.

Figure 4.20: Selected finite element analysis meshes.

Model	Number of Elements				Domain Element Quality	
	Triangular	Edge	Vertex	Tetrahedral	Minimum	Average
Simple Medium	6768	298	16	155961	0.2158	0.6683
Simple Cell	7332	327	21	208661	0.2131	0.6689
Device Medium	20901	968	71	626099	0.1891	0.6616
Device Cell	21985	1076	77	615195	0.188	0.6620

Table 4.2: Mesh descriptions and statistics. The triangular, edge, and vertex two dimensional elements line the boundary of the model, while the three dimensional tetrahedral elements fill the volume. The domain element quality is based on the skewness measure.

4.2.3 Model Validation

The FEA models were validated by comparing the analytic impedance solutions to the results of the simple medium and the simple cell models. The analytic solutions were calculated using the the dimensions of the figure 4.14, the material properties

in table 4.1, direct current, and utilizing both the traditional and power fractions. The results of the analytic impedance solutions were overlayed on the simple model convergence studies and presented in figure 4.21 and 4.22.

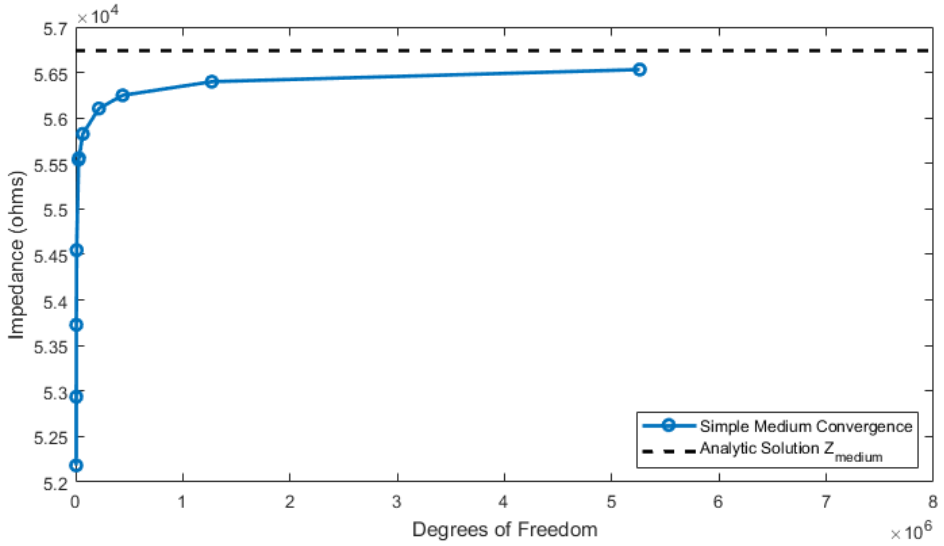

Figure 4.21: A comparison of the medium-only analytic impedance solution and the FEA simple medium convergence results.

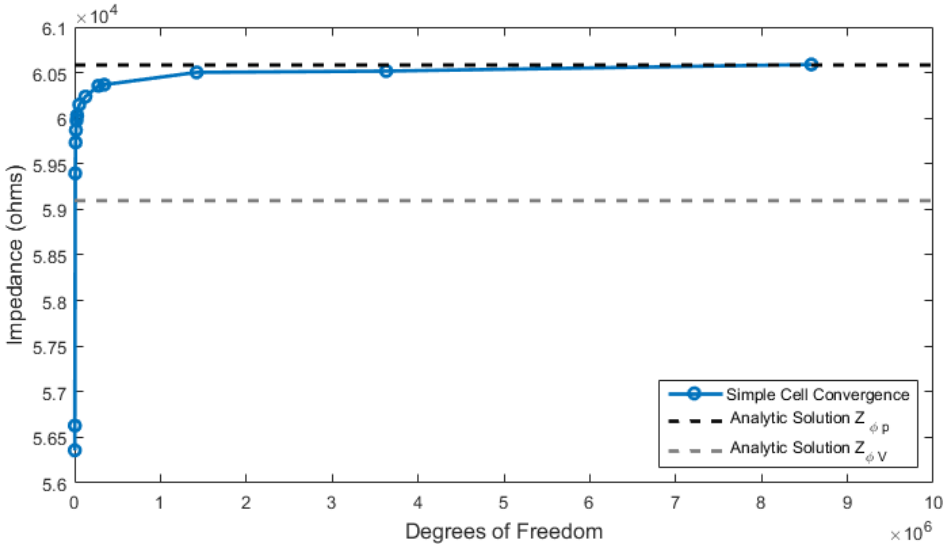

Figure 4.22: A comparison of the FEA simple cell convergence results and the analytic impedance solution using the traditional volume fraction and the power fraction.

A percent error of 0.368% was calculated for the medium comparison, and percent errors of 2.524% and 0.00990% were calculated using the traditional and the power volume fraction for the single cell suspension comparisons respectively. By taking the difference of the medium and the single cell suspension impedance, a

value more closely related to the cell impedance can be obtained. Percent errors of 58.2% and 0.148% were calculated for the traditional and power volume fraction respectively for the difference comparisons.

These results validate the simple FEA models and provides strong evidence that extensions of these models (i.e. parametric analysis, frequency sweeps, and the device models) will provide accurate results. In addition, these results highlight how the use of the the adjusted volume fractions are significantly more accurate than the traditional volume fraction (error with power fraction: 0.148% vs. error with traditional volume fraction: 58.2%).

4.3 Circuit Models

Circuit simulations were developed to validate the IS DAQ system and investigate its shortcomings.

The circuit models were simulated by leveraging the NGSPICE circuit simulator and interfaced to MATLAB to script model execution and analyze results. By interfacing MATLAB to NGSPICE, greater flexibility allowed for multi-variable parametric analysis, programmatic data analysis, and result presentation.

Chapter 5: Results

5.1 Device Fabrication

A functional impedance spectroscopy chip was successfully produced. To create the chip, a PDMS cast was successfully fabricated and validated; a microelectrode fabrication process was developed, and a viable electrode set was created; and the PDMS cast and electrodes were successfully aligned and bonded.

5.1.1 PDMS Cast

Due to the limitations of using the 20,000 DPI photo-plotting service of CAD/Art Services Inc, the produced transparency is only accurate to 8 microns. Consequently, while widths and lengths remained largely unaffected, features, such as square corners on the resolution of microns, were lost. The produced mask largely matched the CAD drawing with the exception of the rectangular cell capture/measurement chamber, which was reduced to a diamond shape. This effect was expected and replicated the results of Fadriquela [4]. Increased accuracy and resolution can be achieved using chrome masks, but at a premium cost that is outside project scope.

The SU-8 master mold matched the transparency and the designed mold height closely. A representative SU-8 mold is depicted in figure 5.1. The sensor chamber portion of the mold, located where all four channels converge, demonstrates the limitation of the transparency mask. Rather than a square chamber, corners are opened up to create a diamond-shaped chamber.

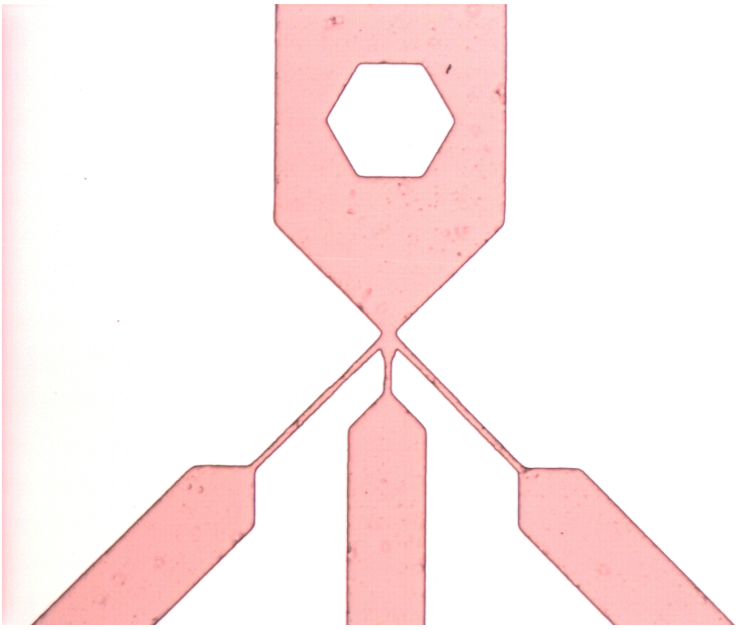

Figure 5.1: SU-8 photoresist as the master mold for PDMS micro-fluidic channels.

The dimensions of the SU-8 mold was verified using the Ambios Xp-1 profilometer. The SU-8 surface profile measured by the profilometer are presented in figure 5.2 and 5.3. Profilometry found that our mold-height closely matched our target height of 10 μm with large chambers at 9.6 μm and the smaller 10 μm chamber at 9 μm.

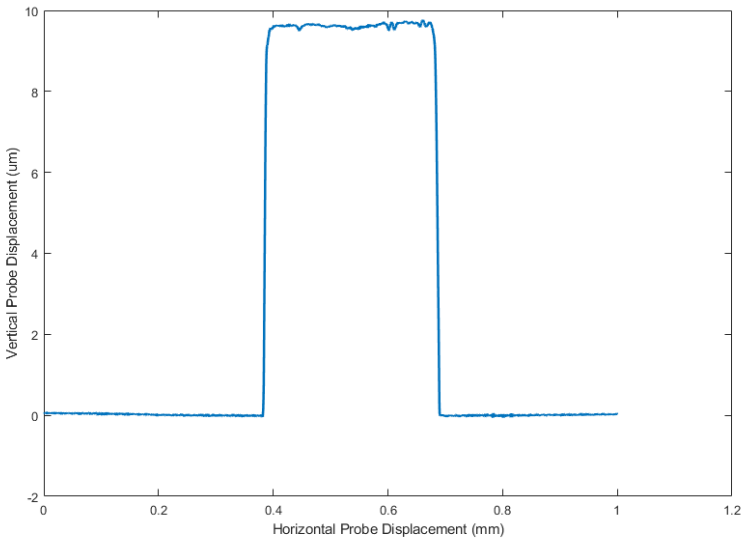

Figure 5.2: Surface profile of a 300 micron wide channel on the SU-8 master mold. The profile was captured with the Ambios XP-1 profilometer. The profilometer recorded a channel height of 9.6 microns.

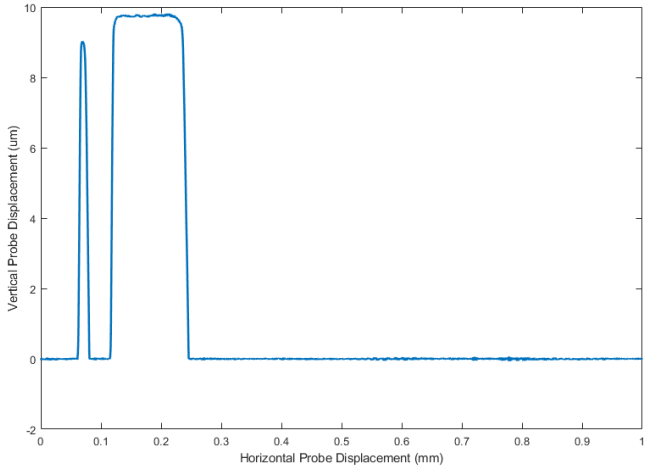

Figure 5.3: Surface profile of a 10 micron and 100 micron wide channel on the SU-8 master mold. The profile was captured with the Ambios XP-1 profilometer. The data depicts the 100 micron channel as about 140 microns wide since it crossed the channel at 45°. The profilometer recorded a channel height of 9 and 9.6 microns for the 10 micron and 100 micron channels respectively.

PDMS casts were successfully fabricated from the SU-8 molds and operation was validated by successfully plasma bonding the casts to glass blanks and verifying channel flow with no leaks or clogs. Figure 5.4 displays a typical PDMS cast. The outlined region represents the effective measurement chamber. The diamond-shaped measurement chamber was carried through all steps of the manufacturing process, originating from the defective transparency mask.

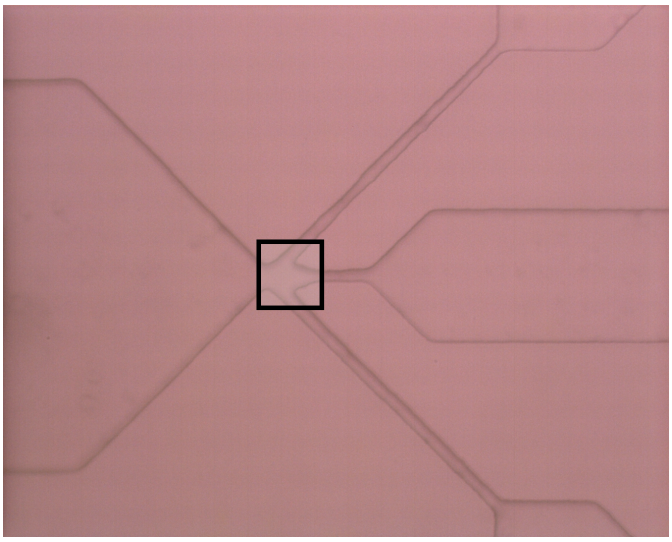

Figure 5.4: PDMS cast of the master mold. Once bonded to a glass substrate, the cast will form the micro-fluidic channels of the device. The outlined region represents the effective measurement chamber.

5.1.2 Electrode Fabrication

The micro-electrode fabrication process was developed with Dr. Hawkins and Foley through the course of this thesis. The fabrication process was developed through an iterative approach of tuning process parameters and was met with many failures before successful fabrication.

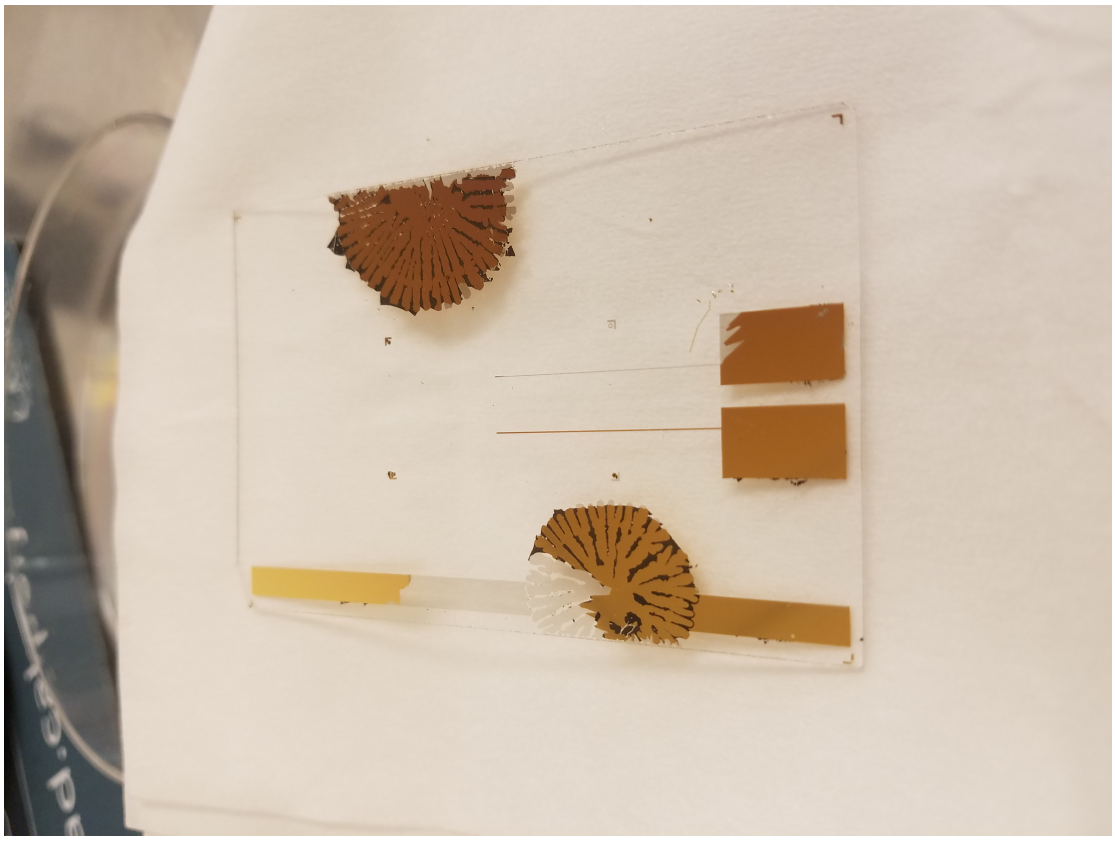

Figure 5.5: Electrode fabrication failure demonstrating two modes of failure: Ma-N1420 photoresist failure to properly adhere to the glass surface manifesting as two anomalous flower patterns, and poor adhesion of the deposited gold to the first chrome layer as evident by gold-stripped leads.

Once the photolithography process was tuned, processed electrodes were met with three main modes of failure: poor photoresist adhesion, poor gold adhesion, and thin cracks or scrapes. Figure 5.5 and 5.6 depict these failure modes at macro and micro scales respectively.

The poor durability of the electrodes was attributed to an overall ineffectiveness of the chromium adhesion layer meant to glue the gold to the glass substrate. The process step of transferring the chromium sputtered wafer from the CrC-150 to the

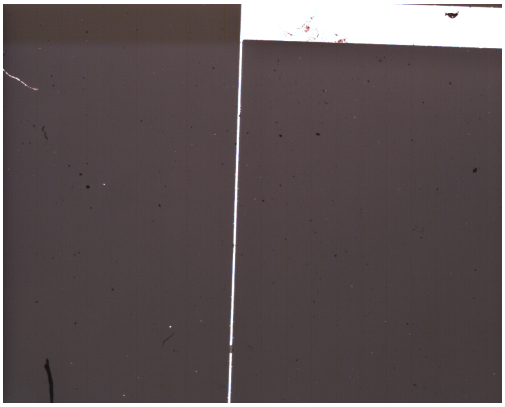

(a) Break in electrode due to delamination of gold strip.

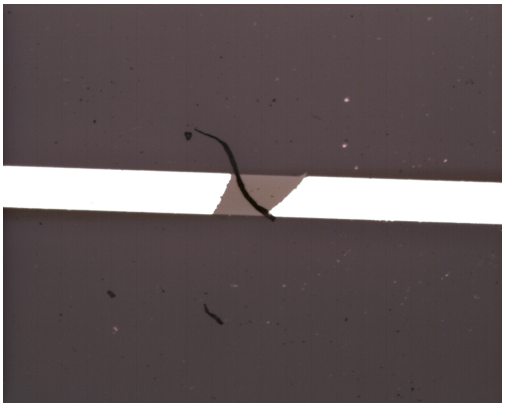

(b) Visible chromium layer at site of electrode delamination highlights failure of gold adhesion to chromium layer.

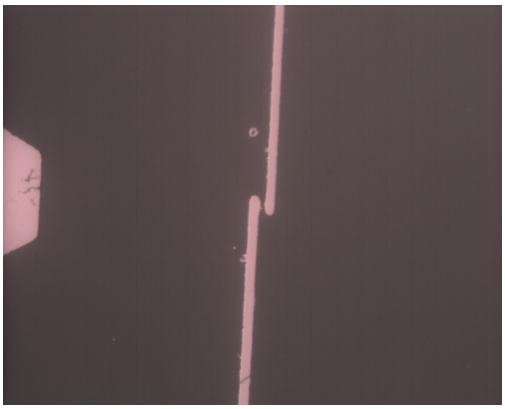

(c) Thin crack in electrode.

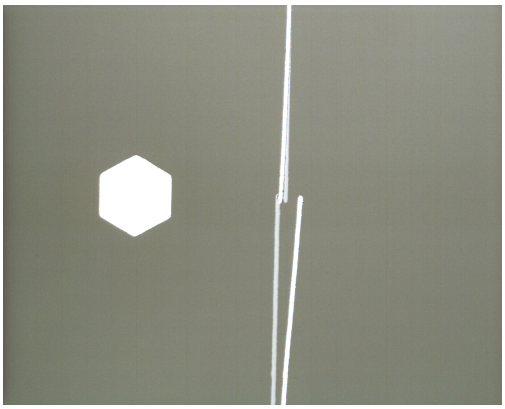

(d) Gold electrode strips sliding off chrome adhesion layer.

Figure 5.6: Images of common electrode fabrication failures.

Denton Desk 5 sputtering system for gold deposition was identified as a likely candidate for the poor chromium-gold adhesion and hypothesized that the formation of chromium oxide during the wafer's exposure to atmosphere was the cause of poor-adhesion. As a consequence, the wafers were held in vacuum until they were quickly transported to the Denton Desk 5. Future microelectrode fabrication processes should take advantage of a dual-target sputtering system that can sputter chromium and gold in series while maintaining vacuum.

With a remedied procedure, two additional sets of electrodes were fabricated. Figure 5.7 depicts representative fabrication results. Overall, both sets of electrodes presented no initial cracking or delamination. However, as discussed in the following section, a set of electrodes manifested adhesion issues during device bonding.

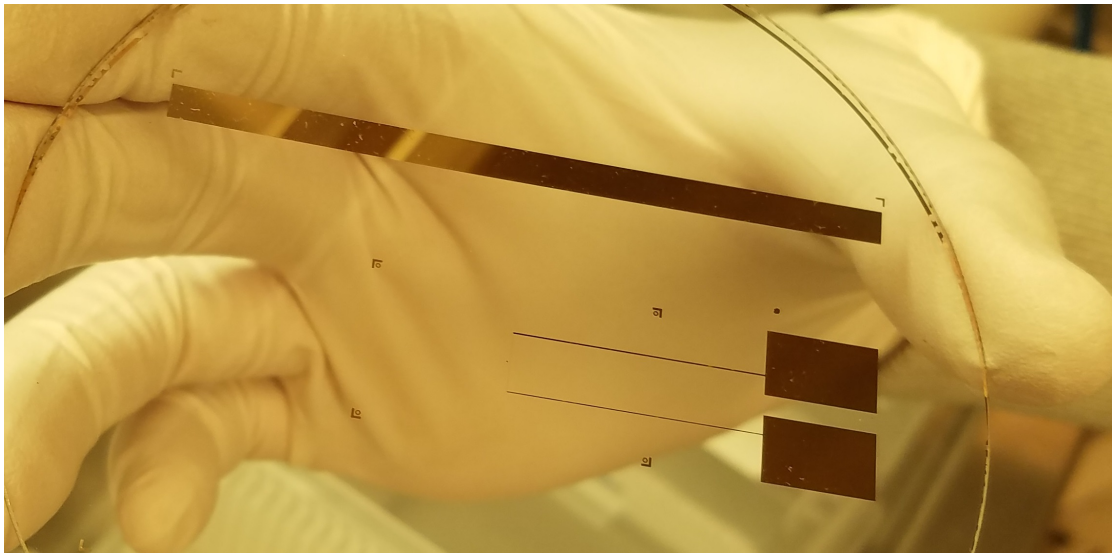

(a) Successful fabrication of device electrodes.

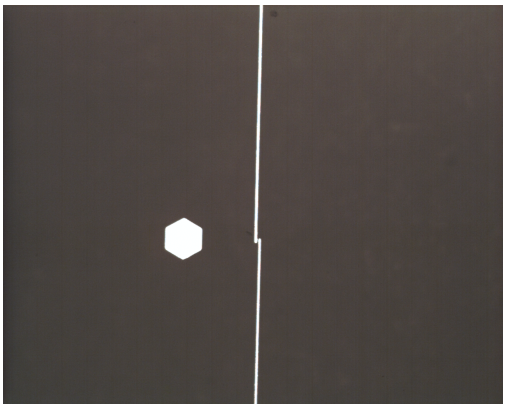

(b) Integral crack-prone segment.

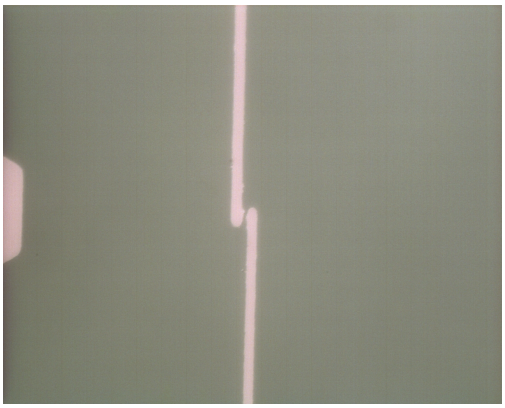

(c) Image of the electrode gap.

Figure 5.7: Integral electrodes with no breaks in sputtered gold layer. The successful results were realized by minimizing the exposure of the chromium adhesion layer to air and reducing the formation chromium oxide.

Microscopy found both sets to be intact with only negligible defects. The successful results are evidence that reducing air exposure of the chromium adhesion layer is a critical process parameter. However, as discussed in the following section, a set of electrodes manifested adhesion issues during device bonding showing that while adhesion has been significantly improved, adhesion-issues continue to persist and supports the need for a dual-target sputtering system.

5.1.3 Device Bonding

By the end of the electrode fabrication process, we had what appeared like two well-adhered and integral electrode chips. Alignment for bonding was completed by hand. The first alignment attempt resulted in delamination of gold from the chromium adhesion layer. Although non-functional, the bonding process for the device was continued to completion. The result of the alignment and bonding for device 1 is depicted figure 5.8.

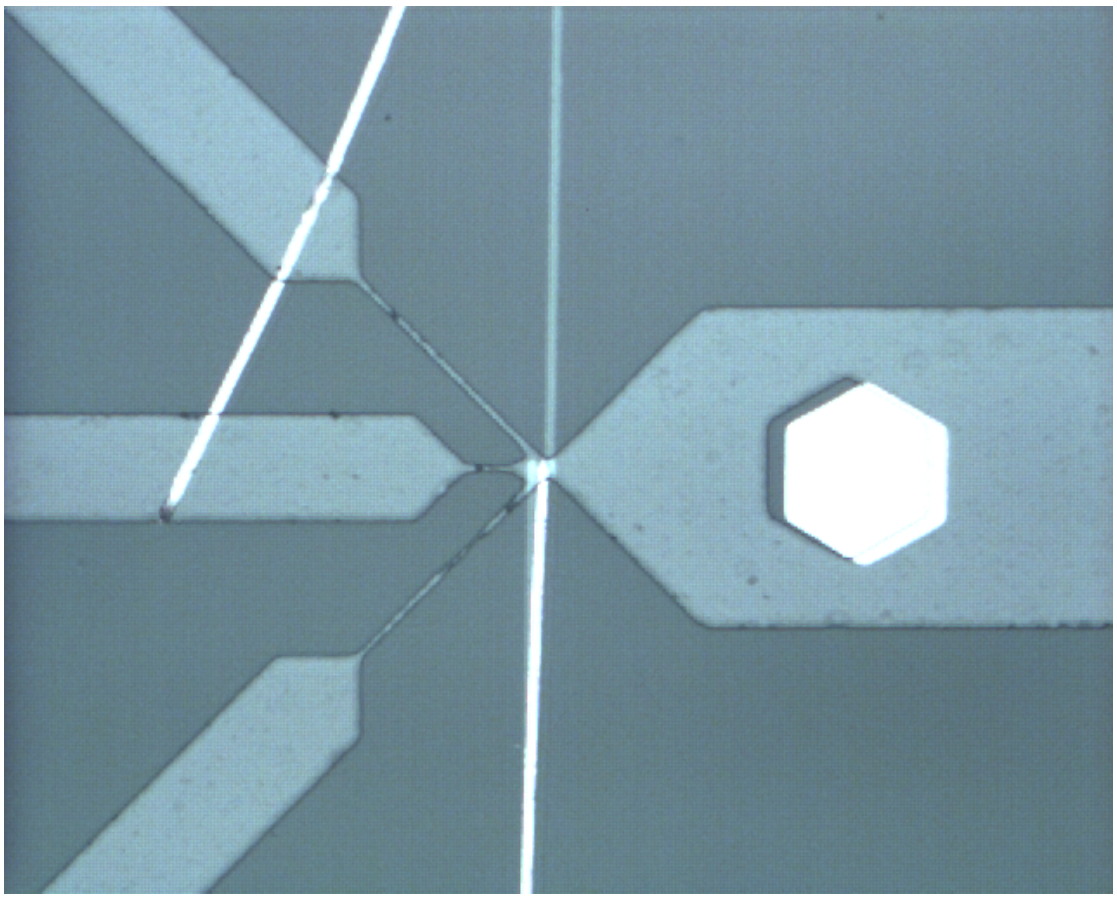

Figure 5.8: Electrode adhesion failure during plasma bonding process of device 1. The sputtered gold layer delaminated from the chromium adhesion layer during PDMS to electrode alignment.

Device 1 was bonded with adequate alignment and exhibited good glass-PDMS adhesion. As evident from the remains of the sputtered chromium layer, the hand alignment was successful in aligning the electrode sensor inside of the PDMS measurement chamber, although slightly biased towards the inlet channel. Tactile testing showed no delamination and the device was successfully used to test microflu-

idic operations. If the electrodes had survived the alignment process, this would be a functional device.

The second attempt resulted in a successful alignment and bonding. Figure 5.9 displays the alignment and bonding results for device 2.

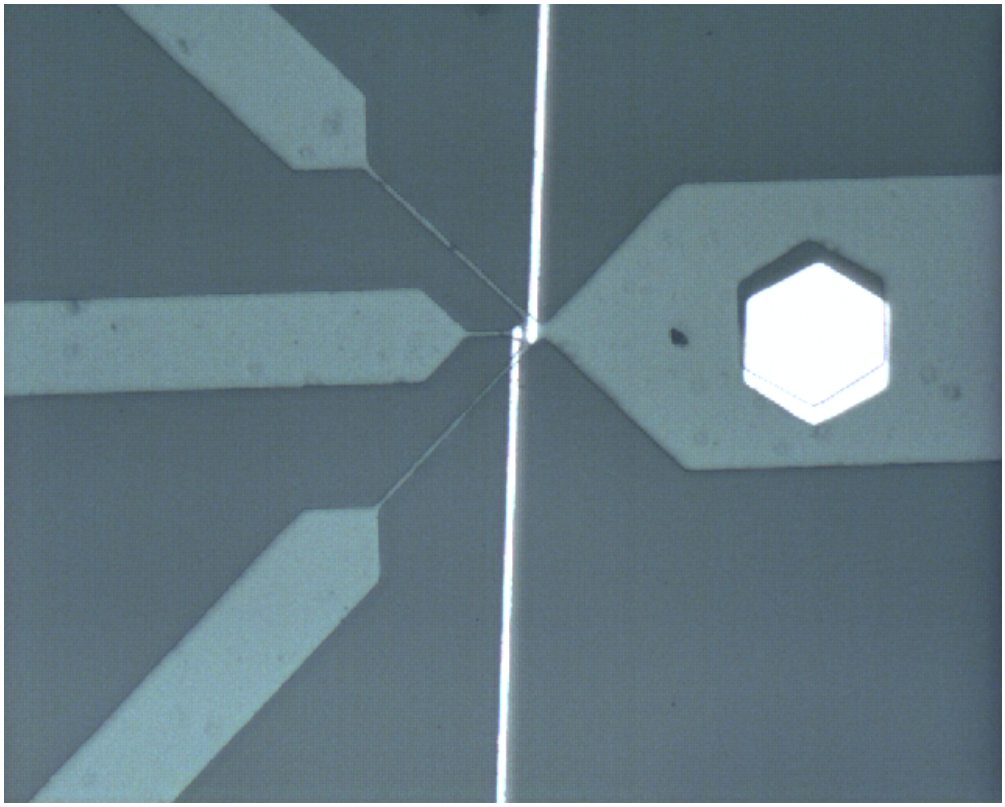

Figure 5.9: Successfully bonded impedance spectroscopy device. PDMS and electrodes were aligned by hand. There is a slight rotational misalignment, but is expected to be functionally negligible.

Device 2 is slightly rotationally misaligned, but is centered on the sensor chamber where the electrodes are nearly perfectly aligned. This rotational misalignment is expected to have only negligible effects on the recorded impedance spectra, but it is a note-worthy topic for potential investigation. The electrodes survived the alignment process with no delamination or cracks. Plasma bonding produced strong PDMS-glass adhesion.

The micro-fabrication results gave us one viable impedance spectroscopy device, and a procedure for creating new viable chips.

5.2 Impedance Spectroscopy System

To characterize and evaluate the impedance spectroscopy system, the microfluidic performance of the IS chip was evaluated, the impedance spectroscopy measurement system was validated, and the performance of impedance spectroscopy with the IS chip was analyzed.

5.2.1 Microfluidic Performance Evaluation

As expected and discussed in chapter 1, the current microfluidic design is not capable of isolating a single cell. This is largely due to the tolerances of the transparency masks as discussed in section 5.1.1. However, the device was evaluated on its ability to flow solutions, saturate the sensor chamber with beads, and clear the sensor chamber of beads. See figure 5.10 for the fully assembled impedance spectroscopy chip under testing.

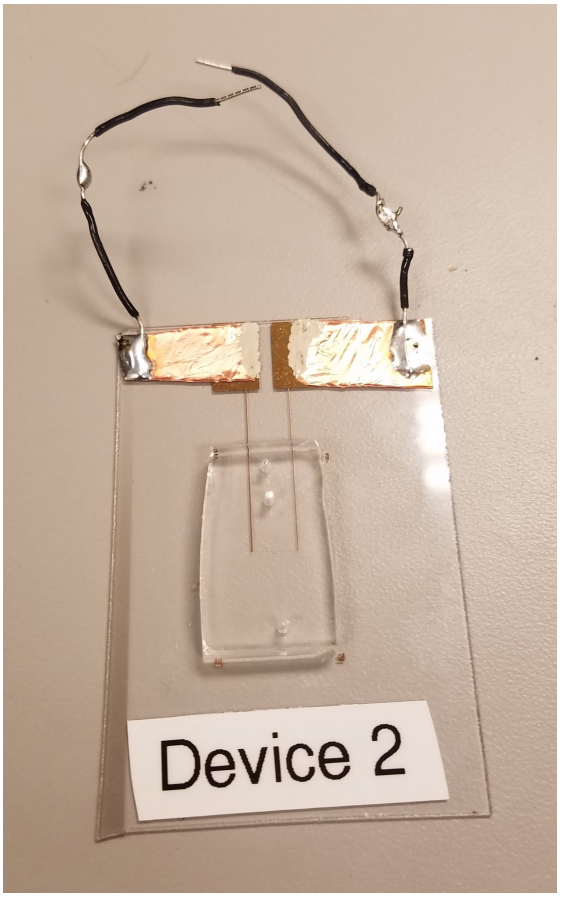

Figure 5.10: Successfully assembled cell impedance spectroscopy device.

Using the the Harvard Apparatus syringe pumps, PBS and DI water were successfully pumped into impedance spectroscopy chip. However, the introduction of 7 μm polystyrene beads initiated debris flow. See figure 5.11 for representative images of IS chip lifecycle.

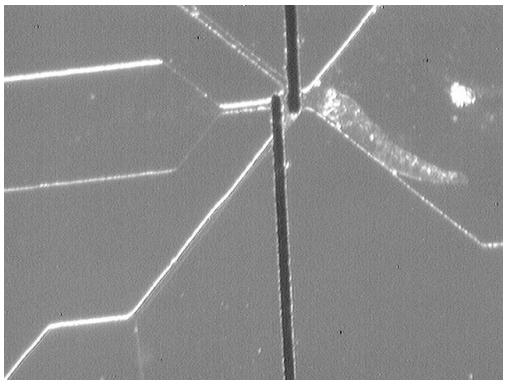

(a) Sensor chamber saturated with phosphate buffered solution.

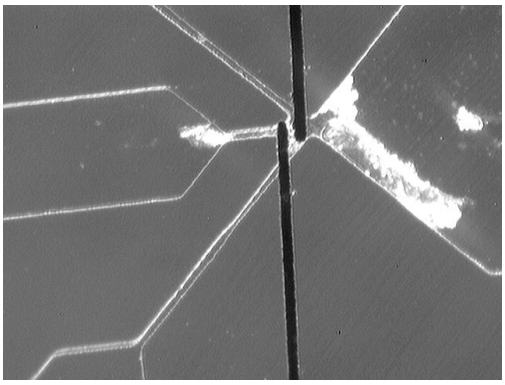

(b) Sensor chamber saturated with 7μm polystyrene beads.

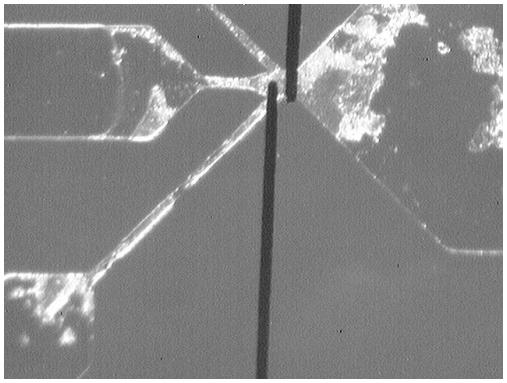

(c) Sensor region jammed with debris and beads.

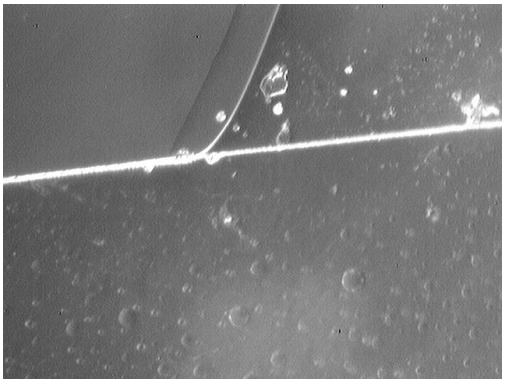

(d) Device delaminated after attempt to flush jammed sensor region.

Figure 5.11: Images of the sensor region of the impedance spectroscopy device. The device successfully measured fluid and 7 μm beads before the sensor region became jammed and the device ultimately delaminated. Images were taken with the LabSmith SVM340 inverted microscope.

As the device channels were saturated with liquid, it became evident that the device channels contained debris, however, no visible debris was present in the sensor chamber and the flows of DI water and PBS did not agitate any debris. All four channels were tested with DI water and proved capable of fluid flow.

The introduction of 7 μm polystyrene beads into the solution initiated debris flow. By significantly decreasing the inlet flow rate, debris flow was minimized and bead suspensions were successfully captured and measured in the sensor cham-

ber. With careful application of alternating flow, the sensor chamber was repeatedly saturated and flushed of microbeads for repeated IS measurements. However, debris progressively aggregated near the sensor chamber and ultimately entered the chamber and clogged the device as depicted in 5.11c. Subsequent attempts to flush the chamber lead to device delaminaton.

Fortunately, a sizable, but limited, body of data was collected. The following section describes the collected data and characterizes the device response to deionized water, phosphate buffered solution, and a suspension of polystyrene beads.

5.2.2 Impedance Spectroscopy Measurement System Validation

The validation of the impedance spectroscopy system focused on the data acquisition system and the impedance calculating circuit. Operation utilizing the cell impedance chip was reserved for the following section.

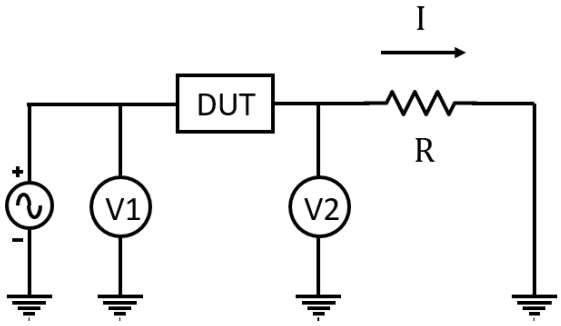

(a) The idealized test circuit.

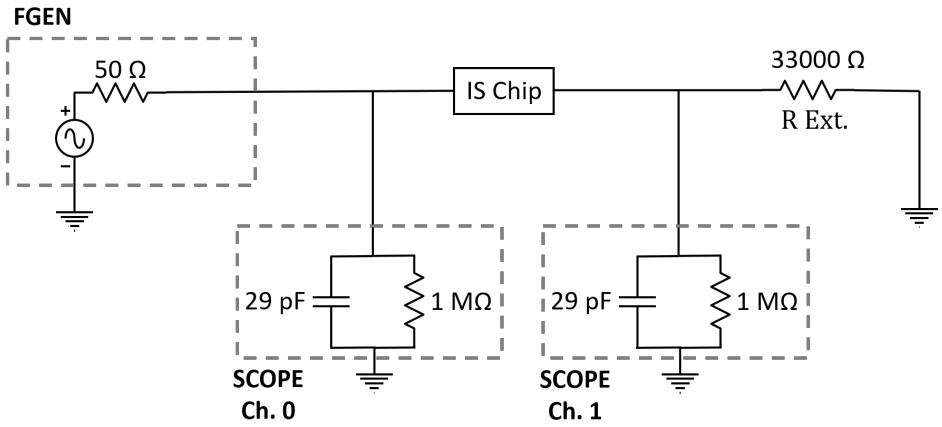

(b) The implemented test circuit.

Figure 5.12: The idealized and implemented I-V circuits. For the validation tests, a 10 pF capacitor was used in place of the IS chip or DUT, and a 33 kΩ resistor was used as the external resistor.

To validate and investigate the impedance spectroscopy DAQ system, the test circuit in figure 5.12b was physically implemented and tested with the IS system. The results were compared to simulations of the implemented circuit and the ideal circuit in figure 5.12a. A 10 pF capacitor was used as the device under testing. The use of the capacitor was justified by noting that the electric double layer will be the largest impedance contributor, and using Gongadze's [44] experimentally determined EDL capacitance of 6 μF/cm^2 for titanium electrodes, and assuming each electrode has a fluid contact area of 11.5 μm by 15 μm, the capacitance of the

EDL for our electrodes can be very roughly estimated as 5.2 pF. Using a capacitor of 10 pF as the DUT is well within the margin of error.

As illustrated in the bode plot of figure 5.13, the measured data and the implemented circuit simulation with scopes largely matched, but there were large deviations from the idealized simulation. The I-V method assumes that all current flowing through the DUT is also flowing through the external resistor R_{EXT}, but with the application of oscilloscope 1, this is no longer the case. All current that leaks through oscilloscope 1 will inflate the calculated impedance of the DUT.

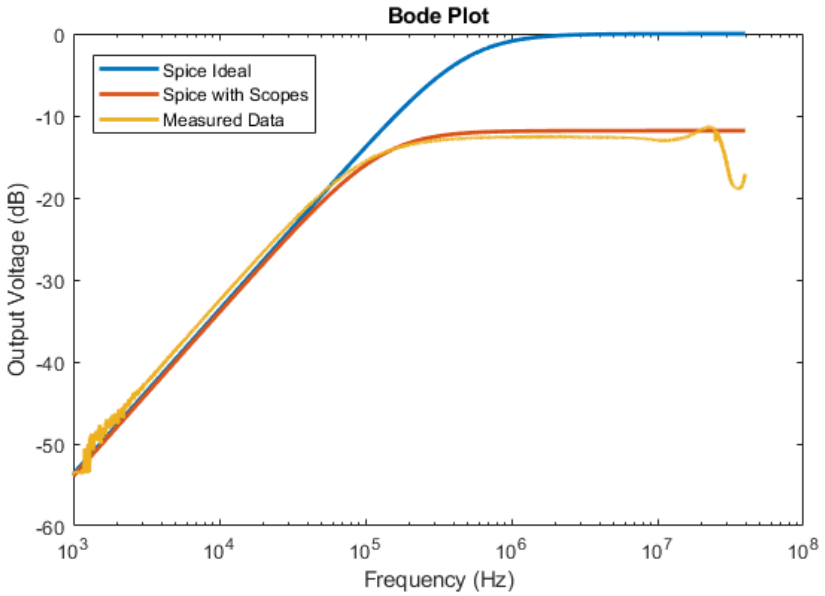

Figure 5.13: Bode plot of the ratio of the voltage out of the DUT to the voltage in.

Revisiting the impedance solution using the I-V method, and referring to figure 5.12 for circuit elements, we have

$$Z_{DUT} = \frac{V_1 - V_2}{I}. \tag{5.1}$$

In ideal scenarios, we would assume all current flows through the external resistor and then $I = V_2/R_{EXT}$. However, we know this is not true: non-ideal properties allows current to flow through our attached oscilloscopes. This additional current flow can be compensated by replacing R_{EXT} with Z_{EXT} to account for the impedance of the oscilloscope and the external resistor.

$$Z_{DUT} = \left(\frac{V_1 - V_2}{V_2}\right) Z_{EXT}. \tag{5.2}$$

Given the equivalent circuit of the oscilloscope, Z_{EXT} can be expressed as

$$Z_{EXT} = \left(jwC_s + \frac{1}{R_s} + \frac{1}{R_{EXT}}\right)^{-1}, \tag{5.3}$$

where C_s and R_s are the capacitance and resistance of the oscilloscope respectively, w is the angular frequency, and j is $\sqrt{-1}$. To correct the data calculated with the uncorrected I-V formula, the following correction function can be applied:

$$Z_{DUT} = Z_{NC}\left(\frac{Z_{EXT}}{R_{EXT}}\right), \tag{5.4}$$

where Z_{NC} is the non-corrected data.

The correction function, equation 5.4, was applied to the measured data and the results are presented in figure 5.14 and 5.15.

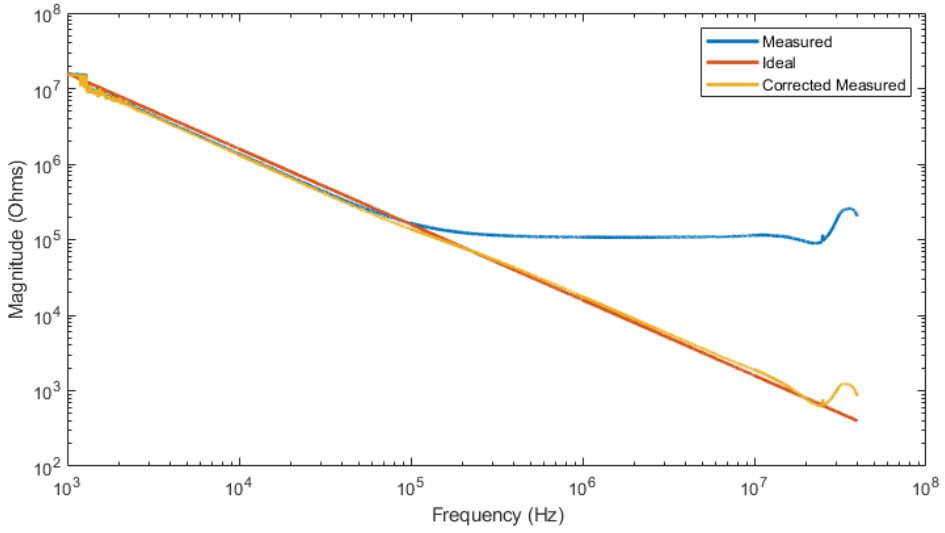

Figure 5.14: Plot of the measured, ideal, and corrected measured impedance magnitude.

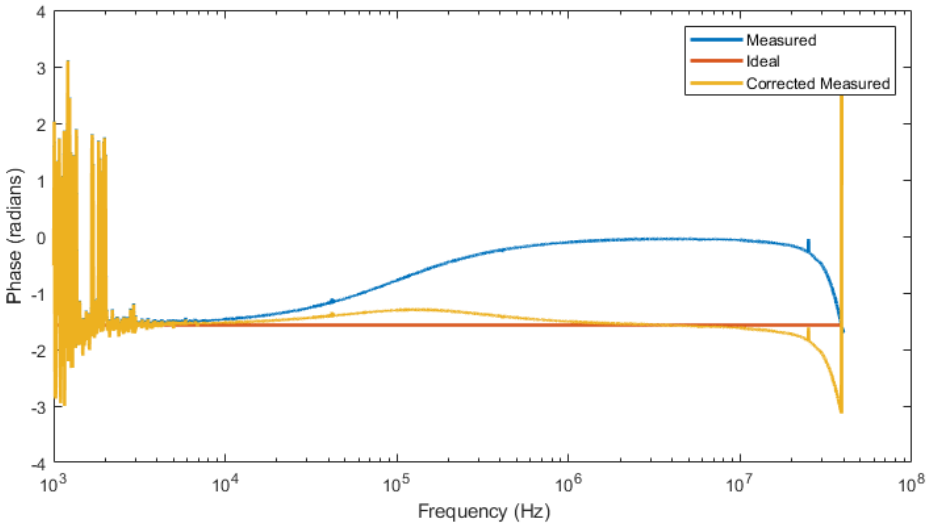

Figure 5.15: Plot of the measured, ideal, and corrected measured impedance phase.

The corrected data displayed in figure 5.14 and 5.15 shows that the application of the correction function significantly decreased the observed deviation from the ideal circuit model, particularly at higher frequencies. This confirms that the oscilloscopes are a source of significant error that needs to be accounted for either through the circuit topology, or through data post-processing as done here. To investigate unaccounted deviations and to quantify residual errors, the measured and calculated errors were compared.

The error associated by attaching the oscilloscope can be quantified as

$$\textbf{\%Error} = 100 \cdot \left| 1 - \frac{R_{EXT}}{Z_{EXT}} \right|. \tag{5.5}$$

Figure 5.16 displays the measured percent error and the error calculated from equation 5.5.

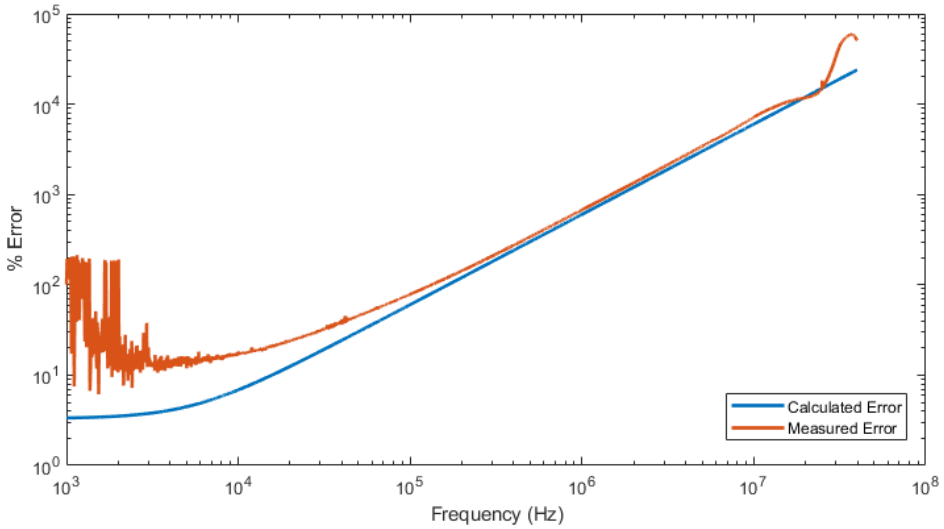

Figure 5.16: Comparison of the calculated percent error caused by the oscilloscopes and the measured percent error.

The calculated error quantifies the error created by adding the oscilloscope circuits to the I-V model while the measured error quantifies the error of the empirical data compared to the I-V model. Although a significant amount error is unaccounted for in the noisy low frequencies and frequencies above 25 MHz, the error due to the attached oscilloscope accounts for a significant amount of error. The remaining residual error is depicted in figure 5.17.

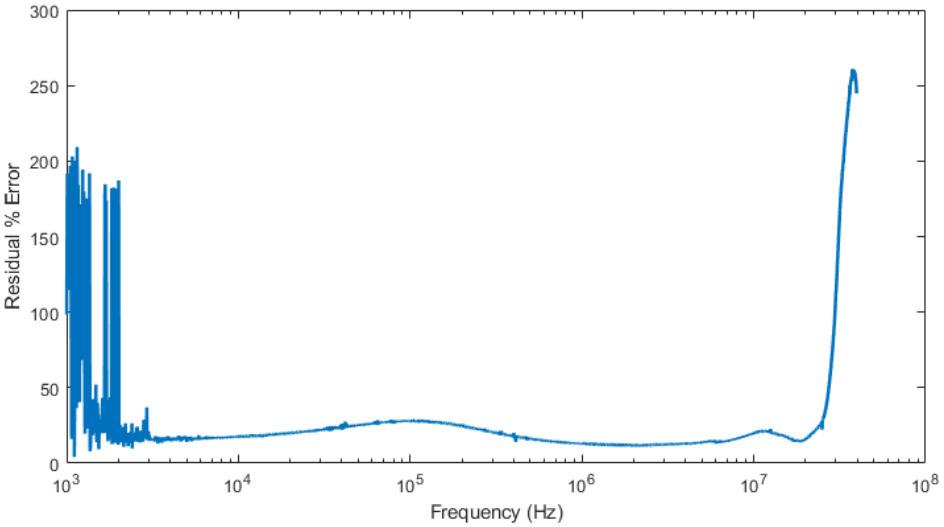

Figure 5.17: Residual percent error of impedance spectra after applying the correction function. Between 3 kHz and 25 MHz, the residual error does not exceed 30%.

Between 3 kHz and 25 MHz, the percent error does not increase beyond 30%, a significant improvement over the exponential error of the uncorrected data. The unaccounted residual error may be attributed to parasitic capacitance in the breadboard and the system at large; deviations in reported values in the external resistor, the oscilloscope, and the test capacitor; and high frequency parasitic inductance. The low-frequency noise is likely caused by the large impedance attenuating the measurement signal (V_2 from figure 5.13) to the noise floor of the system. This could be solved by implementing noise protection into the circuit design, or by increasing the applied voltage signal.

Without revising the current measurement system, and while applying the correction function (equation 5.4), data collected within 3 kHz to 25 MHz can be analyzed with reasonable confidence.

5.2.3 Impedance Spectroscopy Reproducibility

To characterize the reproducibility of the impedance spectroscopy chip, PBS medium samples were tested over three consecutive days. Prior to each measurement, the chip was flushed with DI water and saturated with PBS. Figure 5.18 displays the measured impedance spectra, and figure 5.19 depicts the variation of the sample set.

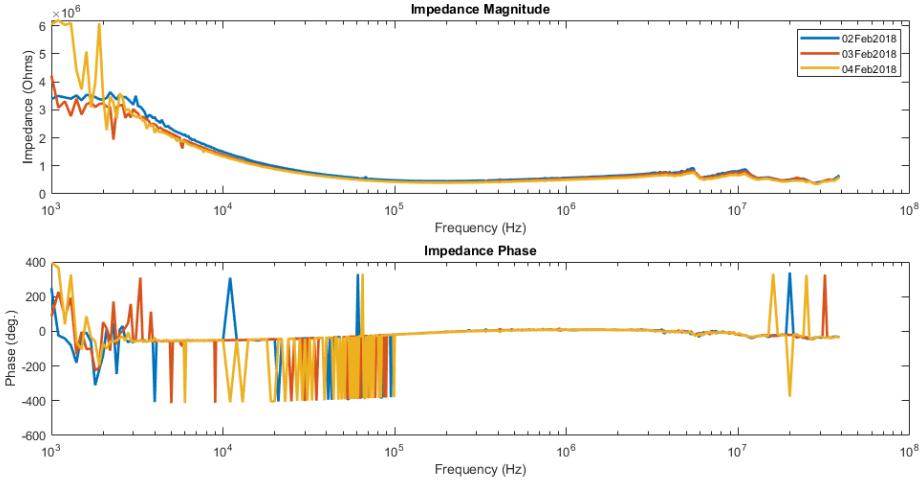

(a) PBS impedance spectroscopy results in polar form.

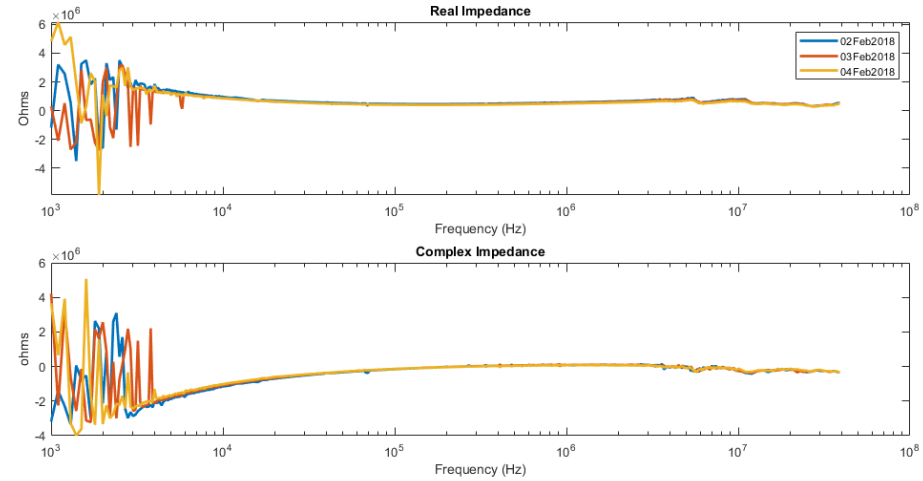

(b) PBS impedance spectroscopy results in rectangular form.

Figure 5.18: Reproducibility of IS measurements demonstrated with repeated measurement of phosphate buffered solution over a span of three days.

As apparent in figure 5.19, there is a considerable amount of variation from 1 kHz to 5 kHZ. This low frequency "noise" consistently occurs throughout all of our

recorded IS data. After 5 kHz, the impedance spectra becomes less variable with a coefficient of variability that fluctuates between 5% and 10%. Although a larger study involving more days of testing, additional solutions, and mixtures, is needed to make a definitive assessment, the current data indicates that impedance spectra measured from 10 kHz to 40 MHz are reproducible.

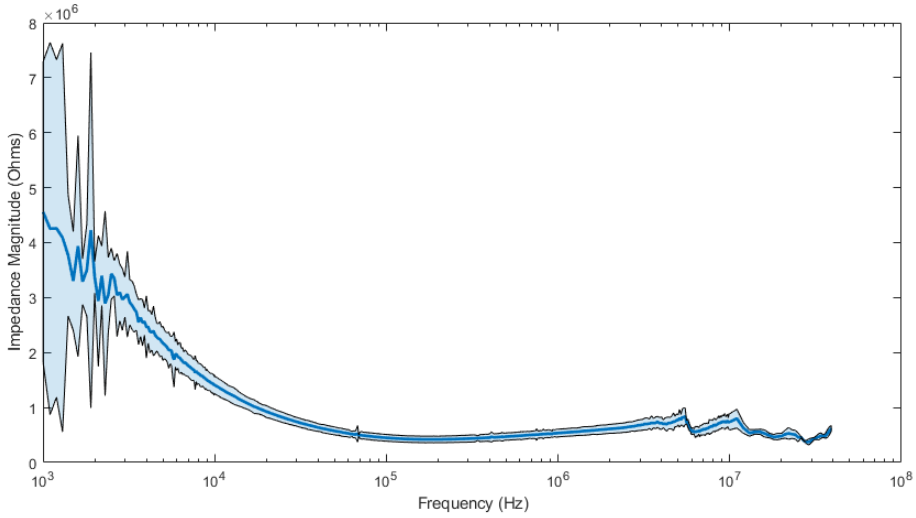

(a) The mean and 2x standard deviation of the impedance magnitude of the reproducibility studies.

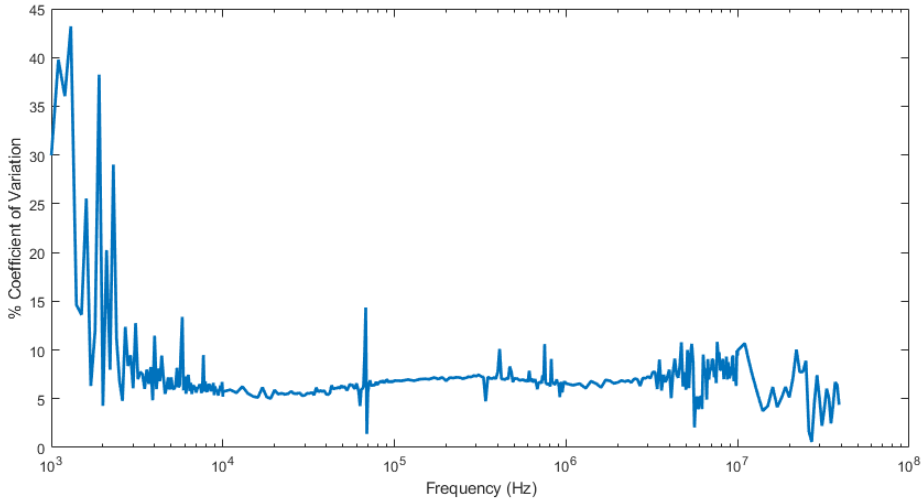

(b) The % coefficient of variation of the impedance magnitude calculated from the reproducibility studies.

Figure 5.19: Measured variability of the reproducibility studies expressed as the standard deviation and the coefficient of variation.

5.2.4 Impedance Spectroscopy Performance

To evaluate the performance of the impedance spectroscopy system, impedance spectra for DI water, PBS, and 7 μm polystyrene beads suspended in PBS were acquired. Representative samples are displayed in figure 5.20.

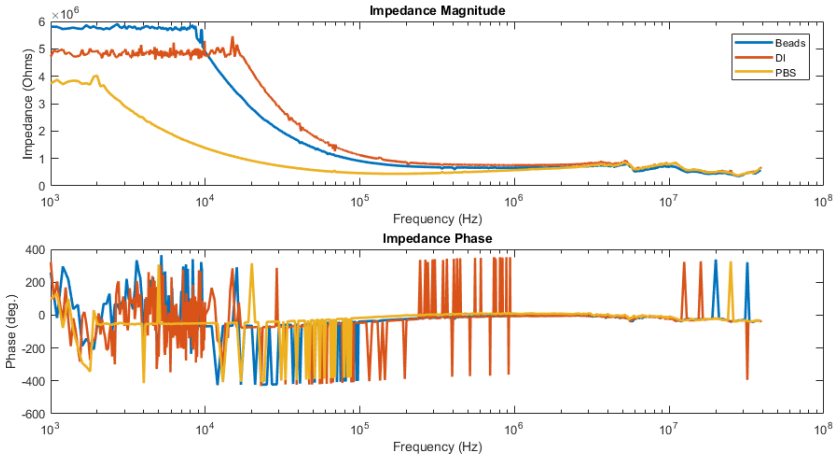

(a) Impedance spectroscopy results in polar form.

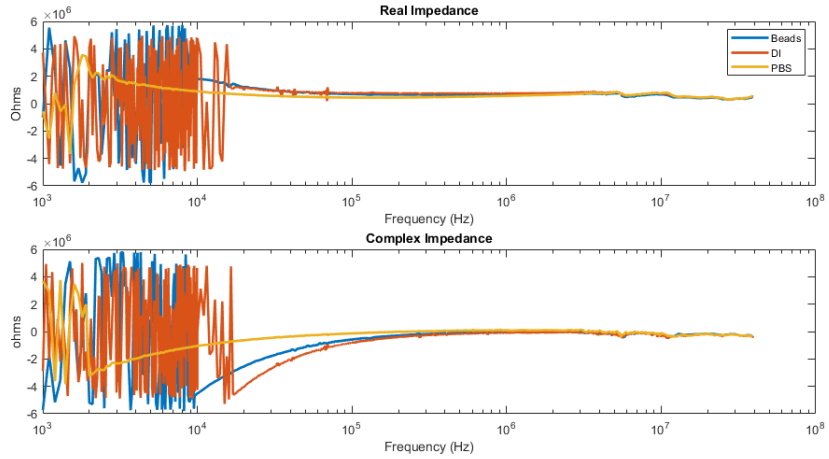

(b) Impedance spectroscopy results in rectangular form.

Figure 5.20: Comparison of impedance spectroscopy results using raw measurements of phosphate buffered solution, de-ionized water, and the chamber saturated with 7 μm polystyrene beads suspended in PBS.

The collected data met the expectations set by the material properties. Deionized water exhibited the largest impedance due to its high resistance, and the conductive PBS responded with a significantly lower impedance. By saturating the sensor chamber with PBS suspended polystyrene beads, the capacitive load significantly increased over PBS medium. However, as mentioned in the reproducibility

study, low-frequency-high impedance loads continued to be inconsistent.

To demonstrate how to isolate the effect of suspended suspended particles, the difference between the polystyrene bead suspension and the pbs solution was calculated. The results are depicted in the frequency domain of 10 kHz to 30 MHz are depicted in figure 5.21 with the applied correction function of equation 5.4.

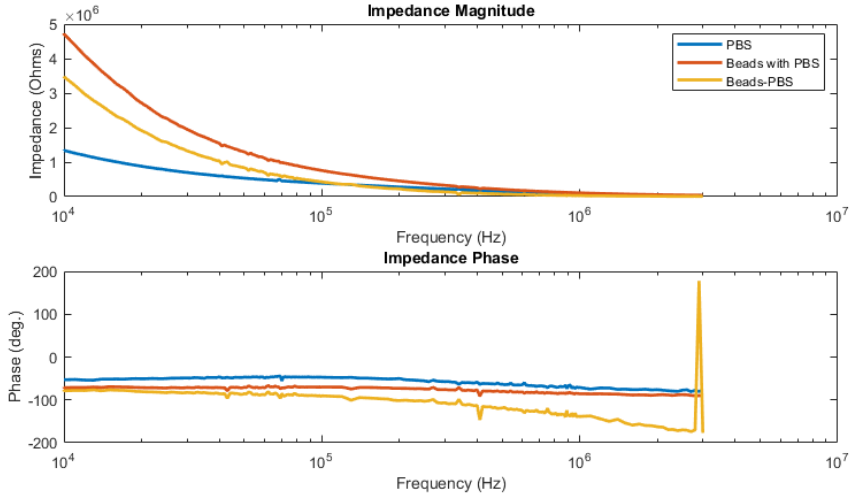

(a) IS results in polar form.

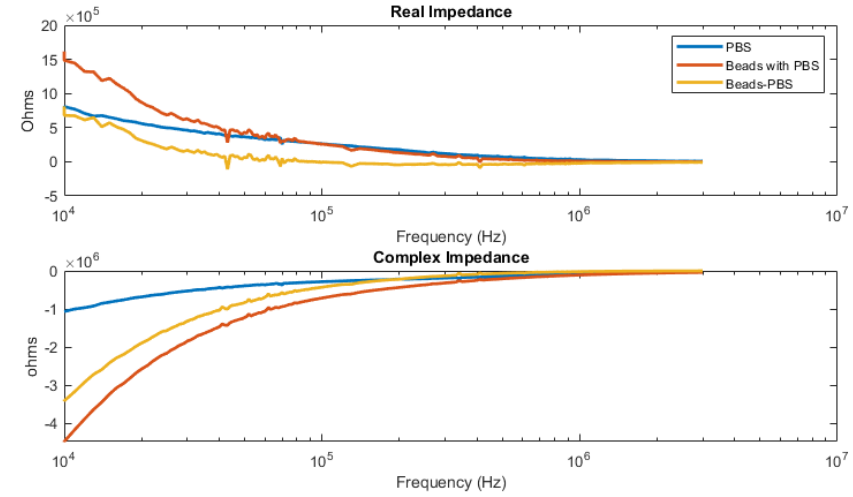

(b) IS results in rectangular form.

Figure 5.21: Comparison of impedance spectroscopy results from measurements of phosphate buffered solution, phosphate buffered solution saturated with 7 μm polystyrene beads, and the phasor difference between the two. The phase data was cleaned and the real and imaginary impedance was re-calculated.

5.3 Modeling

5.3.1 Impedance Spectroscopy Results

The impedance response for the analytic solution, the simple FEA model, and the device model were calculated for medium saturation and a single cell suspension. The analytic solution utilized the power volume fraction discussed in section 4.1.3. For details on the material properties used see table 4.1. Additional information on the analytic solution is available in section 2.3.1 and details on the FEA model are available in section 4.2.

The results for the medium impedance spectra are given in figure 5.22. The medium impedance spectra behaves as a bulk resistor and capacitor element in parallel with a single relaxation starting around 100 Mhz. In practice, an additional relaxation, governed by the polarization at the electrode-medium inteface (i.e. the EDL), would occur and largely mask the medium and cell relaxations. For these simulations the electric double layer phenomenon was excluded.

By comparing the three model results depicted in figure 5.22, it can be noted that the device model has a significantly smaller impedance response than the analytic solution and the simple FEA model. This difference can be attributed to geometry and will be further explored later in this section. In addition, the analytic and simple model spectra are nearly identical. This was expected since they model identical geometries.

With the inclusion of a single cell in the medium, the impedance spectra developed new dielectric dispersions. The simulated impedance spectra are depicted in figure 5.23. According to Pauly and Schwan, the addition of the single-shelled cell into the system is expected to add two new relaxations to the impedance spectra: the Maxwell-Wagner relaxation that occurs from the polarization of the cell membrane with the medium, and the relaxation from polarization of the cytoplasm and medium at high frequencies when the cell membrane capacitance has been short-circuited [30], [54]. The effect of the single cell is small, but can be readily identified

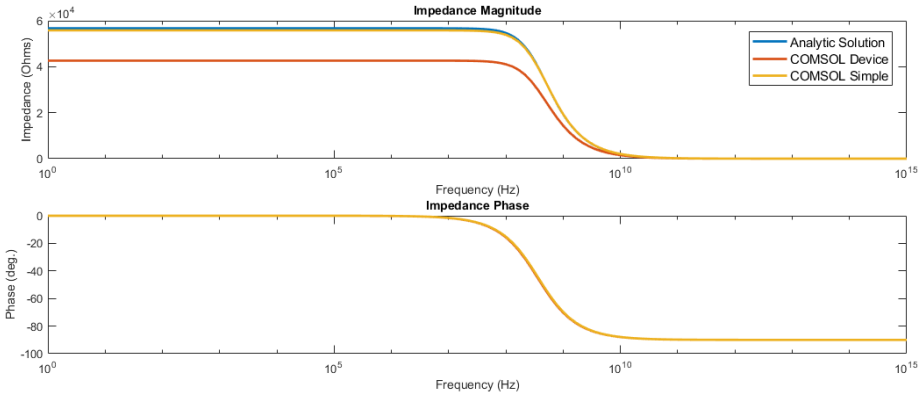

(a) Impedance spectra in polar form.

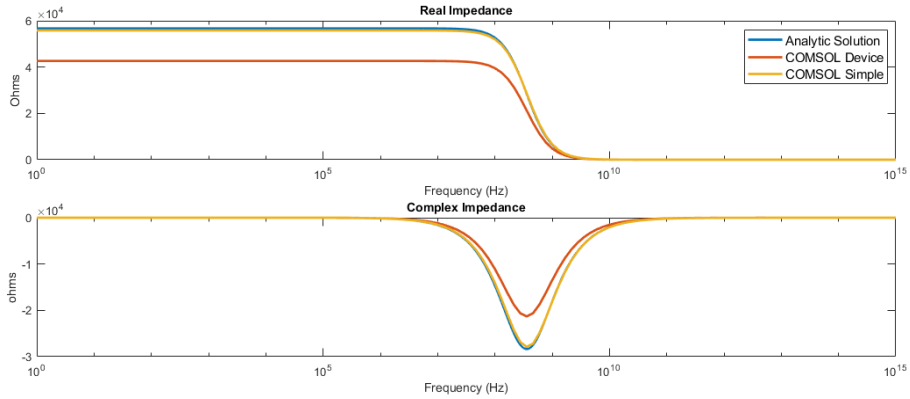

(b) Impedance spectra in rectangular form.

Figure 5.22: Medium impedance spectrum generated by the analytic impedance solution, the simple FEA model, and the device FEA model.

as a small relaxation starting around 10 Mhz. However, the two distinct relaxations of the single shelled cell can't be distinguished among the large relaxation of the medium. The small size of the characteristic single cell suspension in comparison to the medium impedance spectrum highlights the importance of sensitivity optimization. The device model, which features a smaller device sensitivity, generated data with a significantly smaller cell suspension relaxations.

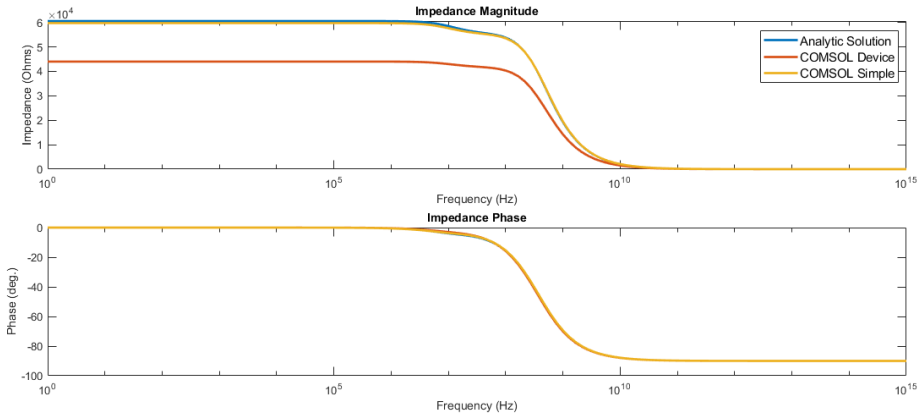

(a) Impedance spectra in polar form.

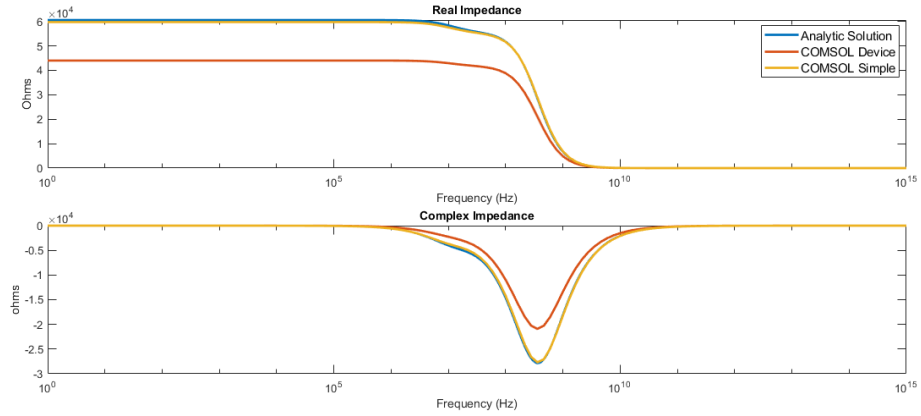

(b) Impedance spectra in rectangular form.

Figure 5.23: Single cell impedance spectrum generated by the analytic impedance solution, the simple FEA model, and the device FEA model.

To isolate the effect of the simulated cell, the difference between the single cell suspension and medium impedance spectra were generated and are displayed in figure 5.24. The spectra in figure 5.24 are ideal results that could be obtained from using two differential sets of electrodes, where one pair measures the single cell suspension, and the second identical pair measures a chamber of only medium. This is a powerful configuration for bypassing the overbearing presence of the electric double layer in the impedance data and to distinguish the effects of the single cell. With the effects of the cell isolated the two characteristic cell relaxations can be easily identified near 10 MHz and 100 MHz.

In addition to the differential spectra, figure 5.24 overlays the Clausius Mossotti factor. See section 2.2 for a description of the Clausius Mossotti factor. The onset

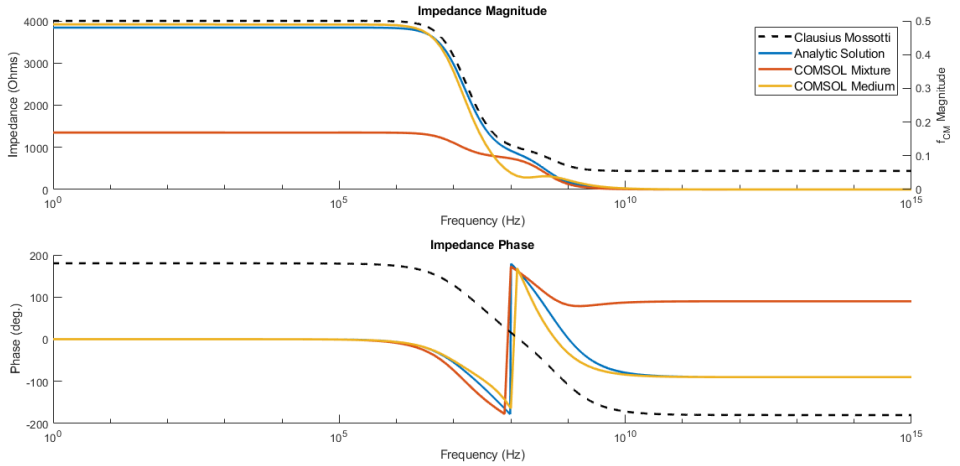

(a) Clausius Mossotti factor overlaid on difference impedance in polar form.

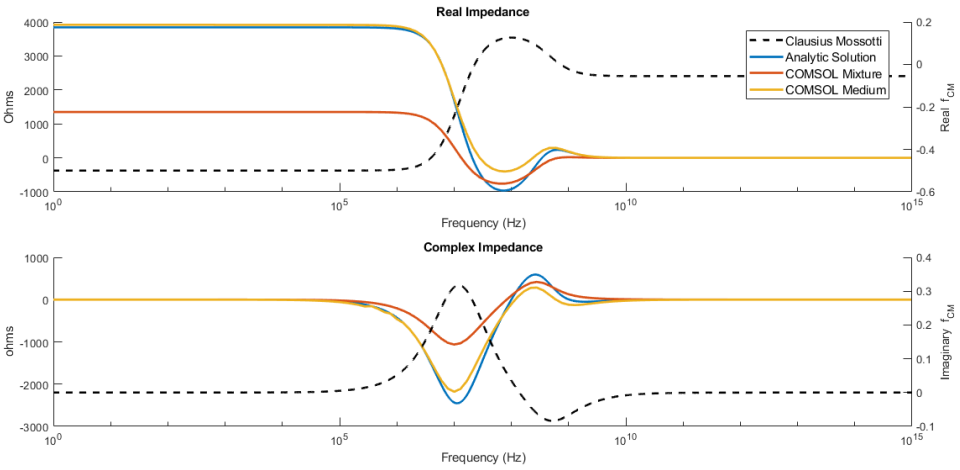

(b) Clausius Mossotti factor overlaid on difference impedance in rectangular form.

Figure 5.24: Clausius Mossotti factor overlaid on the phasor difference between mixture and medium impedance spectra model data generated from the analytic solution, the simple FEA model, and the device FEA model. The Clausius Mossotti factor overlay illustrates how the impedance responds to cell-medium polarization.

of local minima and maxima in the Clausius Mossotti factor predicts the frequencies of the dielectric dispersions, and can be used as a tool in system design and optimization. As demonstrated in figure 5.24a, the curvature of the Clausius Mossotti factor strongly correlates to the isolated particle impedance spectra as the Clausius Mossotti factor describes the polarizability of the particle with respect to the medium. This application is further discussed in section 5.3.2.

As similarly noted in the medium and mixture impedance spectra results, the difference device impedance is significantly less pronounced. In addition, there are

now discrepancies between the analytic solution and the simple FEA spectra. The differences begin to manifest at the onset of the Maxwell-Wagner relaxation at 10 MHz. Although the frequency positions of the dispersions coincide, the magnitude and shape of their spectra differ. This is most notable in the impedance magnitude chart in figure 5.24a. Since the analytic solution and the device model share the same shape, the simple model is suspected to contain errors. It is important to consider that the impedance difference spectra are a small fraction of the impedance of the medium and mixture models from which it is derived, and that errors can be compounded.

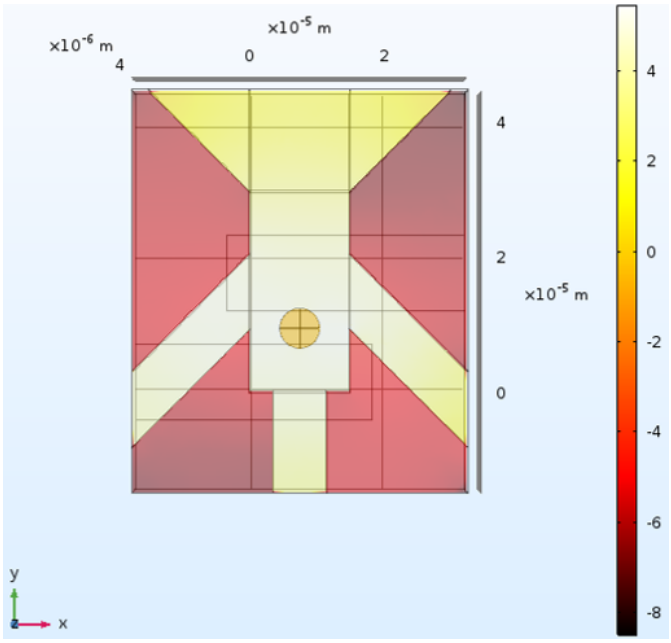

Figure 5.25: Current density plot of the FEA device model at DC. The color mapping depicts the logarithm of the current density magnitude.

Throughout the device model results, the device FEA model produced a smaller impedance than the analytic or simple FEA models. As depicted in figure 5.25, it can be seen that the overlap of a flush channel and an electrode opens up an additional current path. To measure the designed device inefficiency, a surface integration of current density over the electrode region overlapping with the flush channel was calculated. 27.53% and 29.29% of the system current flowed through the flush channel electrode region without and with a cell in the sensor region respectively. The side channel inefficiency will decrease the system cell constant and the effective volume

fraction with the net effect of decreasing the device sensitivity.

To aid in visualizing how the impedance spectra develops as a function of frequency, figure 5.26 plots the electric field lines and magnitude of the center cross-section of the FEA simple model.

At DC, the cell membrane is effectively non-conductive relative to the medium and the cell acts as an obstruction to current through the chamber.

With an applied frequency of 1 MHz there is evidence of applied signal frequency nearing the time constant of the membrane interface, but the electric field of the cell is only a fraction of the surrounding medium and the cell continues to largely obstruct current through the chamber. At 1 MHz the onset of Maxwell-Wagner relaxation is evident, but is far from dominating the spectra.

At 10 MHz, the effects of Maxwell-Wagner relaxation have fully developed. The cell membrane is effectively short-circuited and the effect of the cell is dominated by the dielectric properties of the cytoplasm. In this model, since the cytoplasm is more conductive than the medium, the isolated cell impedance is negative at 10 MHz, signifying that the cell is promoting current flow instead of impeding it.

With an applied frequency of 1 GHz the effect of the cell is negligible as the entire system is effectively short-circuited and current is unaffected by non-homogeneities of the dielectric.

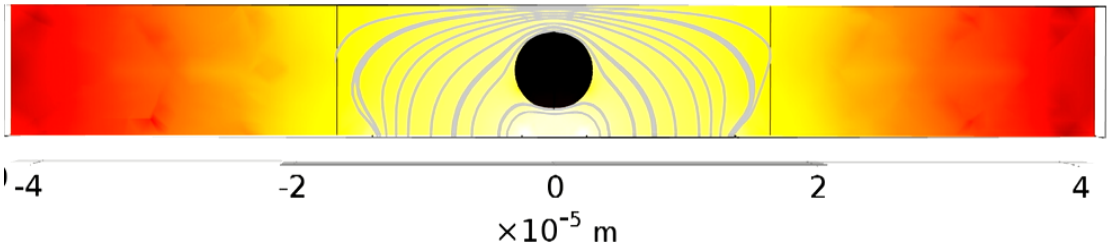

(a) The electric field at DC.

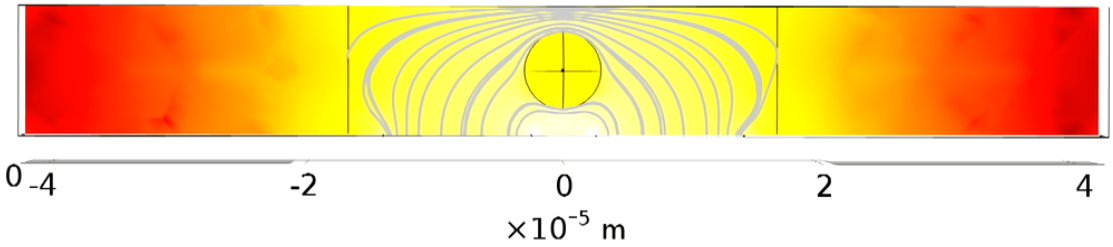

(b) The electric field at 1 Mhz.

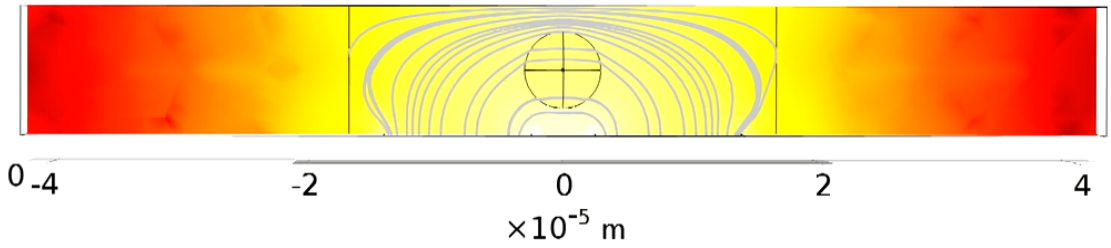

(c) The electric field at 10 Mhz.

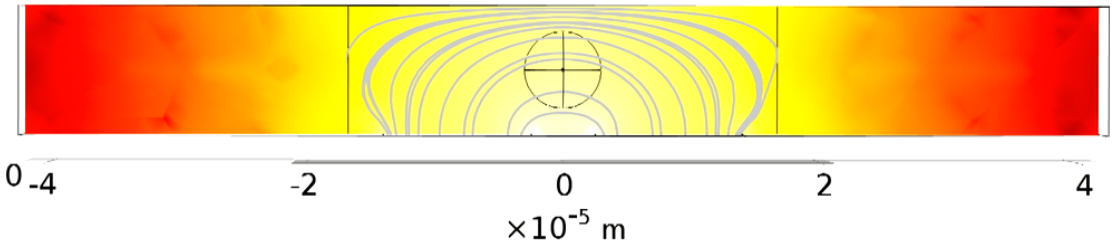

(d) The electric field at 1 GHz.

(e) The color map axis describing the magnitude of the electric field for the preceding sub-figures as $\log_{10}(V/m)$.

Figure 5.26: FEA simple model plots of the electric field at frequencies of interest. The logarithm of the electric field magnitude is depicted through the color mapping outlined by the color axis in sub-figure (e), and the electric field lines are illustrated with white curves in the region of the electrodes and cell.

5.3.2 Solution Optimization

As demonstrated in figure 5.24, the Clausius Mossotti factor can be used to determine at which frequencies dielectric dispersions occur. Measuring these dispersions is an important goal of single-cell impedance spectroscopy and provides significant insight about the cell under testing. As can be seen in equation 2.6, the Clausius Mossotti factor is largely driven by the dielectric properties of the medium and the particle. By tuning the properties of the medium, we can exercise some control over the frequency location of dielectric relaxations and optimize the solution for our IS system.

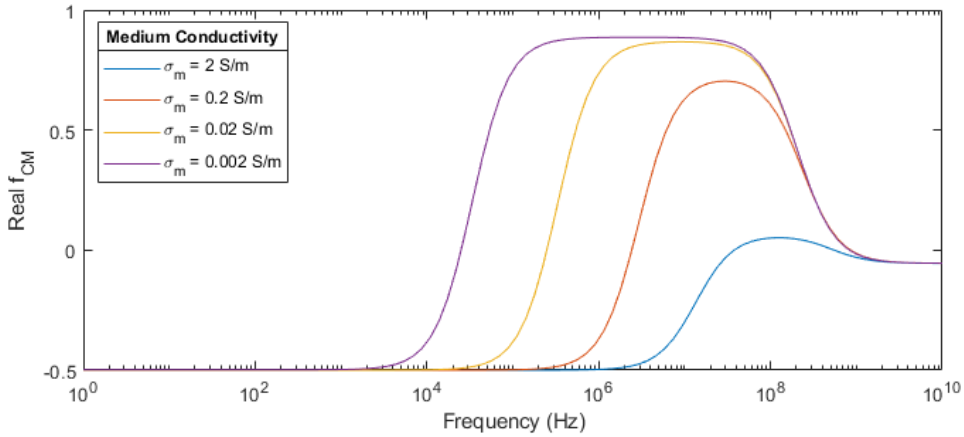

(a) The real part of the Clausius Mossotti factor.

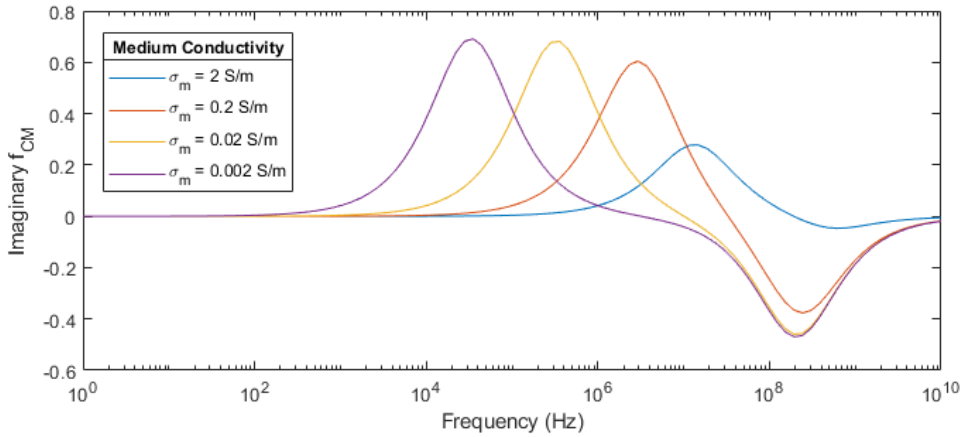

(b) The imaginary part of the Clausius Mossotti factor.

Figure 5.27: The Clausius Mossotti factor varied over several medium conductivity values. All other parameters are given in table 4.1

The effect on the Clausius Mossotti factor of altering the medium conductance

and permittivity are presented in figure 5.27 and 5.28 respectively. As demonstrated in figure 5.27, decreasing the conductivity of the medium shifts dielectric relaxations to lower frequencies. In contrast, figure 5.28 shows how the permittivity of the medium has little effect on the frequency of relaxations.

For application with the IS system of this thesis, the conductivity of the solution should be minimized as much as possible since our system has a high frequency limit of 40 MHz. It should be noted that there are significant limits to this approach. Hypotonic solutions can lead to cell swelling and death and small quantities of contaminates can severely increase the conductivity of DI water.

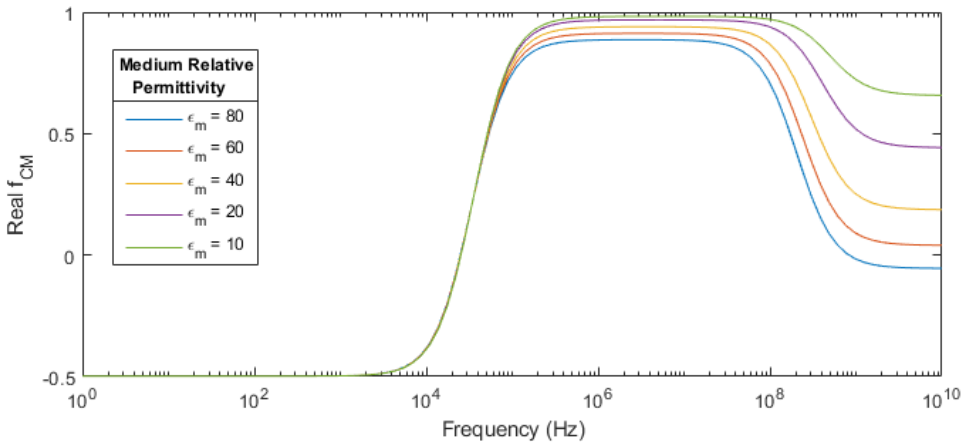

(a) The real part of the Clausius Mossotti factor.

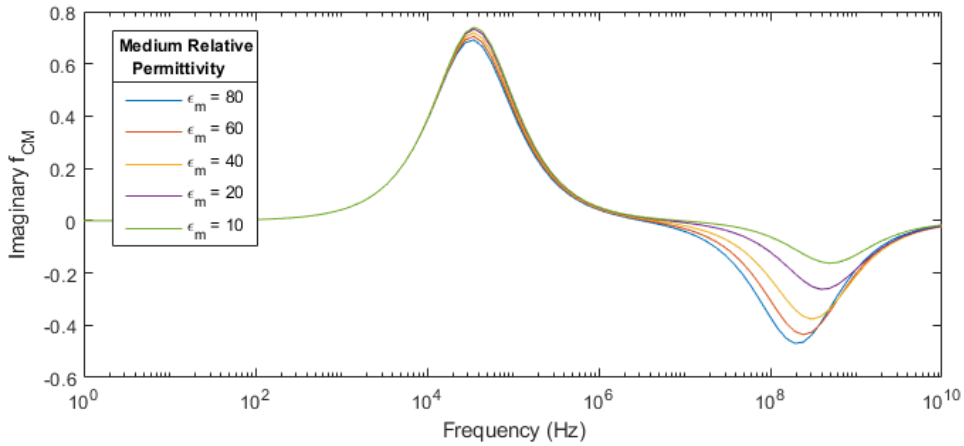

(b) The imaginary part of the Clausius Mossotti factor.

Figure 5.28: The Clausius Mossotti factor varied over several medium permittivity values. All other parameters are given in table 4.1

5.3.3 Optimization

FEA Sensitivity Curves

To optimize the geometry of the device, a parametric analysis based on the electrode gap and width were run on the simple and device FEA models at DC. For each model the electrode width and gap were varied from 5 μm to 15 μm and 1 μm to 10 μm respectively with 1 μm steps. All other geometry remained unchanged. Further details on the FEA models can be found in section 4.2.

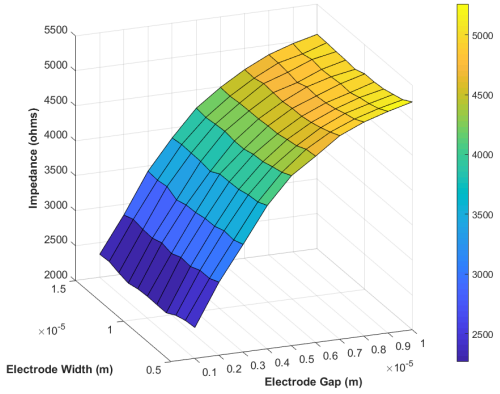

(a) Impedance difference curve.

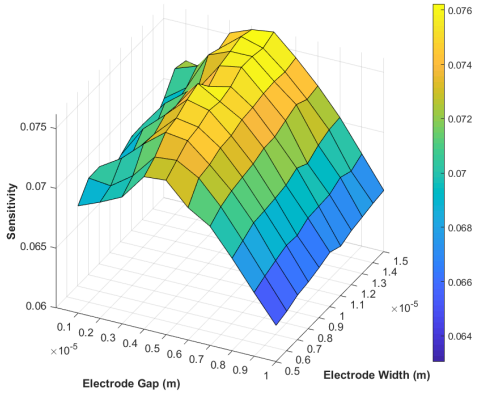

(b) Impedance sensitivity curve.

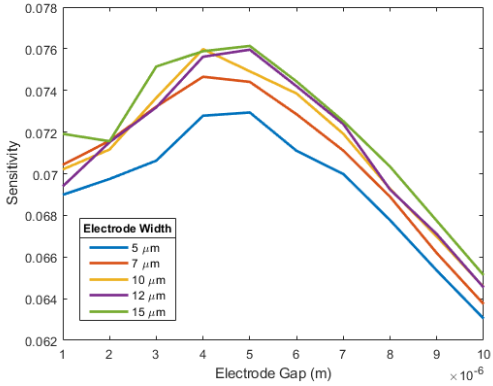

(c) Projection of the sensitivity curve onto the sensitivity - electrode gap plane.

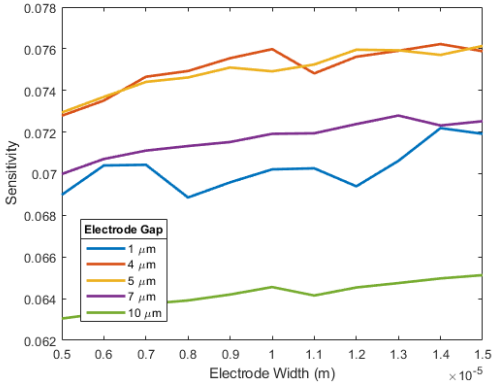

(d) Projection of the sensitivity curve onto the sensitivity - electrode width plane.

Figure 5.29: Parametric study on sensitivity using the Simple FEA model. The study varied the electrode width and gap from 5 μm to 15 μm and 1 μm to 10 μm respectively with 1 μm steps. The Simple FEA model held a channel height of 10 μm and a cell centered between the two electrodes with a center height of 5 μm. The sensitivity was calculated with equation 4.53. See section 4.2 for additional details on the Simple FEA model.

The parametric studies are presented as the difference between the medium and cell suspension impedance, the sensitivity as defined by Sun in equation 4.53, the sensitivity curve projected onto the sensitivity-electrode gap plane, and the sensitivity projected onto the sensitivity-electrode width plane. The parametric study of the simple and device FEA model are presented in figure 5.29 and 5.30 respectively.

The simple FEA parametric study identified a max sensitivity of 0.0762 with an electrode width of 14 μm and an electrode gap of 4 μm. The study found that the electrode gap had a large effect on sensitivity and formed an optimal electrode gap "ridge" around 4-5 μm on the sensitivity curve. The effect of the electrode width was small with slight increases in sensitivity with increased width.

The device FEA parametric study identified a max sensitivity of 0.059 with an electrode gap of 6 μm and an electrode width of 6 μm. However, as apparent in figure 5.30b, there is significant "noise" which is indicative of low precision results. Figure 5.30c and 5.30d depict the average trends over the electrode width and gap.

In both the device and, to a lesser extent, the simple FEA results, there is apparent "mesh noise". COMSOL generates a new mesh for each simulation in the parametric study. What is referred to as "mesh noise" is the accumulation of effects caused by the differences in meshes. Any mesh noise from the medium and mixture FEA studies are amplified through the calculations for sensitivity. The severity of "mesh noise" in the device FEA sensitivity is a clear signal that the meshing scheme needs to revisited.

To clarify and to expand upon the FEA parametric studies, the next section takes an analytic approach to sensitivity.

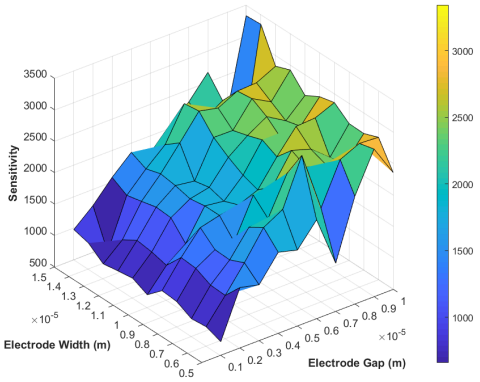

(a) Difference

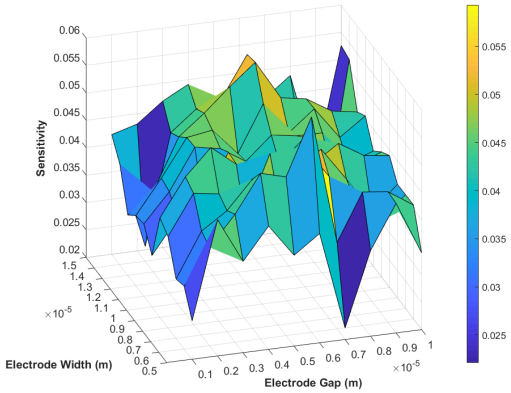

(b) Sensitivity

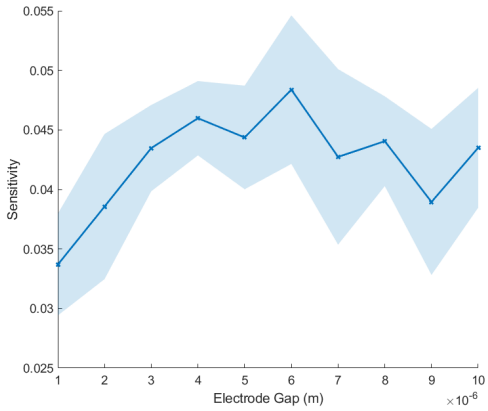

(c) The electrode width average of the sensitivity curve projected onto the sensitivity - electrode gap plane.

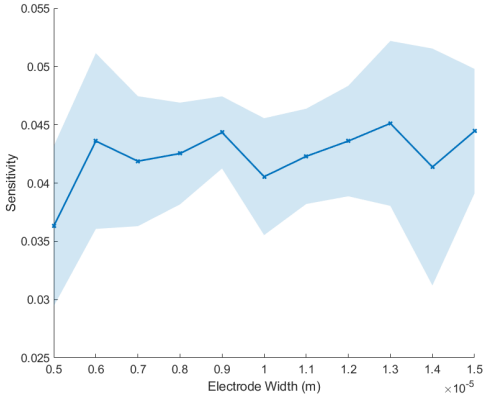

(d) The electrode gap average of the sensitivity curve projected onto the sensitivity - electrode width plane.

Figure 5.30: Parametric study on sensitivity using the device FEA model. The study varied the electrode width and gap from 5 μm to 15 μm and 1 μm to 10 μm respectively with 1 μm steps. The device FEA model held a channel height of 10 μm and a cell centered between the two electrodes with a center height of 5 μm. The sensitivity was calculated with equation 4.53. See section 4.2 for additional details on the device FEA model. In an attempt to identify trends through the mesh noise apparent in (b), the width and gap averages are presented in (c) and (d) respectively.

5.3.4 Analytic Solution Sensitivity Curves

Analytic methods for calculating the sensitivity of the impedance spectroscopy device were used to validate the FEA study, expand the parametric study, and to explore the effect of cell location on the sensitivity curves. There are three main advantages to using the analytic impedance solution for optimization over finite element methods:

1. significantly faster run time, allowing for far higher resolutions over far greater ranges.

2. General solution that isolates the effect of the electrode out from more complicated geometries.

3. No mesh noise. Parametric analysis does not bring in the effects of remeshing and effectively removes the effect of mesh artifacts from the simulation.

The analytic sensitivity was calculated with Sun's definition using the power fraction (equation 4.53 and 4.47), and the power fraction by itself (4.47).

Sun's sensitivity and the simple FEA sensitivity are compared in figure 5.31. Sun's method found a maximum sensitivity of 0.0684 at an electrode width and gap of 15 μm and 5 μm respectively, compared to the simple FEA maximum sensitivity of 0.0762 at an electrode width and gap of 14 μm and 4 μm respectively. The curves largely tracked each other except for electrode gap values less than 4 μm where the analytic sensitivity drops. This is where the maximum percent difference of 52.88% is recorded.

Since the power fraction does not share the same scale as Sun's method and the simple FEA sensivity, all three studies were normalized by their maximum and compared in figure 5.32. The maximum power fraction was found at an electrode width and gap of 15 μm and 5 μm. The mean absolute error between the power fraction vs. Sun's method, the power fraction vs. the simple FEA, and Sun's method

vs the simple FEA sensitivity curves are 0.0039, 0.0471, and 0.0486 respectively. This indicates that while the all three sensitivity studies track each other well, Sun's sensitivity and the power fraction clearly track each other the closest. This is supported by how all three studies predict nearly the same optimal electrode gap and width values inside the tested domain.

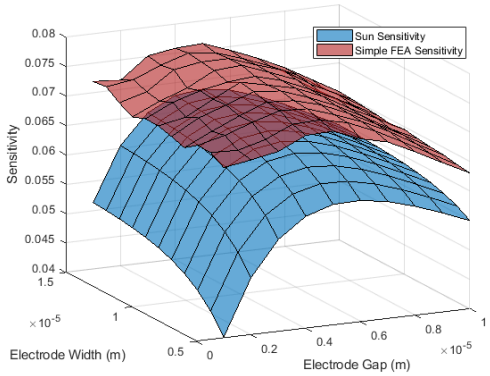

(a) Overlay of the Sun and Simple FEA sensitivity curves.

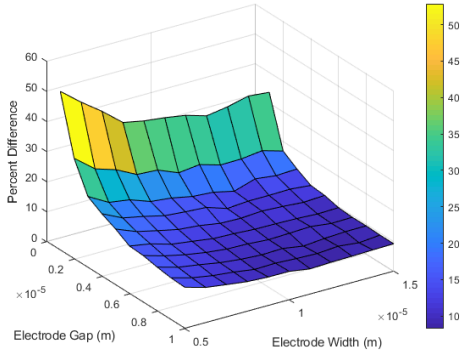

(b) Percent difference between the Sun and Simple FEA Sensitivity.

Figure 5.31: Comparison of Sun's Sensitivity calculated with the power fraction, and the simple FEA sensitivity. Sun's sensitivity found a maximum of 0.0684 at an electrode width and gap of 15 μm and 5 μm respectively. This is compared to the simple FEA maximum sensitivity of 0.0762 at an electrode width and gap of 14 μm and 4 μm respectively. The maximum percent difference is 52.88%.

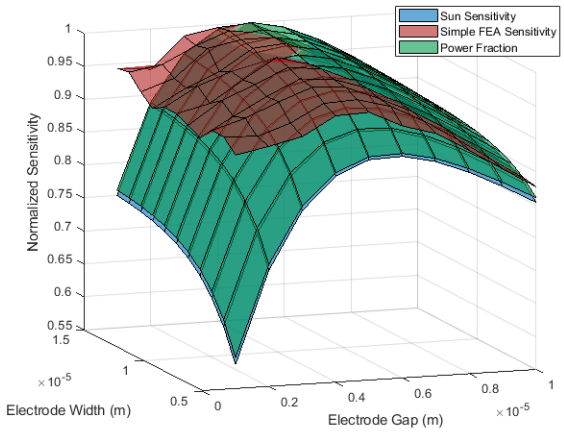

Figure 5.32: Comparison of power fraction, Sun's, and the simple FEA sensitivity curves normalized to their max sensitivity. The mean absolute error between the power fraction vs. Sun's method, the power fraction vs. the simple FEA, and Sun's method vs the simple FEA are 0.0039, 0.0471, and 0.0486 respectively.

The power fraction (equation 4.47) was used to calculate a high resolution sensitivity curve, perform a parametric study over an expanded domain, and to explore the effects of cell position on sensitivity.

The high resolution power fraction curve is depicted in figure 5.33. The study found a maximum power fraction of 0.0438 at an electrode width of 20 μm and an electrode gap of 4.8 μm to a precision of 0.1μm. The study was performed over an electrode length spanning 5 μm to 20 μm and the electrode gap spanning 1 μm to 10 μm.

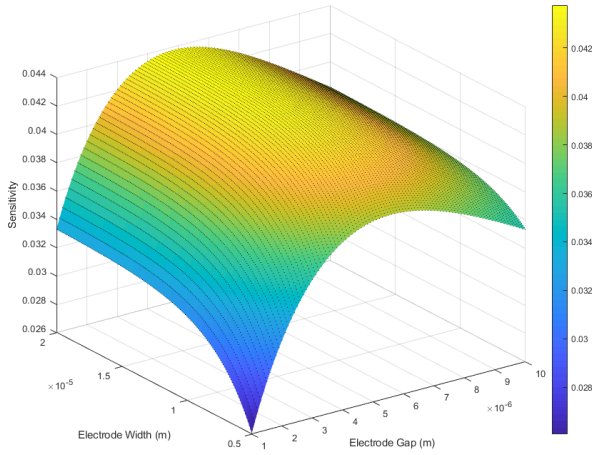

(a) High resolution power fraction curve.

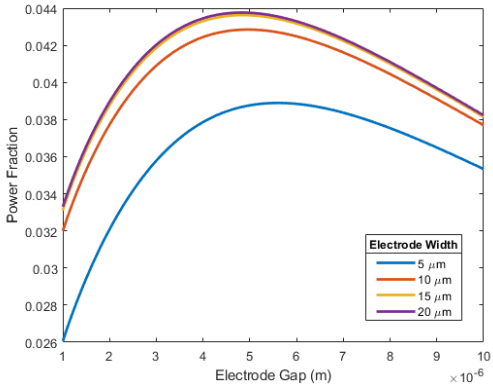

(b) Projection of the high resolution power fraction curve onto the power fraction - electrode gap plane.

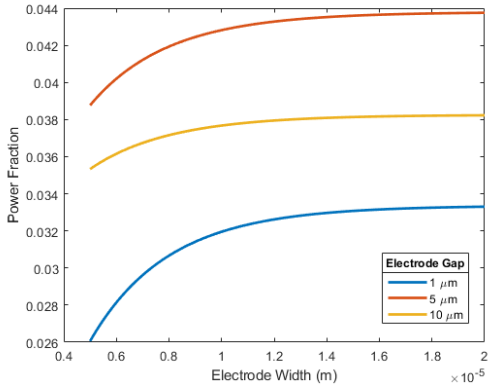

(c) Projection of the high resolution power fraction curve onto the power fraction - electrode width plane.

Figure 5.33: A high resolution power fraction curve calculated over the electrode width spanning 5 μm to 20 μm and the electrode gap spanning 1 μm to 10 μm. The curve has a resolution of 0.1 μm. The study found a maximum power fraction of 0.0438 at an electrode width 20 μm and a electrode gap of 4.8 μm.

The expanded sensitivity study calculated the electrode width and gap from 1 μm to 40 μm with a resolution of 0.5 μm and is presented in figure 5.34. The study found a maximum power fraction of 0.0438 with an electrode gap and width of 5 μm and 40 μm respectively.

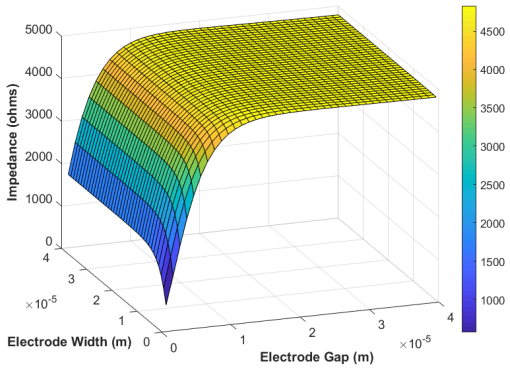

(a) The impedance difference between the single cell suspension and the medium.

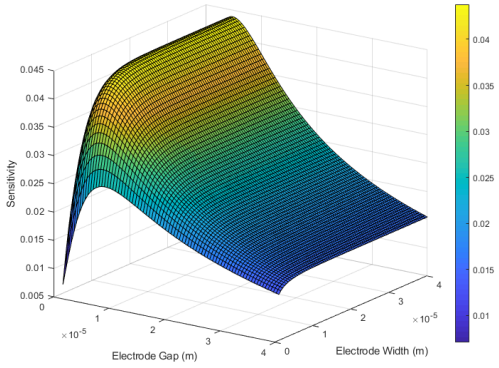

(b) The power fraction sensitivity curve.

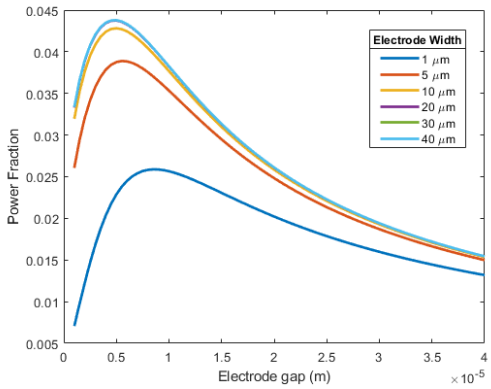

(c) Projection of the power fraction curve onto the power fraction - electrode gap plane.

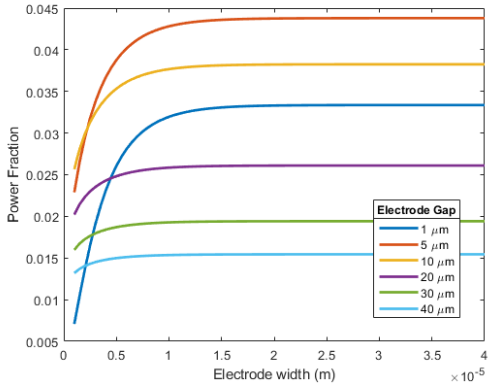

(d) Projection of the power fraction curve onto the power fraction - electrode width plane.

Figure 5.34: Expanded sensitivity study that varied the electrode width and gap from 1 μm to 40 μm with a resolution of 0.5 μm. The study found a maximum power fraction of 0.0438 with an electrode gap and width of 5 μm and 40 μm respectively. A 2.26% increase in power fraction was found by increasing the electrode width from 10 μm to 20 μm. A 0.091% increase in power fraction was found by increasing the electrode width from 20 μm to 40 μm.

The impedance difference between the mixture and medium is presented in figure 5.34a. The impedance difference maximizes and plateaus at a low electrode gap value. By increasing the electrode gap, power is distributed more evenly and progressively higher up in the center of the channel. Up to a certain point, this will

increase the power in the region of a cell suspended above the channel. At the same time, increasing the electrode gap increases the measured medium impedance. The balance of these trends leads to the characteristic "ridge" of the sensitivity curve which designates the optimized electrode geometry.

Increasing the electrode width over 10 μm found diminishing returns in optimizing the sensitivity. A 2.26% increase in power fraction was found by increasing the electrode gap from 10 μm to 20 μm. A 0.091% increase in power fraction was found by increasing the electrode gap from 20 μm to 40 μm.

The limiting effects of the electrode gap and width are strongly affected by the channel height. With a small channel height, larger electrode gaps and widths are restricted from producing power in regions far above the cell, instead the power is focused into the small region containing the cell.

The results presented in figure 5.35 studied the effects of cell position on the sensitivity curve. As expected and depicted in figure 5.35b, the power fraction is maximized for a cell centered between the electrodes. It should be noted that by sacrificing maximum sensitivity, increasing the electrode gap can increase the effective sensor zone of the device and decreases the variability within that zone.

Figure 5.35a tells a similar story. The sensitivity is maximized the closer the cell is to the plane of the electrodes. However, at the expense of sensitivity, the electrode gap can be increased to decrease the effect of cell height on the sensitivity. By increasing the electrode gap, the fringe effects of the electric field become smaller relative to the effective sensor zone and the power dissipation becomes increasingly homogeneous in the region between the electrodes.

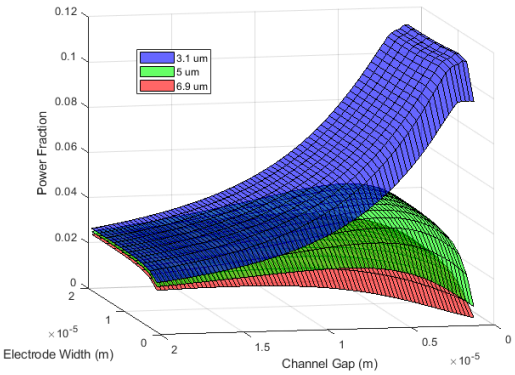

(a) Power fraction curves for several cell height positions centered over the electrodes.

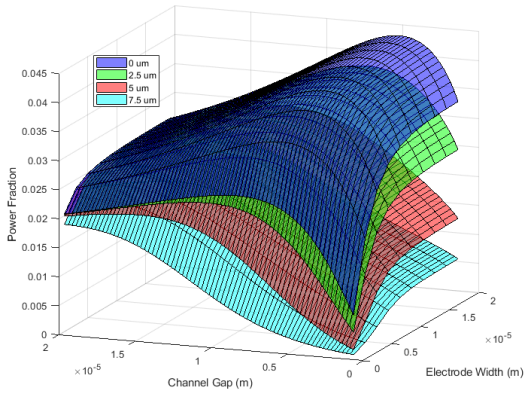

(b) Power fraction curves for several horizontal cell positions with the cell centered at a height of 5 μm.

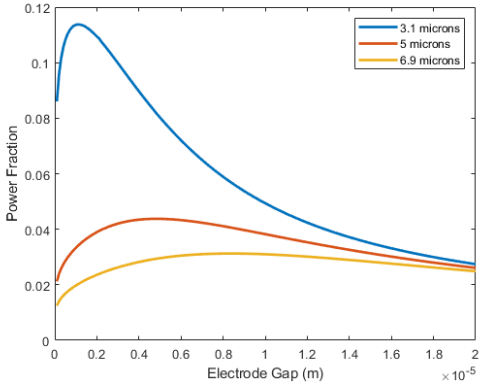

(c) Projection of power fraction curves for several cell height positions onto the power fraction - electrode gap plane. The electrode width is 20 μm.

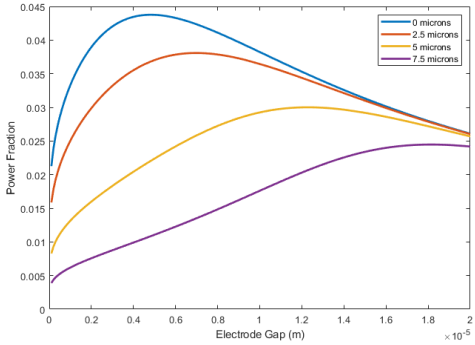

(d) Projection of power fraction curves for several horizontal cell positions onto the power fraction - electrode gap plane. The electrode width is 20 μm.

Figure 5.35: The effect of cell position on the power sensitivity curves. Graphs (c) and (d) are calculated with an electrode width of 20 μm.

Chapter 6: Discussion

Revisiting the thesis objectives set out in chapter 1, the purpose of this thesis is to re-evaluate and optimize the Cal Poly Biofluidic Lab's cell impedance spectroscopy system by exploring the following questions:

1. Are there aspects of the impedance spectroscope that need redesign or optimization?
2. Is the hardware implementation correct?
3. Can the correct circuit model and desired data acquisition and analysis be packaged and incorporated in a device interface computer program?
4. Can model based design be applied to characterize and optimize electric fields and impedance to inform future designs?
5. Can a device be manufactured at Cal Poly to validate the device design and analysis?

To investigate these questions, the following was accomplished throughout the scope the thesis:

- Fabrication of a micro-scale impedance spectroscopy chip in the Cal Poly Microfabrication lab.
- Design and implementation of a software interface to drive, measure, calculate, and compare impedance spectroscopy data in LabVIEW.
- Re-evaluation and validation of the impedance spectroscopy measurement circuit and requisite hardware.
- Evaluation of the impedance spectroscopy system by measuring impedance spectra of DI water, PBS, and a suspension of 7 μm polystyrene beads.

- Innovation of a novel volume fraction to fully account for cell geometry and fringe fields.
- Implementation of single-cell impedance spectroscopy models with numerical and analytic methods to investigate IS behaviour and optimization.
- Development of a graphical user interface for the analytic impedance solution to aid in model-based design.

To answer our guiding questions listed above, the findings from the aforementioned works are discussed and recommendations for future work are made.

6.1 Micro-fabrication

A fully-functional impedance spectroscopy chip was fabricated in the Cal Poly microfabrication lab. The microfluidic channels of the previous generation of the Biofluidic Lab's impedance spectroscopy chip was fabricated at Cal Poly, but the manufacturing of the micro-electrodes were outsourced to the UC Santa Barbara microfabrication lab. In this thesis, in addition to recreating the PDMS microfluidic channels, a process for micro-electrode fabrication was developed and demonstrated the capability to fabricate the complete impedance spectroscopy chip at Cal Poly.

Future Work for Device Manufacturing

Although a complete BioMEMS impedance spectroscopy chip was successfully fabricated at Cal Poly, there is significant room for improvement to increase reliability and to decrease the scrap rate. There is a need for an alignment device to align the PDMS and the electrodes during glass bonding. The current solution is to align the device components by hand while observing the sensor region under a microscope. Making this alignment by hand is difficult and nearly impossible without adding ethanol to act as lubricant to provide about 10 minutes before bonding. It is possible that the rough process of hand alignment is responsible for some of the

particulate generation that eventually led to the jamming and delamination of the IS chip.

This thesis demonstrated the ability to create microelectrodes at the Cal Poly microfabrication lab; however, the process is fraught with risks that can destroy the electrodes and has a very high scrap rate. A huge improvement in the electrode manufacturing process could be realized by utilizing a dual target sputtering tool. Such a tool could allow the deposition of chromium and gold while keeping the substrate under vacuum. This is expected to prevent the formation of chromium oxide before the deposition of gold and significantly increase its adhesion.

6.2 IS Software

To drive, measure, and calculate impedance spectroscopy experiments, a software interface was programmed in LabVIEW. The software is capable of making measurement from an I-V or auto-balancing bridge circuit; performing single IS experiments or timed IS runs at intervals of seconds to days; and features the the ability to compare previously recorded experiments. However, for the application of continuous IS measurements on the scale required for flow-through devices, there are significant updates required.

Future Work

If a flow-through impedance spectroscopy is developed, techniques to measure the broadband impedance spectra quickly as cells flow through the sensor region must be implemented. The currently implemented NI PXI-5421 function generator can output arbitrary waveforms that can be programmed to apply a broadband signal and the frequency response can be analyzed with the Fast Fourier Transform, but the power distribution of the broadband signal, the short measurement time, and noise complicates the practical implementation. Several solutions to this problem have been proposed and include applications of chirp waveforms and maximum length sequences. [55]–[57].

The current implementation of the IS software is built with the ability to incorporate new modules to allow for future features to be added to the program without affecting existing functions. These additions can be made by adding new states or state flows to the program. However, a large draw back to the current architecture is its limited ability of concurrency. If the need arises to make significant changes to the IS software, it is recommended to consider the implementation of a queued message handler architecture (QMH). The QMH architecture encourages parallel programming while also fortifying low-coupling practices with code modules that can co-exist and execute independently. It allows for a more responsive, faster, extendable, and maintainable program. Although likely overkill for this application, the object-oriented analogue to QMH, the ACTOR framework can also be considered. The actor framework ships standard with LabVIEW and its implementation can build a powerful architecture for medium to large applications.

6.3 Impedance Measurement Hardware

The impedance spectroscopy I-V measurement circuit was validated against a test circuit and a large portion of the reported error was quantified and used to improve upon the IS DAQ system.

The measurement circuit was validated against a test circuit and its simulated response. The first limitation realized by evaluating the previous version of the IS hardware, is that the use of coaxial cables incurs significant errors and should be avoided in the current configuration. If coaxial cables are properly implemented, they are exceptional for radio frequency (RF) signal transmission featuring low loss, shielding to noise, and reduced RF emissions. However, when implemented with the I-V circuit described in this thesis, they are a source of significant error. Referring to figure 3.23, if a coaxial cable is used to connect scope ch.1 to between the DUT and the external resistor, the characteristic capacitance of the coaxial cable would draw a significant amount of current through its shielding into ground and grossly invalidate the assumption that all current flowing through the DUT also

flows through the external resistor. In addition, this implementation of the I-V circuit requires that the oscilloscopes are set to their high impedance settings rather than the 50 Ohm input used for avoiding reflectance with coaxial cable. However, if the auto-balancing bridge method is utilized, the benefits of coaxial cable can be obtained while the measurement circuit is protected from extra current draw by an operational amplifier, or equivalent, that maintains a virtual ground after the DUT. The current implementation utilizes insulated solid core wire while minimizing wire length to decrease noise susceptibility.

After the implementation of solid core wire, the effect of the oscilloscope on the recorded impedance was measured and quantified. Similar to the error caused by the coaxial cable, the current that leaks through the oscilloscope will artificially inflate the measured impedance. Errors were measured that reached over 10,000%. This error was quantified as a factor of the external resistor and the effective external impedance and used to develop a correction factor. After application of the correction factor described in equation 5.2, errors were reduced to under 30% over the range of 3 kHz to 25 MHz.

Future Work

All recorded IS datasets feature low-frequency noise that abates near 3 kHZ to 10 kHZ. This noise could be from small voltage signals approaching the noise floor, or the resolution limit of the oscilloscope. The cause of this noise was not pursued and is a shortcoming of the current IS measurement system that should be explored in future iterations.

Beyond the low-frequency noise, the broadband error can be further reduced by replacing breadboards for alternative connections that are less prone to parasitic capacitance, the implementation of high impedance FET oscilloscope probes, or the application of an autobalancing-bridge circuit. Practical auto-balancing bridge circuits can be complicated to implement accurately for broadband signals, but some have had success creating digital auto-balancing circuit systems [58].

For the current implementation, insulated solid core wire was connected to the impedance spectroscopy chip, and the length of the wire was minimized to reduce noise. A breadboard was used for making and organizing connections. Although no differences were noticed between data measured with and without the the use of a breadboard, future implementations should move away from using a breadboard due do its inherent capacitance.

6.4 IS System Evaluation

The complete IS system was evaluated on the basis of repeatability and qualitative accuracy through the comparison of measured impedance spectra of DI water, PBS, and 6μm polystyrene beads suspended in PBS. Due to debris flow that ultimately clogged the device, the evaluation was made on a limited body of data. However, the results were consistent and appeared sufficient to draw conclusions on the system's performance.

To assess the reproducibility of the IS system, impedance spectra of PBS measured over three consecutive days were compared. The data clearly showed that experiment could be reproduced over the broadband range of 10 kHz to 40 MHZ. However, the low frequency noise observed in the measurement hardware validation also occurred in IS chip measurements and caused high variability. Hypotheses on the source of this noise are discussed in 6.3.

The accuracy was qualitatively assessed by comparing the relative impedance spectra of DI water, PBS, and a 6μm polystyrene bead suspension in PBS. The impedance spectra met the expectations set by the dielectric properties of the solutions. Deionized water exhibited the largest impedance due to its high resistance and the conductive PBS responded with significantly lower impedance. By saturating the sensor chamber with PBS suspended polystyrene beads, the capacitive impedance significantly increased over the PBS medium.

Future Work

Although experiments largely appeared promising and demonstrated a functioning impedance spectroscopy device, there is future work required to bring a more robust device on-line. First and foremost the manufacturing process should be revisited and refined with an emphasis on particulate reduction. Particles on the order of 10 μm will significantly reduce the life-span of the device.

The investment in higher resolution photolithography masks will likely be required to manufacture single-cell impedance spectroscopy cell-capture devices. Alternatively, a flow-through device will be easier to fabricate with lower resolution masks. However, flow-through devices will require additional changes to the software and data post-processing if broadband frequencies need to be explored. Furthermore, the addition of a second set of electrodes to make differential measurements should be considered. The dual sets of electrodes will allow for real-time subtraction of the medium and EDL from the impedance spectra to isolate the effect of the cell. Alternatively, particle spectra isolation can be calculated from a single set of electrodes by comparing the individually captured particle suspension spectra to the medium spectra as depicted in figure 5.24, however, this method runs the risk that the medium properties have changed between experiments.

6.5 Impedance Spectroscopy Modeling

To investigate and optimize the single cell impedance spectroscopy system, analytic and finite element models were developed.

By following the work of Sun [31], an analytic solution of co-planar electrodes was developed through application of Maxwell's Mixture Theorem and conformal mapping. Part of this solution required the use of the volume fraction. Previously used volume fractions were calculated as the ratio of the cell volume to the volume over the electrodes, however, this method neglects the position of the cell and the non-uniformity of the electric field. This thesis addressed the problem by develop-

ing effective volume fractions based on conformal mapped volumes and dissipated power. These methods increased the accuracy of the analytic impedance solution and allowed for the quantification of the effect of the cell position.

The analytic solution and the finite element model largely agreed with each other with percent errors reaching as low as 0.01%. The finite element model further explored the effect of the device geometry and found that over 29% of the electric current leaked through the overlap of the electrodes and flush channel. This current leak significantly decreases the device sensitivity.

In section 5.3.3 device optimization was explored. With the ability to simulate the effect of position with novel effective volume fraction methods, it became obvious that there were two opposing qualities to optimize: the maximum sensitivity given a particle location and size, and the maximum sensitivity given a desired volume of uniform sensitivity. In both cases, the optimal geometry was highly dependent on the application. It was concluded that there is not optimal geometry for all scenarios. However, several trends were found that are critical for device design.

Given an electrode height of 10 μm, small to negligible gains in sensitivity were found with increased electrode width. This is an important finding of the optimization studies. Although the sensitivity benefits are meager, wider electrodes are far easier to manufacture and are more resilient to cracks and defects. The modest effect of increased sensitivity is explained by opening additional parallel current paths with wider electrodes and, in effect, increasing the dissipated power in the region of the particle. However, if the particle is near the base of the sensor chamber and is small compared to the chamber height, increasing the electrode width will decrease the sensitivity since the majority of the additional dissipated power occurs above the particle.

Since the electric double layer (EDL) can be modeled as a largely capacitive distributed impedance over the electrode surface, it may be tempting to conclude that by increasing the the width of electrodes, the impedance load of the EDL is reduced. And while that is true, the effect rapidly diminishes. In general for a given channel

height, additional electrode area distal to the sensor chamber center contributes less current than electrode area near to the sensor chamber. Likewise, the EDL on distal electrode areas contributes less capacitance to the system impedance. This can be visualized by revisiting our ideal capacitor model in the W-plane (2.18). For each additional increase in electrode width, γ becomes larger compared to δ, but each additional increase in electrode width contributes progressively less to γ.

The effect of channel height on sensitivity matched intuition. Smaller channel heights increase sensitivity in all scenarios by restricting parallel currents outside of the particle region and by focusing the particle to higher power regions. In addition, short channel heights enable wider electrodes. With increased channel heights, the distal portions of wider electrodes will contribute more current to the higher regions of the chamber and effectively reduce the sensitivity. With target particles of 6μm in diameter, a chamber height of 10μm in our current device is near optimal. Although the sensitivity of the device could dramatically be increased with decreased channel height, it comes with the increased risk of clogs from particles and debris.

Optimizing the electrode gap to maximize the device sensitivity is highly dependent on the cell size, cell location, and channel height. The optimization for a 6μm diameter cell centered in the sensor chamber with a channel heighth of 10 μm is found at an electrode gap of about 5 μm, which is the electrode gap of our current device design. However, if the cell deviates from this position, the sensitivity will rapidly diminish. If an accurate method of cell-capture is employed, this highly spatially-dependent sensitivity may be acceptable. However, for cell-capture devices where the cell position cannot be guaranteed or for flow-through devices, a large region of uniform power dissipation is desired. A uniform power region can be accomplished by increasing the electrode gap, but at the cost of high sensitivity. This could be useful for increasing the device resident time in flow-through devices.

Future Work

In both the analytic and the finite element models the electric double layer is neglected, but, the electric double can easily shroud the effect of a single particle. Although techniques have been mentioned in this thesis to isolate the effect of the particle from the EDL, the development of an accurate EDL model would be useful for device validation and experiment interpretation. Current analytic models are largely inaccurate, but electrodes can be characterized by fitting experimental data to empirical models.

6.6 A Framework for Single-Cell IS Model-Based Design

As previously discussed, there is no optional design for all cases. To that end, a model-based design framework using the simulations and tools developed in this thesis is presented. The IS app presented in chapter 4 contains most of the tools required for design calculations in the following steps.

1. Identify Functional Requirements and Material Properties

   Prior to device design or fabrication, the functional requirements of the device and the relevant material properties should be identified. This information should include the device type (i.e. flow-through or cell-capture), the cell type, the literature values of the cell's dielectric properties, the average and variance of the cell size, the plausible cell mediums, and the dielectric properties of those mediums.

2. Determine Required Frequency Range

   The required frequency range of the impedance spectroscopy system should be determined by the functional requirements identified in step 1. Cell counting or cell size can be determined with a DC or low-frequency applied signal. However, if information regarding the cell membrane or internals is required, a broadband frequency range will be required. A useful tool to determine the

required frequency range is the Clausius Mossotti factor. By using the literature values of the dielectric properties of the cell and medium to be measured, theoretical values of the suspensions dielectric relaxations can be identified and used to inform a required frequency range.

3. Model and Optimize Simple Device Design

   The purpose of this step is to use the analytic IS solution for co-planar electrodes to inform initial design and electrode optimization. If the cell will be focused to a specific height, the electrodes can be optimized to the maximum sensitivity, but if the resident time needs to be increased, the electrodes can be optimized to create a region of uniform power density at the cost of maximum sensitivity. If the fluid dynamics requires a channel geometry that differs significantly from the simple model, a FEA simulation can quantify the device impedance and sensitivity. However, it is still recommended to optimize the system with the analytic model as mesh changes throughout a parametric analysis can introduce “mesh noise” into the optimization curve. Once the general sensor region design is determined, an estimate of the impedance load of the system should be calculated (including an estimate of the EDL).

4. Design Impedance Spectroscopy Measurement Hardware

   With an estimate of the required frequency range, the impedance load, and the device type, the impedance measurement system can be selected or designed. For measurement circuits, this thesis focused on the simplest I-V circuit and discussed the auto-balancing bridge method, but there are other methods that range in complexity and are appropriate for different frequency and impedance loads. See section 2.2.3 for a short discussion of I-V and auto-balancing circuits and "A Guide to Measurement Technologies and Techniques" by Keysight Technologies for a more in-depth discussion of a wider range of measurement circuits [32]. The ability of the signal generator should be determined by the required frequency range and the type of the device.

Depending on the type of the measurement circuit and impedance load, close attention should be made to the input impedance of the oscilloscope or the ADC and how this will affect measurement readings.

Chapter 7: Conclusion

This thesis implemented a bioelectric impedance spectroscopy system and developed a model to inform design and aid in the interpretation of single-cell impedance spectroscopy.

To implement the impedance spectroscopy system, an impedance spectroscopy bioMEMS chip was fabricated in the Cal Poly Microfabcrication lab, software was developed to run impedance spectroscopy experiments, and impedance spectroscopy experiments were run to validate the system.

To develop the single-cell impedance spectroscopy model, Maxwell's mixture theorem and the Schwartz-Christoffel transform were used to calculate an analytic impedance solution to the co-planar electrode system, a novel volume fraction to account for the non-uniformity of the electric field was developed to increase the accuracy of the analytic solution and to investigate the effect of cell position on the impedance spectrum, a software program was created to allow easy access to the analytic solution, and FEA models were developed to compare to the analytic solution and to investigate the effect of complex device geometry. This model was used to explore device optimization and to develop a model-based design framework.

This thesis found that the Cal Poly Biofluidics Lab's impedance spectroscopy system is a viable system to make cell measurements. With improvements to the IS measurement system and new IS chips guided by model-based design, this system can make repeatable, accurate, and meaningful single-cell impedance measurements.

Appendices

Chapter A: Microfluidics

In most BioMEMS there is fluid flow on the micrometer scale. At this scale fluid flow physics differ from fluid flow at the macro scale. Understanding and leveraging microfluidic mechanics allows for small reagent and sample volumes, multiplexing, and physic phenomenon that allow experiments and functions not possible at the macro scale. Laminar flow, diffusion, fluidic resistance, surface area to volume, and surface tension, may not be dominant in phenomenon on the macro scale, but on the micro scale become significant [41].

A.1 The Navier-Stokes Equation

The Navier-Stokes formula is a partial differential equation that describes the fluid velocity given a set of boundary conditions. The Navier-Stokes equation is derived from applying Newton's second law to an infinitesimally small arbitrary control volume:

$$\rho \frac{\mathrm{D}\mathbf{u}}{\mathrm{D}t} = \sum \mathbf{f}, \tag{A.1}$$

where ρ is the mass density, **u** is the velocity vector, $\sum \mathbf{f}$ is the sum of forces applied to the control volume, and $\frac{\mathrm{D}()}{\mathrm{D}t}$ is the material derivative [59]. The material derivative is the time derivative of a function that is spatially dependent and arises from the chain rule. The material derivative of an arbitrary spatial and temporal function ($F = F(t, x, y, z)$) can be calculated as

$$\frac{\mathrm{D}F}{\mathrm{D}t} = \frac{dF}{dt} + \frac{dF}{dx}\frac{dx}{dt} + \frac{dF}{dy}\frac{dy}{dt} + \frac{dF}{dz}\frac{dz}{dt}, \tag{A.2}$$

and can be expressed as

$$\frac{\mathrm{D}F}{\mathrm{D}t} = \frac{dF}{dt} + \mathbf{v} \cdot \boldsymbol{\nabla} F, \tag{A.3}$$

or in index notation as

$$\frac{\mathrm{D}F}{\mathrm{D}t} = \frac{dF}{dt} + v_j \frac{dF}{dx_j}. \tag{A.4}$$

The material derivative is valid for scalars and vectors.

Surface forces are present in many fluid systems and generally arise from pressure driven flow and viscous properties of the fluid. In general, the surface forces are expressed as the divergence of the stress tensor:

$$\mathbf{f}_s = \boldsymbol{\nabla} \cdot \mathcal{T}, \tag{A.5}$$

$$\mathbf{f}_s = \frac{d\tau_{ij}}{dx_i}, \tag{A.6}$$

where $\mathbf{f}_s$ is the surface force, and $\mathcal{T}$ and τ_{ij} are the second order stress tensor which is dependent on the type of fluid and the driving forces. For pressure driven inviscid fluids, the stress tensor and surface forces can be expressed as

$$\tau_{ij} = -p\delta_{ij}, \tag{A.7}$$

$$\mathbf{f}_s = -\frac{dp}{dx_j}, \tag{A.8}$$

where p is the pressure.

For a viscid Newtonian fluid, the stress tensor and surface force can be expressed as [59]

$$\tau_{ij} = -p\delta_{ij} + 2\mu(\epsilon_{ij} - \frac{1}{3}\epsilon_{kk}\delta_{ij}), \tag{A.9}$$

$$\mathbf{f}_s = \frac{dp}{dx_i} + \mu\frac{d}{dx_j}(\frac{du_i}{dx_j} + \frac{du_j}{dx_i} - \frac{2}{3}\delta_{ij}\frac{du_k}{dx_k}), \tag{A.10}$$

where ϵ_{ij} is the rate of strain tensor written as

$$\epsilon_{ij} = \frac{1}{2}\Big(\frac{du_i}{dx_j} + \frac{du_j}{dx_i}\Big). \tag{A.11}$$

If the fluid is incompressible, then conservation of mass states

$$\frac{du_k}{dx_k} = \boldsymbol{\nabla} \cdot \mathbf{u} = 0, \tag{A.12}$$

and equation A.10 can be simplified to

$$\mathbf{f}_s = -\frac{dp}{dx_i} + \mu \frac{d^2 u_i}{dx_j^2} \tag{A.13}$$

$$\mathbf{f}_s = -\boldsymbol{\nabla} p + \mu \boldsymbol{\nabla}^2 \mathbf{u} \tag{A.14}$$

Additional common forces on the control volume can include the gravitational force

$$\mathbf{f}_g = \rho \mathbf{g}, \tag{A.15}$$

where **g** is the acceleration of gravity, and for some microfluidic applications, the electroosmotic flow force (EOF)

$$\mathbf{f}_{EOF} = -\rho_e \boldsymbol{E}, \tag{A.16}$$

where $\boldsymbol{E}$ is the electric field vector, and ρ_e is the net charge density of the electric double layer (EDL). Electric osmotic flow arises from the Coulomb force caused by the net electric charge from the electric double layer at the channel surface and the applied electric field. The electric double layer arises from the equilibrium of the solid-fluid interface [20]. EOF results in plug flow which is characterized by a flat velocity profile in contrast to a parabolic velocity profile in pressure driven flow (figure A.1).

The most common form of the Navier-Stokes equation includes the surface forces of pressure driven Newtonian fluids with the gravitational forces, and can be expressed by combining equations A.1, A.14, and A.15.

$$\rho(\frac{d\mathbf{u}}{dt} + \mathbf{u} \cdot \boldsymbol{\nabla} \mathbf{u}) = -\boldsymbol{\nabla} p + \mu \boldsymbol{\nabla}^2 \mathbf{u} + \rho \mathbf{g} \tag{A.17}$$

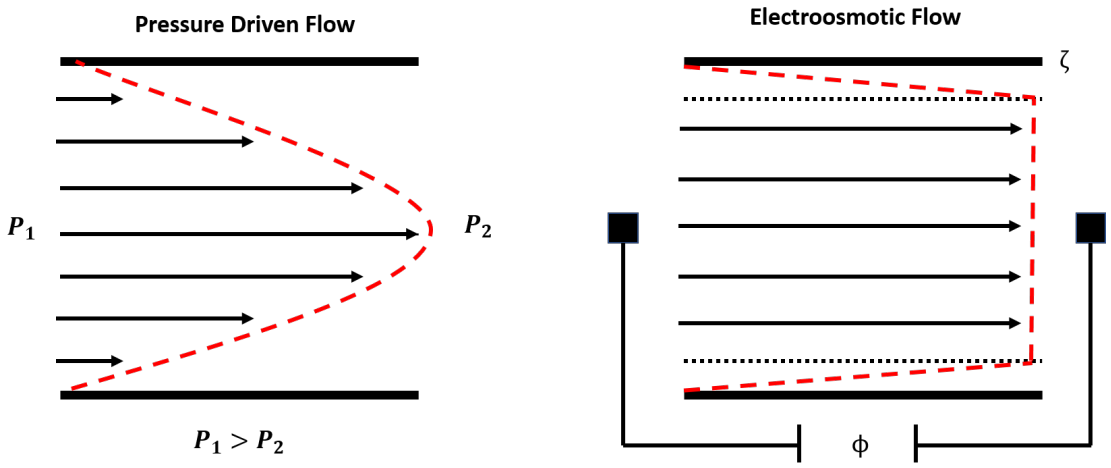

Figure A.1: Pressure driven versus electroosmotic flow profile. The pressure driven flow results in a parabolic flow profile while the electroosmotic flow with an applied voltage of ϕ results in a plug flow velocity profile. Near the wall of the EOF conduit in the EDL, the velocity increases until outside of the EDL there is no net charge to fight viscous forces, and the velocity profile plateus.

For microfluidic applications, the Navier-Stokes equation can often be simplified by assuming negligible inertial forces (Re $<<$ 2300; laminar flow) and gravitational forces allowing equation A.17 to be rewritten as

$$\boldsymbol{\nabla} p = \mu \boldsymbol{\nabla}^2 \mathbf{u}. \tag{A.18}$$

Currently there is no general solution to the Navier-Stokes equation, but can be solved in specific applications with simplifying assumptions, and is widely used in computational approximations.

A.2 Laminar Flow

Laminar flow describes the condition where the velocity of a particle in fluid flow is not a random function of time. This is in contrast to turbulent flow which is chaotic [41]. The dimensionless Reynold number can quantitatively characterize a fluid flow and is a ratio of inertial and viscous forces. The Reynold number can be expressed as

$$\text{Re} = \frac{\rho v L}{\mu}, \tag{A.19}$$

where ρ is the fluid density, v is the characteristic fluid velocity, μ is the fluid viscosity, and L is the characteristic length. In many cases, the characteristic length is the hydraulic diameter (D_h). The hydraulic diameter is used for fluid calculations in non-circular conduits by relating the conduit to a circular geometry in a proportion that maintains the conservation of momentum of the original conduit [41].

The hydraulic diameter can be expressed as ratio of cross-sectional area to conduit perimeter:

$$D_h = 4\frac{A}{P}, \tag{A.20}$$

where A and P are the cross-sectional area and perimeter of the conduit respectively. For a cylindrical conduit, equation A.20 simplifies to $D_h = D_c$ where D_c is the diameter of a circular cross-section. For a rectangular cross-section, the hydraulic diameter is expressed as

$$D_h = \frac{2hw}{w+h}, \tag{A.21}$$

where h and w are the height and width of the cross-sectional rectangle respectively. For turbulent flows, where the geometry is of lesser consequence, equation A.20 is a good approximation for fluid calculations, but for laminar flow, specifics of the conduit geometry is of great consequence and equation A.20 should be used with caution.

In general, flow conditions with a Reynolds number much larger than 2300 exhibit turbulent behaviours, and flow conditions with a Reynolds number much smaller than 2300 exhibit laminar flow behaviours. The laminar-turbulent transition number of 2300 is reportedly accurate for microfluidics as well [41].

Referring back to equation A.20, since the product of characteristic length and velocity for microfluidic systems, most microfluidic flows are considered laminar. An important consequence is that separate streams that come in contact will not mix via convection, but primarily through diffusion. This phenomenom can be quantified with the dimensionless Péclet number (Pe), which is defined as the ratio of convection transport to diffusion transport [60]. The Péclet number can be expressed

as

$$\text{Pe} = \frac{vL}{D} \tag{A.22}$$

where D is the diffusion coefficient. The Péclet number can also be defined with the Reynolds number

$$Pe = \text{Re Sc} \tag{A.23}$$

where Sc is the dimensionless Schmidt number and describes the ratio of momentum diffusivity and and mass diffusivity. The Schmidt number can be calculated as

$$\text{Sc} = \frac{\mu}{\rho D} \tag{A.24}$$

For fluid systems where Pe is much larger than 1, the system is convection dominated and when Pe is much smaller than 1, the system is diffusion dominated. Again, the product of the characteristic velocity and length in microfluidic systems is usually very small so in BioMEMS, the system is diffusion dominated and cannot rely on convective mixing. To facilitate mixing in microfluidic systems, the device should be designed to create large surface areas between streams to expedite the diffusion process, or stimulate turbulent flow to create convective transport.

A.3 Diffusion

Since microfluidic flow is almost always laminar, mixing will mainly occur via diffusion (figure A.2) [41]. Diffusion is the phenomenon where a concentration will average over a volume by Brownian motion. Fick's laws gives a quantitative description of diffusion. The first law states that the molar flux of a dissolved species is proportional to the concentration gradient of that species and can be expressed as

$$\boldsymbol{J} = -D\boldsymbol{\nabla}C, \tag{A.25}$$

where $\boldsymbol{J}$ is the molar flux of a diffusive species, $\boldsymbol{\nabla}C$ is the concentration gradient, and D is a proportionality factor known as the translational diffusion constant.

Fick's second law arises from the continuity of mass

$$\frac{\partial C}{\partial t} + \boldsymbol{\nabla} \cdot \boldsymbol{J} = 0, \tag{A.26}$$

And by substituting in Fick's first law (equation A.25), Fick's second law can be expressed as

$$\frac{\partial c}{\partial t} = D\Delta C \tag{A.27}$$

Equation A.27 describes the time and spatial dependencies of concentrations.

By examining the random walk of a particle due to Brownian motion, the mean displacement of particles can be described:

$$\left\langle r^2 \right\rangle = 2NDt \tag{A.28}$$

where $< r^2 >$ is the squared mean displacement of a particle, $N = 1$, 2, or 3 for analysis in 1, 2, or 3 dimensions respectively, t represents the time elapsed, and D is the translation diffusion constant.

The translation diffusion constant is a ratio of thermal motion and viscous resistance terms and can be generally expressed as

$$D = \frac{k_b T}{f_r}, \tag{A.29}$$

where k_b is the boltzman constant, T is the temperature, and f_r is the mean friction coefficient [61], [59]. The mean friction coefficient arises from the average of the translation friction tensor (f_{ij}) components. This tensor describes the viscous force on a particle as a function of velocity:

$$F_i = f_{ij} v_j \tag{A.30}$$

where for a rigid particle

$$f_{ij} = 6\pi\mu R_{ij}, \tag{A.31}$$

where μ is the fluid viscosity, and R_{ij} is the translation tensor that describes the equivalent radius. For a spherical particle, R_{ij} reduces to the radius of the sphere and f_{ij} becomes the viscous resistance from Stokes law. In this special case, the diffusion translation constant becomes

$$D_o = \frac{k_B T}{6\pi\mu r}, \tag{A.32}$$

and is known as the Stokes-Einstein equation. For spheroid particles where the radius depends on the orientation of the particle, the mean friction coefficient can be used since brownian motion will randomly move the particle in all directions. From the translation friction tensor, the mean friction coefficient can be described as

$$f_r^{-1} = \frac{1}{3}(\frac{1}{f_1} + \frac{1}{f_2} + \frac{1}{f_3}) \tag{A.33}$$

where f_1, f_2, and f_3 refer to the components of the main diagonal of the translation friction tensor [59].

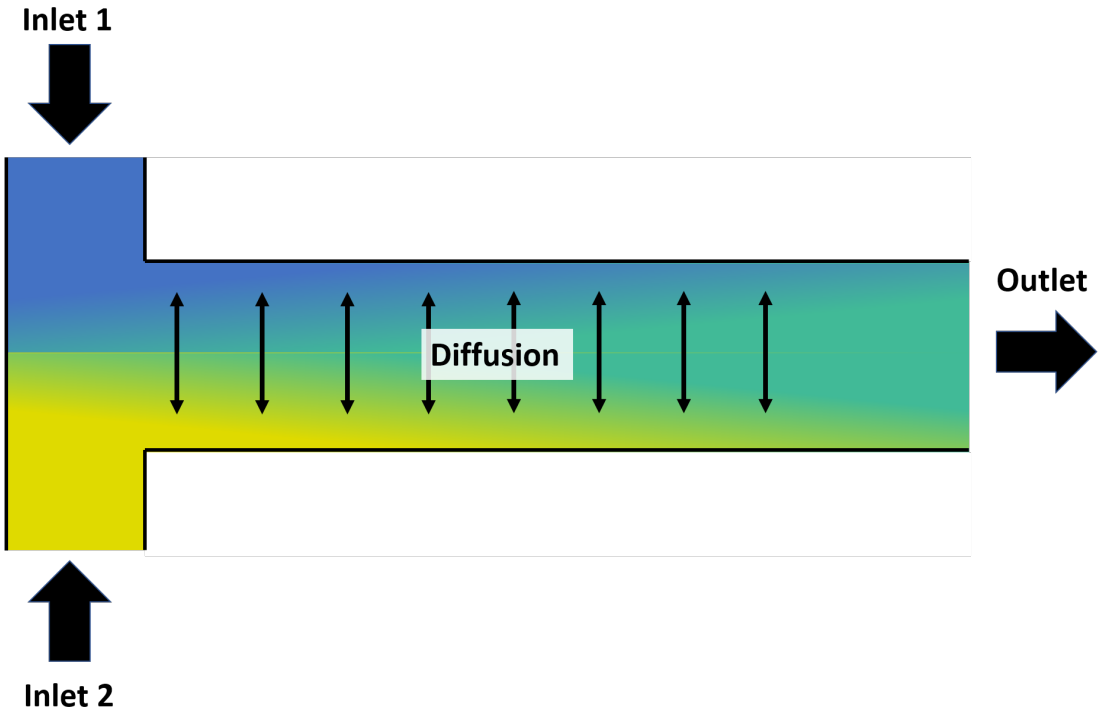

Figure A.2: Illustration of diffusion dominated transport.

A.4 Hydraulic Resistance

Fluid resistance is a powerful analogy of fluid flow to Ohm's law where pressure is analagous to electric potential, and volumetric flow rate (Q) is analagous to electrical current:

$$\Delta V = IR, \tag{A.34}$$

$$\Delta P = QR. \tag{A.35}$$

In both equation A.34 and A.35 there is a quantity referred to as the resistance that resists a flow under an applied voltage or pressure.

If the velocity profile is solved for from the Navier-Stokes equation and is integrated over the volume of the conduit, the volumetric flow rate as a function of applied force can be derived. In the case of pressure-driven flow of a non-compressible Newtonian fluid through a cylindrical conduit, the Hagen-Pouisuelle equation is derived, and is expressed as

$$\Delta P = Q\frac{8\mu L}{\pi R_c^4} \tag{A.36}$$

where L is the length of the conduit, R_c is the radius of the conduit, and μ is the viscosity. In the case of Hagen-Pouisuelle flow, the hydraulic resistance is

$$R = \frac{8\mu L}{\pi R_c^4}. \tag{A.37}$$

In the case of a rectangular conduit, the hydraulic resistance can be expressed as

$$R = \frac{12\mu L}{wh^3}\left[1 - \frac{h}{w}\left(\frac{192}{\pi^5}\sum_{n=1,3,5}^{\infty}\frac{1}{n^5}\tanh\left(\frac{n\pi w}{2h}\right)\right)\right]^{-1}, \tag{A.38}$$

where w and h are the cross-sectional width and height of conduit respectively [41]. If the width is far greater or smaller than the width, the hydraulic resistance can be

expressed by a much simpler expression [41]:

$$R = \frac{12\mu L}{wh^3} \tag{A.39}$$

The Ohm's law analogy of fluid flow can be expanded to other circuit techniques such as equivalent parallel and series resistors, and Krichoff's current and voltage laws. This analogy allows for the design of complicated fluid networks at the system level.

Chapter B: Detailed Analytic Impedance Solution

Impedance is the resistance of electrical current flow of a system for a given voltages signal. For dielectric materials, the impedance is related to the complex permittivity expressed as

$$\tilde{\epsilon} = \epsilon - j\frac{\sigma}{\omega} \tag{B.1}$$

where ϵ is the permittivity, $j = \sqrt{-1}$, σ is the conductivity, and ω is the angular frequency. The impedance of a single cell suspension, such as depicted in figure B.1, can be solved for with Maxwell's mixture thoery [11], [30].

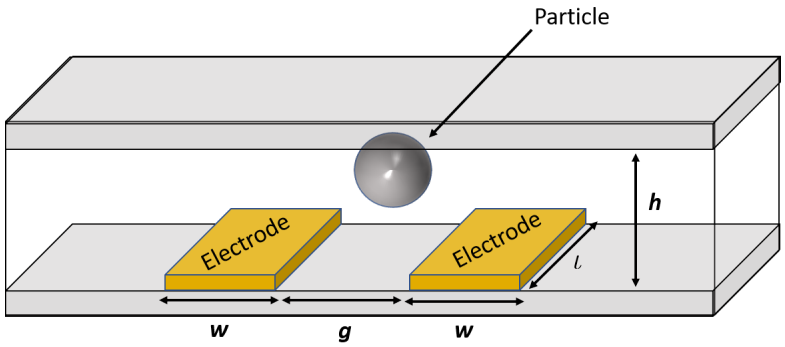

Figure B.1: Schematic diagram of simplified impedance sensor chamber where w, g, and l are the width, gap, and length of the electrodes respectively, and h is the height of the chamber.

B.1 Maxwell's Mixture Theory

Maxwell's equation for the complex permittivity of a mixture is

$$\tilde{\epsilon}_{mix} = \tilde{\epsilon}_m \frac{1 + 2\Phi\tilde{f}_{CM}}{1 - \Phi\tilde{f}_{CM}} \tag{B.2}$$

where $\tilde{\epsilon}_{mix}$ is the complex permittivity of the mixture, $\tilde{\epsilon}_m$ is the complex permittivity of the medium, $\tilde{f}_{CM}$ is the Clausius Mossotti factor, and Φ is the volume fraction.

The Clausius Mossotti factor is defined as

$$\tilde{f}_{CM} = \frac{\tilde{\epsilon}_p - \tilde{\epsilon}_m}{\tilde{\epsilon}_p + 2\tilde{\epsilon}_m} \tag{B.3}$$

where $\tilde{\epsilon}_p$ is the complex permittivity of the particle and $\tilde{\epsilon}_m$ is the complex permittivity of the medium.

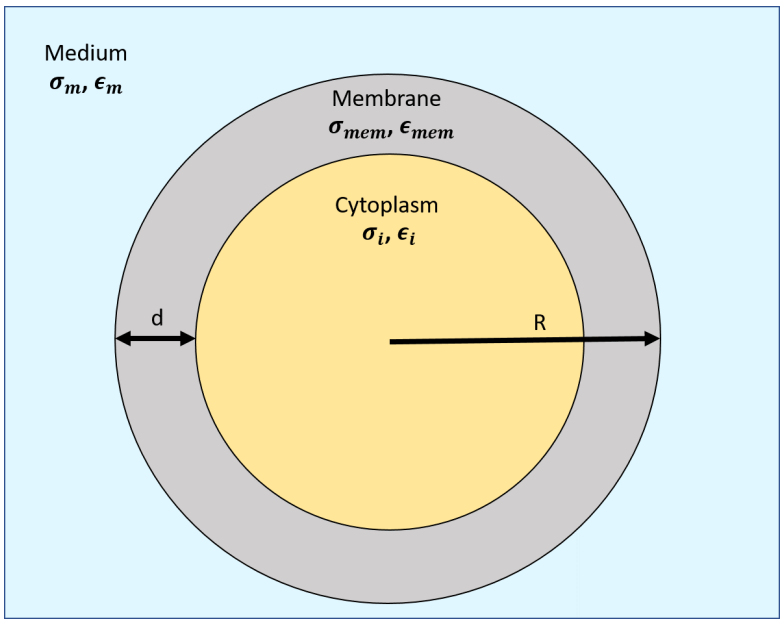

Figure B.2: A diagram of a single shelled cell model where σ_m, ϵ_m; σ_{mem}, ϵ_{mem}; σ_i, and ϵ_i are the conductivity and permittivity of the medium, cell membrane, and cell cytoplasm respectively. R and d are the radius of the cell and membrane thickness respectively.

The permittivity of the single shelled cell in figure B.2, can be modelled as

$$\tilde{\epsilon}_p = \tilde{\epsilon}_{mem} \frac{\gamma^3 + 2(\frac{\tilde{\epsilon}_i - \tilde{\epsilon}_{mem}}{\tilde{\epsilon}_i + 2\tilde{\epsilon}_{mem}})}{\gamma^3 - (\frac{\tilde{\epsilon}_i - \tilde{\epsilon}_{mem}}{\tilde{\epsilon}_i + 2\tilde{\epsilon}_{mem}})} \quad \text{with } \gamma = \frac{R+d}{R} \tag{B.4}$$

where $\tilde{\epsilon}_i$ is the complex permittivity of the cytoplasm, $\tilde{\epsilon}_{mem}$ is the complex permittivity of the cell membrane, R is the radius of the cell, and d is the thickness of the cell membrane.

The impedance of the mixture is

$$\tilde{Z}_{mix} = \frac{1}{jw\tilde{C}_{mix}} \tag{B.5}$$

where w is the angular frequency and $\tilde{C}_{mix}$ is the complex capacitance of the mixture and can be expressed as

$$\tilde{C}_{mix} = \tilde{\epsilon}_{mix} G_f \tag{B.6}$$

If equations B.5 and B.6 are combined, we obtain

$$\tilde{Z}_{mix} = \frac{1}{jw\tilde{\epsilon}_{mix} G_f} \tag{B.7}$$

To find the value of the geometric factor G_f, the cell constant of the electrodes must be determined.

B.2 Electrode Cell Constant

The cell constant κ is defined as the proportionality factor between the measured resistance R_b and the resistivity ρ of a material.

$$R_b = \kappa\rho \tag{B.8}$$

Olthius related the measured resistance to capacitance in order to derive an analytic solution to cell constant [34].

To find R_b for two electrodes with an interspatial material, the measured resistance can be related to capacitance via Ohm's law and Maxwell's equation.

$$RC = \frac{\oiint \epsilon \boldsymbol{E} \cdot d\boldsymbol{S}}{\oiint \sigma \boldsymbol{E} \cdot d\boldsymbol{S}} \tag{B.9}$$

where R and C are the resistance and capacitance between the electrodes, ϵ is the product of the relative and vacuum permittivity, $\boldsymbol{E}$ is the electric field vector, and the integral is taken over a surface including one electrode.

If the interspatial material is homogeneous and isotropic, then equation B.9 can be reduced to

$$RC = \frac{\epsilon}{\sigma} \tag{B.10}$$

If we take $R_b = R$, we can combine equation B.10 and B.8 to express the cell

constant in terms of capacitance.

$$\kappa = \frac{\epsilon}{C} \tag{B.11}$$

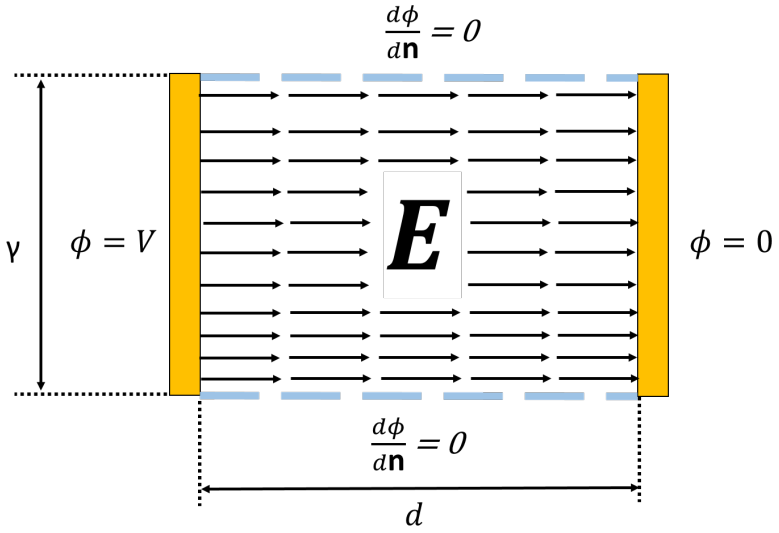

Figure B.3: Uniform electric field between two parallel electrodes where $\boldsymbol{E}$ is the electric field, ϕ is the voltage, and $\frac{d\phi}{d\boldsymbol{n}} = 0$ is the boundary condition of a perfect insulator. The dimensions of the capacitor are the electrode height γ, and the distance between the electrodes d.

The capacitance of the two parallel plates with a uniform electrode field in figure B.3 is

$$C = \frac{\epsilon A}{d} \tag{B.12}$$

where A is the area of the plate and d is the distance between the plates. Since $A = l\gamma$, where l is the width, and γ is the height of the electrode, the capacitance per unit width can be written as

$$C_l = \frac{\epsilon\gamma}{d} \quad \text{where} \quad C = l\,C_l \tag{B.13}$$

Returning to equation B.11, and substituting equation B.13, the cell constant can be expressed as

$$\kappa = \frac{d}{\gamma\,l} \tag{B.14}$$

The geometric factor is related to the cell constant by

$$G_f = (\kappa)^{-1} \tag{B.15}$$

By combining equations B.14 and B.15, the geometric factor can be expressed as

$$G_f = \frac{\gamma l}{d} \tag{B.16}$$

Equation B.16 is the solution of the geometric constant for the electrode configuration in figure B.3, but to find the geometric constant for any other configuration, including the coplanar electrode in figure B.1, d and γ will need to be mapped to parameters in the other configuration. This will be accomplished in the next section with conformal transformations.

B.3 Conformal Transformations

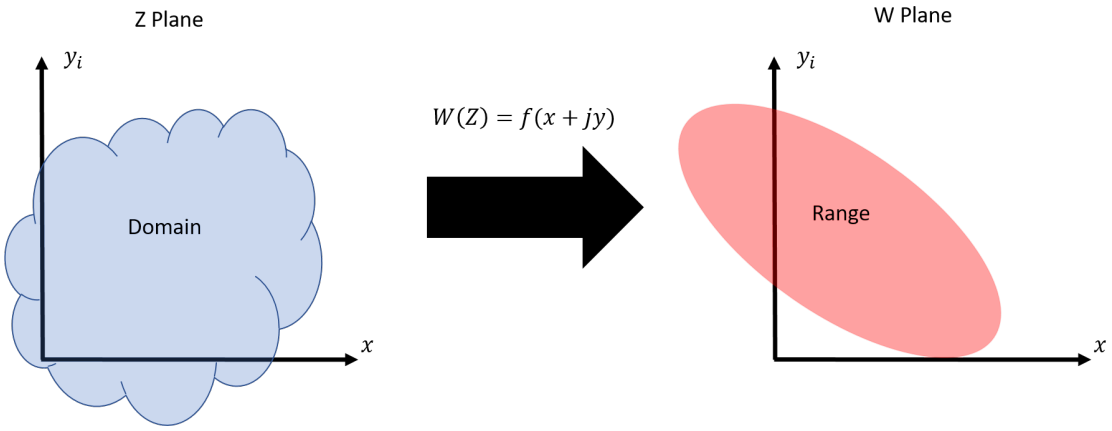

Figure B.4: An Illustration of complex mapping.

Let $z = x + j\,y$, where j is the imaginary number $\sqrt{-1}$, then a function of z, such as $W(z) = u(x, y) + j\,v(x, y)$, can be considered a mapping of an area of one complex plane to an area in another complex plane (figure B.4). Conformal transformations are a special kind of mapping between two complex planes that preserves local angles. A mapping is conformal if it is composed of analytic functions, and as a consequent, fulfills the Cauchy-Rieman equations. Conformal mappings are

extremely useful for solving problems in complicated domains by mapping the problem to a new domain where the problem is simplified. An example of a conformal mapping is $w(z) = tan(z)$, which maps an infinite vertical strip to a circle (figure B.5).

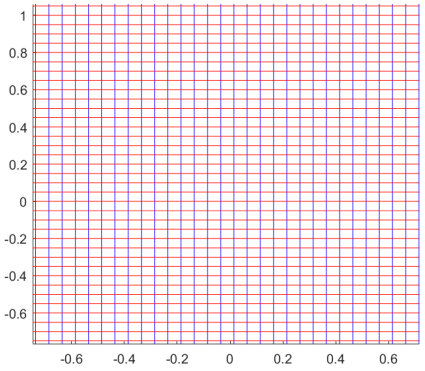

(a) Part of the partial infinite strip $-\pi/4 < x < \pi/4$.

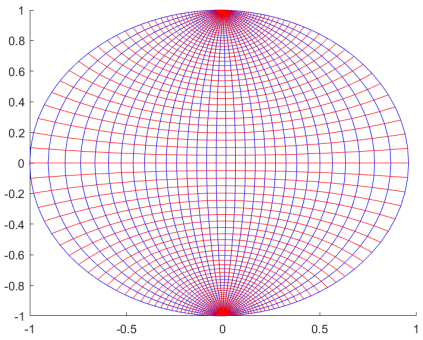

(b) Mapping of the partial infinite vertical strip to a circle

Figure B.5: An example of conformal mapping by transforming a partial infinite vertical strip to a circle with the mapping $w(z) = tan(z)$.

Sun, Greene, et al. utilized the Schwartz-Christoffel transform to map the coplanar electrode configuration in figure B.1 to the configuration of parallel electrodes with uniform electrode fields in figure B.3 [31]. The Schwartz-Christoffel formula is a powerful transform that allows the mapping of the upper complex T-plane ($y > 0$) to the inside of a polygon. The formula is

$$Z = C_1 \int_{T_0}^{T} \prod_{r=1}^{m} (T - T_r)^{(\theta_r/\pi - 1)} dT + C_2 \tag{B.17}$$

where Z is the interior of a polygon in the Z-plane with vertices $Z_1,\ Z_2,\ Z_3,\ ..., Z_m$ and angles $\theta_1,\ \theta_2,\ \theta_3,\ ..., \theta_m$ which correspond to the points $T_1,\ T_2,\ T_3,\ ..., T_m$ on the real axis of the T-plane. C_1 and C_2 are integration constants. The Schwartz-Christoffel transform has three degrees of freedom, and consequently, up to three points may be chosen arbitrarily. T_0 is the reference and is typically chosen at the origin.

To find the geometric constant for coplanar electrodes, Schwartz-Christoffel trans-

forms will be used to map the coplanar electrode geometry (Z-plane) to the upper complex plane (T-plane) and then to map the T-plane to the W-plane. The W-plane vastly simplifies the solution to the cell constant, and the goemetric constant can be solved for with equation B.16.

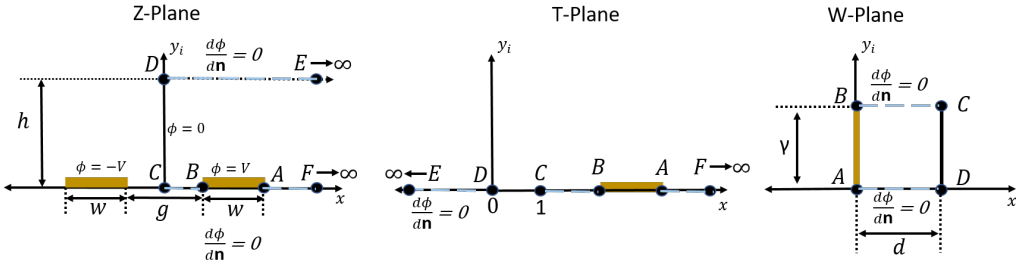

Figure B.6: Diagrams of coplanar electrodes through Schwartz-Christoffel mapping where the Z-plane contains the physical dimensions of the electrode configuration, the T-Plane links the Schwartz-Christoffel mappins of Z and W plane, and the W-plane represents the parallel electrodes producing a uniform electrode field.

B.3.1 Schwartz-Christoffel Transform: T to Z Mapping

Mapping the T-plane to the Z-plane, point C and D will be chosen as the polygon corners with angles of $\pi/2$.

$$Z = C_1 \int (T - T_c)^{-1/2} (T - T_D)^{-1/2} dT + C_2 \tag{B.18}$$

To integrate

$$\int (T - T_D)^{-1/2} (T - T_C)^{-1/2} dT$$

Substitute $u = (T - T_C)^{1/2}$ with $du = \frac{1}{2}(T - T_C)^{-1/2}\, dT$

$$= 2 \int \frac{du}{\sqrt{T - T_D}} \quad \text{with } T = u^2 + T_C$$

$$= 2 \int \frac{du}{\sqrt{u^2 + T_C - T_D}}$$

$$= 2 \int \frac{\sqrt{T_C - T_D}}{\sqrt{\frac{u^2}{T_C - T_D} + 1}}\ du$$

substitute $t = \frac{u}{\sqrt{T_C - T_D}}$; $dt = \frac{du}{\sqrt{T_C - T_D}}$

$$= 2 \int \frac{dt}{\sqrt{t^2 + 1}}$$

Substitute $t = tan(s)$ with $dt = \sec^2 s$

$$= 2 \int \sec(s) ds$$

$$= 2 \ln(\tan(s) + \sec(s))$$

$$= 2 \ln(t + \sec(\arctan(t)))$$

$$= 2\ln(t + \sqrt{s^2+1})$$

$$= 2\ln\left(\frac{u}{\sqrt{T_C - T_D}} + \sqrt{\frac{u^2}{T_C - T_D} + 1}\right)$$

$$= 2\ln\left(\frac{u}{\sqrt{T_C - T_C}} + \sqrt{\frac{u^2 + T_C - T_D}{T_C - T_D}}\right)$$

$$= 2\ln\left(\sqrt{\frac{T - T_C}{T_C - T_D}} + \sqrt{\frac{T - T_D}{T_C - T_D}}\right)$$

Add the integration constants from equation B.18 and combine $(T_C + T_D)^{-1/2}$ in C_2, then

$$Z = 2C_1 \ln\left(\sqrt{T - T_C} + \sqrt{T - T_D}\right) + C_2 \tag{B.19}$$

The points T_C and T_D will be chosen to be 1 and 0 respectively

$$Z = 2C_1 \ln\left(\sqrt{T-1} + \sqrt{T}\right) + C_2 \tag{B.20}$$

The integration constants can be solved by relationships in the coordinates between the Z-plane and T-plane.

For point C, $Z_C = 0$ and $T_C = 1$,

$0 = 2C_1(0) + C_2$

$C_2 = 0$

For point D, $Z_D = jh$ and $T_D = 0$,

$$jh = 2C_1 \ln(j)$$
$$jh = 2C_1(\frac{\pi}{2}j)$$
$$C_1 = \frac{h}{\pi}$$

After substituting the values of the integration constants into equation B.20,

$$Z = \frac{2h}{\pi} \ln\left(\sqrt{T-1} + \sqrt{T}\right) \tag{B.21}$$

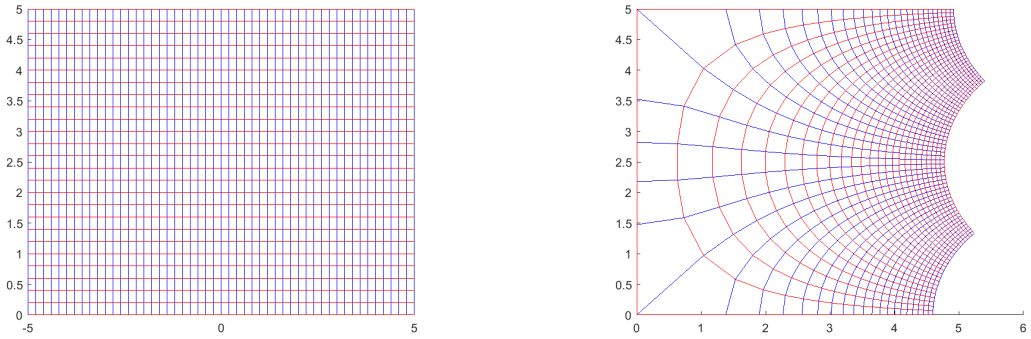

(a) Part of upper complex T-Plane

(b) Mapping of the part of the T-plane to the polygon in the Z-plane

Figure B.7: Mapping of the T-plane to the inside of the open polygon in the Z-Plane outlined by the points F, C, D, and E in the Z-plane. Equation B.21 is the mapping function.

The mapping from the Z-plane to the T-plane can be found by solving for T in equation B.21.

$$Z = \frac{2h}{\pi} \ln\left(\sqrt{T-1} + \sqrt{T}\right)$$

$$\frac{Z\pi}{2h} = \ln\left(\sqrt{T-1} + \sqrt{T}\right)$$

And utilizing the inverse hyperbolic identity

$$\operatorname{arccosh}(z) = \ln\left(z + \sqrt{z-1}\sqrt{z+1}\right)$$

$$\operatorname{arccosh}(z) = \ln\left(z + \sqrt{z^2-1}\right)$$

Substitute $z = \sqrt{T}$

$$\operatorname{arccosh}(\sqrt{T}) = \ln\left(\sqrt{T} + \sqrt{T-1}\right)$$

Then T can be solved for as

$$T = \cosh^2\left(\frac{z\pi}{2h}\right) \tag{B.22}$$

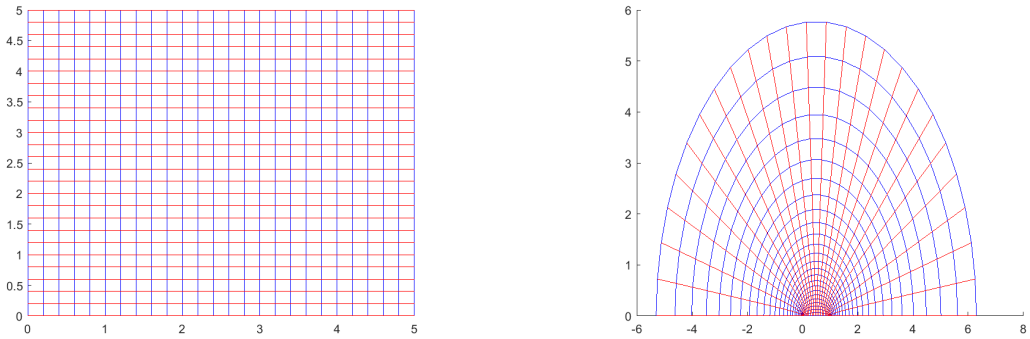

(a) Part of the open polygon in the Z-plane.

(b) Mapping of part of the polygon in the Z-plane to the T-plane.

Figure B.8: Mapping of the open polygon in the Z-Plane outlined by the points F, C, D, and E to the T-plane. Equation B.22 is the mapping function.

B.3.2 Schwartz-Christoffel Transform: W to T Mapping

Mapping the T-plane to the W-Plane, points A, B, C, and D, will be chosen as the polygon corners with angles of $\pi/2$.

$$W = D_1 \int (T - T_A)^{-1/2}(T - T_B)^{-1/2}(T - T_C)^{-1/2}(T - T_D)^{-1/2}\, dT + D_2 \tag{B.23}$$

Since equation B.23 is an integral of a rational function with a root of a quartic

polynomial, the function can be rewritten as an elliptic integral [50].

$$W = D_3 F(v,k) + D_2 \tag{B.24}$$

$$D_3 = \frac{2D_1}{\sqrt{(T_A - T_C)(T_B - T_D)}} \tag{B.25}$$

$$v = \arcsin\sqrt{\frac{(T_B - T_D)(T - T_A)}{(T_A - T_D)(T - T_B)}} \tag{B.26}$$

$$k = \sqrt{\frac{(T_B - T_C)(T_A - T_D)}{(T_A - T_C)(T_B - T_D)}} \tag{B.27}$$

Where $F(v,k)$ is the incomplete elliptic integral of the first kind, and can be expressed as

$$F(v,k) = \int_0^v \frac{d\alpha}{\sqrt{1 - k^2 \sin^2 \alpha}} \tag{B.28}$$

Where v and k are referred to as the amplitude and modulus respectively. For all values of T that are greater than T_A or do not lay on the real number line (i.e. has an imaginary component), the elliptic integral provided is valid.

Solving for the integral constants, for point A, $W_A = 0$ and $v = 0$

$$0 = D_3 F(0,k) + D_2$$

$$F(0,k) = 0$$

$$D_2 = 0$$

For point D, $W_D = d$ and $v = \pi/2$

$$d = D_3 F(\pi/2, k)$$

$$D_3 = \frac{d}{F(\pi/2,k)}$$

$$D_3 = \frac{d}{K(k)}$$

Where $K(k)$ is the complete elliptic integral and is expressed as

$$K(k) = \int_0^{\pi/2} \frac{d\alpha}{1 - k^2 \sin^2(\alpha)} \tag{B.29}$$

For point B, $W_B = j\gamma$ and $\lim_{x\to 0} v(T_B + jx)$

$$j\gamma = \lim_{x\to 0} D_3 F(v(T_B + jx), k)$$
$$D_3 = \lim_{x\to 0} \frac{F(v(T_B + jx), k)}{j\gamma}$$

Equating the two solutions for D_3, the Geometric factor (equation B.16) in the W-Plane can be mapped to T-plane and, using equation B.22, mapped to the Z-plane.

$$D_3 = \frac{d}{K(k)} = \frac{j\gamma}{\lim_{x\to 0} F(v(T_B + jx), k)} \tag{B.30}$$

$$G_f = \frac{\gamma l}{2\, d} = \frac{\lim_{x\to 0} F(v(T_B + jx), k) l}{j\, 2\, K(k)} \tag{B.31}$$

A constant of two appears in the denominator of B.31 since the conformal mapping takes advantage of symmetry and only accounts for half of the disance between the electrodes in the W-plane (figure B.6).

However, the expression $\lim_{x\to 0} F(v(T_B + jx), k)$ is inconvenient to handle, but by using the imaginary-argument transform, it can be shown that $\lim_{x\to 0} F(v(T_B + jx), k) = iK(k')$.

The Imaginary-argument transform states that

$$F(i\phi, k) = iF(\psi, k') \text{ with } \sinh\phi = \tan\psi \tag{B.32}$$

Where $k' = \sqrt{1 - k^2}$ and is called the complement modulus. Applying the imaginary-argument transform,

$$\psi = \lim_{x\to 0} \arctan\left(\sinh\left(\frac{\arcsin\sqrt{\frac{(T_B - T_D)(T_B + jx - T_A)}{(T_A - T_D)(T_B + jx - T_B)}}}{j}\right)\right) \tag{B.33}$$

Working from the inside out,

$$\lim_{x\to 0} \frac{(T_B - T_D)(T_B + jx - T_A)}{(T_A - T_D)(T_B + jx - T_B)}$$

$$= \lim_{x\to 0} \frac{(T_B - T_D)(T_B + jx - T_A)}{(T_A - T_D)jx} \qquad \text{where } T_D = 0$$

$$= \lim_{x\to 0} \frac{T_B}{T_A}\frac{(T_B - T_A)}{jx} + \frac{T_B}{T_A}$$

Since $T_A > T_B$, then $T_B - T_A < 0$. Therfore,

$$\lim_{x\to 0} \frac{(T_B - T_D)(T_B + jx - T_A)}{(T_A - T_D)(T_B + jx - T_B)} = -\infty. \tag{B.34}$$

Substituting the results from equation B.34 into equation B.33,

$$\psi = \lim_{x\to -\infty} \arctan\left(\sinh\left(\frac{\arcsin\sqrt{x}}{j}\right)\right) = \arctan\left(\sinh\left(\frac{\arcsin(j\infty)}{j}\right)\right) \tag{B.35}$$

Working from the inside out and starting with the definition of $\arcsin x$,

$$\arcsin x = -j\ln(jx + \sqrt{1-x^2})$$

$$\arcsin(jx) = -j\ln(\sqrt{1+x^2} - x)$$

$$\lim_{x\to\infty} \arcsin(jx) = \lim_{x\to} -j\ln(\sqrt{1+x^2} - x)$$

$$= \lim_{x\to\infty} -j\ln\left(\frac{(\sqrt{1+x^2}+x)(\sqrt{1+x^2}-x)}{(\sqrt{1+x^2}+x)}\right)$$

$$= \lim_{x\to\infty} -j\ln\left(\frac{1}{x(\sqrt{1/x^2+1}+1)}\right)$$

$= -j \ln(0)$

$$\lim_{x\to\infty} \arcsin(jx) = j\infty \tag{B.36}$$

Substituting equation B.36 into equation B.35

$$\psi = \lim_{x\to\infty} \arctan(\sinh(x)). \tag{B.37}$$

Applying the following common limits,

$$\lim_{x\to\infty} \sinh x = \infty,$$
$$\lim_{x\to\infty} \arctan x = \frac{\pi}{2},$$

$$\psi = \frac{\pi}{2} \tag{B.38}$$

And then applying the results of equation B.38 to equation B.32,

$$F(\lim_{x\to 0} v(T_B + jx), k) = jF(\pi/2, k') \tag{B.39}$$

$$F(\lim_{x\to 0} v(T_B + jx), k) = jK(k') \tag{B.40}$$

Returning to the mapping of the geometric factor (equation B.30, and B.31), D_3 and G_f can be expressed as

$$D_3 = \frac{d}{K(k)} = \frac{\gamma}{K(k')} \tag{B.41}$$

$$G_f = \frac{lK(k')}{2\,K(k)} \tag{B.42}$$

B.4 Solution to the Electric Field

Now with Z-T and T-W mappings, the solution of the electric field in the W-plane can be mapped to the Z-plane. The mapping of the electric field can be expressed as

$$\boldsymbol{E_z} = -\nabla\phi_z \text{ with } \nabla\phi_z = \nabla\phi_w \overline{\frac{dW}{dZ}} \tag{B.43}$$

Where $\nabla\phi$ is the gradient of potential and $\overline{\frac{dW}{dZ}}$ is the conjugate of the derivative of W with respect to Z [51].

Applying the chain rule to equation B.43, the electric field mapping is expressed as

$$\boldsymbol{E_z} = -\nabla\phi_w \overline{\frac{dW}{dT}\frac{dT}{dZ}} \tag{B.44}$$

The gradient of ϕ_w can be reduced to $\frac{d}{dx}\phi_w$ since the electric potential in the W-plane is independent of the y and z direction (figure B.6). The electric potential and electric field in the W-plane can be expressed as

$$\phi_w = V\Big(1 - \frac{x}{d}\Big) \tag{B.45}$$

$$E_w = -\nabla\phi_w = \frac{V}{d} \tag{B.46}$$

$\frac{dW}{dT}$ can be found by integrating equation B.23.

$$\frac{dW}{dT} = \frac{d}{K(k)} \frac{(T_A - T_C)^{1/2}(T_B - T_D)^{1/2}}{(T - T_A)^{1/2}(T - T_B)^{1/2}(T - T_C)^{1/2}(T - T_D)^{1/2}} \tag{B.47}$$

And $\frac{dT}{dz}$ can be found by integrating equation B.22.

$$T = \cosh^2\Big(\frac{Z\pi}{2h}\Big)$$

$$\frac{dT}{dZ} = 2\cosh\Big(\frac{Z\pi}{2h}\Big)\sinh\Big(\frac{Z\pi}{2h}\Big)\frac{\pi}{2h} \qquad \text{Substitute equation B.21}$$

$$\frac{dT}{dZ} = \frac{\pi}{h}\cosh\Big(\ln(\sqrt{T-1} + \sqrt{T})\Big)\sinh\Big(\ln(\sqrt{T-1} + \sqrt{T})\Big)$$

And then applying the inverse cosh and sinh log relations,

$$\operatorname{arccosh} x = \ln(x + \sqrt{x^2 - 1})$$

$$\operatorname{arcsinh} x = \ln(x + \sqrt{x^2 + 1})$$

$$\frac{dT}{dZ} = \frac{\pi}{h}(\sqrt{T - T_D})(\sqrt{T - T_C}) \tag{B.48}$$

Combining equations, B.44, B.46, B.47, and B.48, the electric field for the coplanar electrodes can be expressed as equation B.49 and is depicted in figure B.9

$$E_z = \overline{\frac{\pi V}{2hK(k)} \frac{\sqrt{(T_A - T_C)(T_B - T_D)}}{\sqrt{(T - T_A)(T - T_B)}}} \tag{B.49}$$

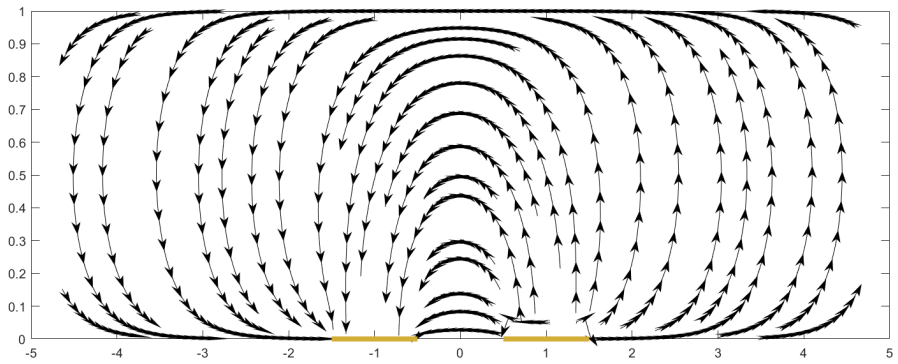

Figure B.9: The electric field for coplanar electrodes as defined by equation B.49.

Bibliography

[1] M. A. Mansor, M. Takeuchi, M. Nakajima, Y. Hasegawa, and M. R. Ahmad, "Electrical impedance spectroscopy for detection of cells in suspensions using microfluidic device with integrated microneedles," *Applied Sciences (Switzerland)*, vol. 7, no. 2, 2017, ISSN: 1454-5101. DOI: 10.3390/app7020170. [Online]. Available: https://pure.utm.my/en/publications/electrical-impedance-spectroscopy-for-detection-of-cells-in-suspe (visited on 12/04/2017).

[2] C. Kantara, M. R. O'connell, G. Luthra, A. Gajjar, S. Sarkar, R. L. Ullrich, and P. Singh, "Methods for detecting circulating cancer stem cells (CCSCs) as a novel approach for diagnosis of colon cancer relapse/metastasis," *Laboratory investigation*, vol. 95, no. 1, pp. 100–112, 2015.

[3] P. K. Pandey, P. H. Kass, M. L. Soupir, S. Biswas, and V. P. Singh, "Contamination of water resources by pathogenic bacteria," *AMB Express*, vol. 4, no. 1, p. 51, 2014.

[4] J.-J. Fadriquela, "Design, Fabrication, and Implementation of a Single-Cell Capture Chamber for a Microfluidic Impedance Sensor," *Master's Theses and Project Reports*, Jun. 1, 2009. DOI: 10.15368/theses.2009.98. [Online]. Available: http://digitalcommons.calpoly.edu/theses/189.

[5] S. Hernandez, "Single Cell Impedance Measurements using Microfabricated Electrodes and Labview Graphical Programming," *Master's Theses and Project Reports*, Dec. 1, 2009. DOI: 10.15368/theses.2009.192. [Online]. Available: http://digitalcommons.calpoly.edu/theses/225.

[6] Daniel D Chiras, *Human Biology*, 5th Edition. Boston: Jones and Bartlett, 2005.

[7] LadyofHats, *English: This is a diagram of an animal cell. i based my information on this diagrams:* Apr. 2006. [Online]. Available: https://commons.wikimedia.org/wiki/File:Animal_cell_structure_en.svg (visited on 12/12/2019).

[8] B. Kirby. (Aug. 31, 2016). The cell membrane, NIST Center for Neutron Research, [Online]. Available: https://www.ncnr.nist.gov/programs/reflect/rp/biology/cell_membrane.html (visited on 12/12/2019).

[9] T. N. Swaminathan and H. H. Hu, "Effect of induced-charge double layer on dielectrophoretic motion of particles," *Mechanics Research Communications*, vol. 36, no. 1, pp. 46–54, 2009.

[10] Hober R, "Eine Methode die elektrishche Leitfaehigkeit im Innern von Zellenzu messen," *Arch. Ges. Physiol*, no. 133, pp. 237–259, 1910.

[11] James Clerk Maxwell, *A Treatise on Electricity and Magnetism*, 3d ed. Oxford, Clarendon, 1892.

[12] Fricke H, "A mathematical treatment of the electrical conductivity of colloids and cell suspensions," *J. Gen. Physiol*, no. 6, pp. 375–384, 1924.

[13] ——, "The Electric Conductivity of Disperse Systems," *J. Gen. Physiol*, no. 24, pp. 575–587, 1924.

[14] ——, "The Electric Conductivity of and Capacity of Disperse Systems," *Physics*, no. 1, pp. 106–115, 1931.

[15] K. S. Cole, "Electric Impedance of Suspensions of Spheres," *The Journal of General Physiology*, vol. 12, no. 1, pp. 29–36, Sep. 20, 1928, ISSN: 0022-1295, 1540-7748. DOI: 10.1085/jgp.12.1.29. pmid: 19872446. [Online]. Available: http://jgp.rupress.org/content/12/1/29 (visited on 10/05/2017).

[16] H. J. Curtis and K. S. Cole, "Transverse Electric Impedance of Nitella," *The Journal of General Physiology*, vol. 21, no. 2, pp. 189–201, Nov. 20, 1937, ISSN: 0022-1295, 1540-7748. DOI: 10.1085/jgp.21.2.189. pmid: 19873046. [Online]. Available: http://jgp.rupress.org/content/21/2/189 (visited on 10/05/2017).

[17] Schwan H P, "Electrical Properties of Tissue and Cell Suspensions," *Adv. Biol. Med. Phys*, no. 5, pp. 147–209, 1957.

[18] ——, "Electrical Properties of Tissue and Cell Suspensions," *Physical Techniques in Biological Research*, no. 6, pp. 323–406, 1963.

[19] H. P. Schwan, "Electrical properties of tissues and cell suspensions: Mechanisms and models," in *Proceedings of 16th Annual International Conference of the IEEE Engineering in Medicine and Biology Society*, Nov. 1994, A70–A71 vol.1. DOI: 10.1109/IEMBS.1994.412155.

[20] B. J. Kirby, *Micro-and Nanoscale Fluid Mechanics*. Cambridge University Press, 2010.

[21] T. Muller, A. Pfennig, P. Klein, G. Gradl, M. Jager, and T. Schnelle, "The potential of dielectrophoresis for single-cell experiments," *IEEE Engineering in Medicine and Biology Magazine*, vol. 22, no. 6, pp. 51–61, Nov. 2003, ISSN: 0739-5175. DOI: 10.1109/MEMB.2003.1266047.

[22] H. Morgan, T. Sun, D. Holmes, S. Gawad, and N. G. Green, "Single cell dielectric spectroscopy," *Journal of Physics D: Applied Physics*, vol. 40, no. 1, p. 61, 2007, ISSN: 0022-3727. DOI: 10.1088/0022-3727/40/1/S10. [Online]. Available: http://stacks.iop.org/0022-3727/40/i=1/a=S10.

[23] N. G. Green and H. Morgan, "Dielectrophoresis of submicrometer latex spheres. 1. Experimental results," *The Journal of Physical Chemistry B*, vol. 103, no. 1, pp. 41–50, 1999. [Online]. Available: http://pubs.acs.org/doi/abs/10.1021/jp9829849.

[24] A. D. Goater and R. Pethig, "Electrorotation and dielectrophoresis," *Parasitology*, vol. 117, no. 7, pp. 177–189, Nov. 1999, ISSN: 1469-8161, 0031-1820. [Online]. Available: https://www-cambridge-org.ezproxy.lib.calpoly.edu/core/journals/parasitology/article/electrorotation-and-dielectrophoresis/EBA8C3B7540BD0FA53BCCE3849A18D8F (visited on 10/08/2017).

[25] I. POHL, "Dielectrophoresis," *Gambridge Monographs on Physics*, 1978. [Online]. Available: http://ci.nii.ac.jp/naid/10007135453/.

[26] W. M. Arnold and U. Zimmermann, "Rotating-field-induced rotation and measurement of the membrane capacitance of single mesophyll cells of Avena sativa," *Zeitschrift für Naturforschung C*, vol. 37, no. 10, pp. 908–915, 1982. [Online]. Available: https://www.degruyter.com/view/j/znc.1982.37.issue-10/znc-1982-1010/znc-1982-1010.xml.

[27] H. Morgan and N. G. Green, *AC Electrokinetics*. Research Studies Press, 2003. [Online]. Available: http://dl.merc.ac.ir/handle/Hannan/3349.

[28] R. Höber, "Ein zweites Verfahren, die Leitfähigkeit im Innern von Zellen zu messen," *Pflügers Archiv European Journal of Physiology*, vol. 148, no. 4, pp. 189–221, 1912. [Online]. Available: http://www.springerlink.com/index/T088M1NU04142159.pdf.

[29] R. W. DeBlois and C. P. Bean, "Counting and sizing of submicron particles by the resistive pulse technique," *Review of Scientific Instruments*, vol. 41, no. 7, pp. 909–916, 1970. [Online]. Available: http://aip.scitation.org.ezproxy.lib.calpoly.edu/doi/abs/10.1063/1.1684724.

[30] T. Sun and H. Morgan, "Single-cell microfluidic impedance cytometry: A review," *Microfluidics and Nanofluidics*, vol. 8, no. 4, pp. 423–443, Apr. 1, 2010, ISSN: 1613-4982, 1613-4990. DOI: 10.1007/s10404-010-0580-9. [Online]. Available: https://link.springer.com/article/10.1007/s10404-010-0580-9 (visited on 08/15/2017).

[31] T. Sun, N. G. Green, S. Gawad, and H. Morgan, "Analytical electric field and sensitivity analysis for two microfluidic impedance cytometer designs," *IET Nanobiotechnology*, vol. 1, no. 5, pp. 69–79, Oct. 2007, ISSN: 1751-8741. DOI: 10.1049/iet-nbt:20070019.

[32] Keysight Technologies, *Impedance Measurement Handbook: A Guide to Measurement Technology and Techniques*, 6th ed., ser. Application Notes. 2015.

[33] T. Hanai, "Theory of the dielectric dispersion due to the interfacial polarization and its application to emulsions," *Kolloid-Zeitschrift*, vol. 171, no. 1, pp. 23–31, Jul. 1, 1960, ISSN: 0368-6590, 1435-1536. DOI: 10.1007/BF01520320. [Online]. Available: https://link-springer-com.ezproxy.lib.calpoly.edu/article/10.1007/BF01520320 (visited on 09/23/2017).

[34] W. Olthuis, W. Streekstra, and P. Bergveld, "Theoretical and experimental determination of cell constants of planar-interdigitated electrolyte conductivity sensors," *Sensors and Actuators B: Chemical*, vol. 24, no. 1, pp. 252–256, Mar. 1, 1995, ISSN: 0925-4005. DOI: 10.1016/0925-4005(95)85053-8. [Online]. Available: http://www.sciencedirect.com/science/article/pii/0925400595850538.

[35] T. Sun, S. Gawad, N. G. Green, and H. Morgan, "Dielectric spectroscopy of single cells: Time domain analysis using Maxwell's mixture equation," *Journal of Physics D: Applied Physics*, vol. 40, no. 1, p. 1, 2007, ISSN: 0022-3727. DOI: 10.1088/0022-3727/40/1/S01. [Online]. Available: http://stacks.iop.org/0022-3727/40/i=1/a=S01.

[36] Y. Xia and G. M. Whitesides, "Soft lithography," *Annual review of materials science*, vol. 28, no. 1, pp. 153–184, 1998. [Online]. Available: http://www.annualreviews.org.ezproxy.lib.calpoly.edu/doi/abs/10.1146/annurev.matsci.28.1.153.

[37] W. Wang and S. A. Soper, *Bio-MEMS: Technologies and Applications*. CRC press, 2006.

[38] A. M. Foudeh, T. F. Didar, T. Veres, and M. Tabrizian, "Microfluidic designs and techniques using lab-on-a-chip devices for pathogen detection for point-of-care diagnostics," *Lab on a Chip*, vol. 12, no. 18, pp. 3249–3266, 2012.

[39] G. M. Whitesides, E. Ostuni, S. Takayama, X. Jiang, and D. E. Ingber, "Soft Lithography in Biology and Biochemistry," *Annual Review of Biomedical Engineering*, vol. 3, no. 1, pp. 335–373, 2001. DOI: 10.1146/annurev.bioeng.3.1.335. pmid: 11447067. [Online]. Available: https://doi.org/10.1146/annurev.bioeng.3.1.335.

[40] J. C. McDonald and G. M. Whitesides, "Poly(dimethylsiloxane) as a Material for Fabricating Microfluidic Devices," *Accounts of Chemical Research*, vol. 35, no. 7, pp. 491–499, Jul. 1, 2002, ISSN: 0001-4842. DOI: 10.1021/ar010110q. [Online]. Available: http://dx.doi.org/10.1021/ar010110q.

[41] D. J. Beebe, G. A. Mensing, Walker, and G. M., "Physics and Applications of Microfluidics in Biology," *Annual Review of Biomedical Engineering*, vol. 4, no. 1, pp. 261–286, 2002. DOI: 10.1146/annurev.bioeng.4.112601.125916. pmid: 12117759. [Online]. Available: https://doi.org/10.1146/annurev.bioeng.4.112601.125916.

[42] P. B. Ishai, M. S. Talary, A. Caduff, E. Levy, and Y. Feldman, "Electrode polarization in dielectric measurements: A review," *Measurement Science and Technology*, vol. 24, no. 10, p. 102 001, 2013, ISSN: 0957-0233. DOI: 10.1088/0957-0233/24/10/102001. [Online]. Available: http://stacks.iop.org/0957-0233/24/i=10/a=102001.

[43] F. Bordi, C. Cametti, and T. Gili, "Reduction of the contribution of electrode polarization effects in the radiowave dielectric measurements of highly conductive biological cell suspensions," *Bioelectrochemistry*, vol. 54, no. 1, pp. 53–61, Aug. 1, 2001, ISSN: 1567-5394. DOI: 10.1016/S1567-5394(01)00110-4. [Online]. Available: http://www.sciencedirect.com/science/article/pii/S1567539401001104.

[44] E. Gongadze, S. Petersen, U. Beck, and U. V. Rienen, "Classical models of the interface between an electrode and an electrolyte," *COMSOL Conference 2009 Milan*, [Online]. Available: https://www.comsol.com/paper/download/44928/Gongadze.pdf (visited on 09/01/2017).

[45] J. Varghese, H. Wang, and L. Pilon, "Simulating electric doulble layer capacitance of mesoporous electrodes with cylindrical pores," *Journal of the Electrochemical Society*, vol. 158, 2011, ISSN: 0013-4651, 1945-7111. DOI: 10.1149/1.3622342. [Online]. Available: https://www.seas.ucla.edu/~pilon/Publications/JES2011.pdf (visited on 09/01/2017).

[46] D. L. Chapman, "LI. A contribution to the theory of electrocapillarity," *The London, Edinburgh, and Dublin philosophical magazine and journal of science*, vol. 25, no. 148, pp. 475–481, 1913.

[47] P. B. Ishai, Z. Sobol, J. D. Nickels, A. L. Agapov, and A. P. Sokolov, "An assessment of comparative methods for approaching electrode polarization in dielectric permittivity measurements," *Review of Scientific Instruments*, vol. 83, no. 8, p. 083 118, Aug. 1, 2012, ISSN: 0034-6748. DOI: 10.1063/1.4746992. [Online]. Available: http://aip.scitation.org.ezproxy.lib.calpoly.edu/doi/abs/10.1063/1.4746992.

[48] Y. Feldman, R. Nigmatullin, E. Polygalov, and J. Texter, "Fractal-polarization correction in time domain dielectric spectroscopy," *Physical Review E*, vol. 58, no. 6, pp. 7561–7565, Dec. 1, 1998. DOI: 10.1103/PhysRevE.58.7561. [Online]. Available: https://link.aps.org/doi/10.1103/PhysRevE.58.7561.

[49] ——, "Fractal-polarization correction in time domain dielectric spectroscopy," *Physical Review E*, vol. 58, no. 6, p. 7561, 1998.

[50] I.S. Gradshteyn, *Table of Integrals, Series, and Products*. Academic Press, 1980.

[51] R. Schinzinger and P. A. A. Laura, *Conformal Mapping: Methods and Applications*. Courier Corporation, Apr. 30, 2012, 628 pp., ISBN: 978-0-486-15074-1.

[52] P. Linderholm, U. Seger, and P. Renaud, "Analytical expression for electric field between two facing strip electrodes in microchannel," *Electronics Letters; Stevenage*, vol. 42, no. 3, pp. 1–2, Feb. 2, 2006, ISSN: 00135194. [Online]. Available: https://search-proquest-com.ezproxy.lib.calpoly.edu/docview/1625023765/abstract/FDEF703119314F7APQ/1.

[53] J. Mark, *Polymer Data Handbook*, Second Edition, New to this Edition: Oxford, New York: Oxford University Press, May 22, 2009, 1264 pp., ISBN: 978-0-19-518101-2.

[54] H. Pauly and H. P. Schwan, "Über die Impedanz einer Suspension von kugelförmigen Teilchen mit einer Schale," *Zeitschrift für Naturforschung B*, vol. 14, no. 2, pp. 125–131, 1959, ISSN: 1865-7117. DOI: 10.1515/znb-1959-0213. [Online]. Available: https://www.degruyter.com/view/j/znb.1959.14.issue-2/znb-1959-0213/znb-1959-0213.xml.

[55] M. Min, R. Land, T. Paavle, T. Parve, and P. Annus, "Broadband spectroscopy of a dynamic impedance," *Journal of Physics: Conference Series*, vol. 224, no. 1, p. 012 109, 2010, ISSN: 1742-6596. DOI: 10.1088/1742-6596/224/1/012109. [Online]. Available: http://stacks.iop.org/1742-6596/224/i=1/a=012109.

[56] T. Sun, C. van Berkel, N. G. Green, and H. Morgan, "Digital signal processing methods for impedance microfluidic cytometry," *Microfluidics and Nanofluidics*, vol. 6, no. 2, pp. 179–187, Feb. 1, 2009, ISSN: 1613-4982, 1613-4990. DOI: 10.1007/s10404-008-0315-3. [Online]. Available: https://link.springer.com/article/10.1007/s10404-008-0315-3 (visited on 08/15/2017).

[57] T. Sun, S. Gawad, C. Bernabini, N. G. Green, and H. Morgan, "Broadband single cell impedance spectroscopy using maximum length sequences: Theoretical analysis and practical considerations," *Measurement Science and Technology*, vol. 18, no. 9, p. 2859, 2007, ISSN: 0957-0233. DOI: 10.1088/0957-0233/18/9/015. [Online]. Available: http://stacks.iop.org/0957-0233/18/i=9/a=015.

[58] N. Li, H. Xu, W. Wang, Z. Zhou, G. Qiao, and D. D.-U. Li, "A high-speed bioelectrical impedance spectroscopy system based on the digital auto-balancing bridge method," *Measurement Science and Technology*, vol. 24, no. 6, p. 065 701, 2013, ISSN: 0957-0233. DOI: 10.1088/0957-0233/24/6/065701. [Online]. Available: http://stacks.iop.org/0957-0233/24/i=6/a=065701.

[59] R. F. Probstein, *Physicochemical Hydrodynamics: An Introduction*. John Wiley & Sons, 2005.

[60] N.-T. Nguyen and Z. Wu, "Micromixers—a review," *Journal of Micromechanics and Microengineering*, vol. 15, no. 2, R1, 2005, ISSN: 0960-1317. DOI: 10.1088/0960-1317/15/2/R01. [Online]. Available: http://stacks.iop.org/0960-1317/15/i=2/a=R01.

[61] D. Clague, "Hindered diffusion of spherical macromolecules and fluid flow in dilute fibrous media," PhD thesis, University of California, Davis, 1997.